Winter 1-1-1976

Electromagnetic Penetration into Cylindrical Enclosures

Carl T. Johnk
University of Colorado Boulder

David C. Chang
University of Colorado Boulder

Steve Sandness
University of Colorado Boulder

Larry Rispin
University of Colorado Boulder

Scientific Report No. 17

January 1976

ELECTROMAGNETIC PENETRATION INTO CYLINDRICAL ENCLOSURES

Also a final report on

Contract No. N00173-74-C-0556

entitled

"The Development of Test Methods and Procedures for Electromagnetic Susceptibility Measurements"†

by

Carl T. Johnk, David C. Chang, Steve Sandness and L. Rispin

Prepared for

U.S. Naval Surface Weapons Center
Dahlgren Laboratory
Dahlgren, Virginia 22448

†This project is monitored by Mr. Ronald Prehoda of the Naval Dahlgren Laboratory, Dahlgren, Va. 22448 under contract no. N00173-74-C-0556 from June 12, 1974 to December 30, 1975.

Acknowledgments

The research reported herein was sponsored by the Department of Defense, Department of the Navy. Special thanks must go to Mr. Ron Prehoda of the Naval Surface Weapons Center, Dahlgren Laboratory (NSWC/DL), without whose interest, spirit, and guidance this work would not have been possible; to Mr. John Glass of NSWC/DL, who gave invaluable assistance with that portion of the measurements carried out at the Dahlgren antenna range; and to Dr. Sam Maley of the University of Colorado for numerous suggestions and comments. Finally, a word of appreciation is due Mrs. Marie Kindgren, who patiently typed the manuscript.

TABLE OF CONTENTS

PART I

INTRODUCTION

It is commonly accepted that electromagnetic energy can couple into electronic systems and cause varying degrees of electromagnetic interference (EMI) to the intricate circuitry within. Typically, when such a system is housed inside a metallic enclosure and placed in an electromagnetic environment (EME), penetration of unwanted electromagnetic field into the enclosure may occur whenever there exists any access hatch, cable connector, or seam. Once inside, this externally-generated signal can be picked up by internal cables or component leads and conducted to non-linear circuit elements where the RF portion of the signal is detected. The detected signal (EMI) is then processed along with the main video signal through the ensuing circuitry. From this description it appears that EMI to a typical enclosed electronic system can be separated into the following areas of investigation:

1. shielded enclosures
2. shielded cables
3. cable-to-cable coupling
4. filters
5. component response
6. circuit response
7. sub-system response
8. system response

To guard again EMI effects, several procedures are employed involving the use of "hardened" (less EMI prone) electronic components, improved shielding, R.F. filters, etc., all of which can and should be used together

in reducing EMI. However, only by quantitatively knowing the amount of R.F. leakage into a given system and its impact on the enclosed circuitry can one determine what safeguards are sufficient for adequate protection without entailing expensive and sometimes unnecessary overprotection. Test methods therefore must be developed to evaluate the importance of each of these above mentioned areas in relation to the EMI of the entire system. In this project, we address mainly the problem of shielding effectiveness of long, shielded cylindrical metallic enclosures.

During the funding period of this project, a number of basic coupling mechanisms of a shielded enclosure have been identified. Two physical models representing some of these mechanisms have been designed, fabricated and experimentally evaluated. As part of that evaluation, the response of models was measured at two frequencies, i.e., 200 MHz and 300 MHz, on a roof-top open antenna range at the University of Colorado, and independently verified in the NSWC/DL anechoic chamber. We believe that not only do these two models contain the basic characteristics of a more complicated coupling situation, but they are also of the type which allows a more thorough theoretical investigation. As a consequence, the measured responses of these models can be used as a standard against which any developmental test method may be evaluated. Furthermore, test facilities such as the NSWC/DL anechoic chamber degrade with age, or its characteristics could change if additional supportive equipments are installed. These models can also be used as standards against which changes in chamber performance may be identified.

The first of the two physical models we have investigated is discussed in Part II of this report. It consists of a coaxial cylinder for which the penetration of high frequency electromagnetic radiation can occur whenever there exists any aperture on the periphery of the outer cylinder. Thus, it represents typically the situation where electromagnetic energy can leak into a shielded enclosure (as simulated by the outer cylinder) through holes, access hatches, etc. Once inside, it propagates along a cable system simulated by the inner conductor coaxial with the outer shield, impinging upon a crystal detector connected to one end of the interior coaxial line system. Detailed description of the experimental model, measurement techniques, and the result of the experimental investigation are included. In addition, we have also included in the Appendices a review of theoretical methods pertaining to the evaluation of this model.

The second physical model that we have evaluated consists of a similar coaxial cylinder, except that the peripheral aperture is replaced by a recessed end-cap at one end of the cylinder. Penetration of electromagnetic radiation now occurs mainly at the gap existing between the end-cap and the inner surface of the cylindrical enclosure. Experimental evaluation of this model is contained in Part III of this report.

Finally, in Part IV, we shall summarize and discuss the significance of some important results concerned with the characteristics of these two models. It is worthwhile mentioning that throughout the experimental evaluation of the models we have adopted an optical fiber telemetry system and styrofoam testing mast in order to avoid possible interference. However, as part of the evaluation program on NSWC/DL anechoic chamber performance, we have also included in the report results obtained from replacing the

optical fiber system by a conventional cable system. We believe our experimental investigation has unequivocally demonstrated the necessity of avoiding interference due to scattering objects such as cables, hoods, etc. in the test platform in order to achieve an acceptable quality in the experimental measurements.

PART II

INVESTIGATION OF THE EM PENETRATION THROUGH FINITE APERTURES ON THE SURFACE OF A SHIELDED COAXIAL CYLINDER

Chapter 1

Introduction and Theory

The general topic of electromagnetic shielding is of great practical interest and has received a considerable amount of study, both theoretical and experimental. Among the first such problems considered were those involving the fields inside an unbroken conducting surface. In this case the mechanisms which reduce the intensity of the fields within the shielding structure are the reflection from the surface and attenuation of the incident fields by the material of the shielding walls.

When the conducting structure contains a small aperture, it is probable that the fields penetrating the aperture will far exceed the field penetration through the shield walls. Several recent studies have dealt with this problem as well as the closely related problem of radiation from such a structure when its interior is supplied with electromagnetic energy. Although a rigorous solution of such a problem for an arbitrarily shaped structure is extremely difficult, the special case of a circular cylinder with a circular or elliptical aperture has been more widely investigated; this is the case which is to be studied here.

In this work it is desired to measure the magnitude of current induced in an internal impedance by the electromagnetic energy coupled via a small aperture into the interior of a conducting, cylindrical structure,

when the structure is illuminated by an incident electromagnetic wave. The measured current or voltage appearing at the load then form the basis from which values can be compared.

More specifically, the enclosure system to be evaluated is essentially a cylindrical coaxial device of circular cross-section, with the outer conductor fabricated from aluminum tubing and the inner conductor made of brass tubing. It has brass end caps and two internal brass bulkheads which divide the interior of the device into three cavities. The central cavity contains the coupling aperture in the outer conductor, and contains a load impedance connected in series with the inner coaxial conductor at each end of the central cavity. A sketch of the model is shown in Figure 1; a more detailed discussion on the construction of the model will be found in Section 1.2. For ease of discussion, a schematic diagram of the idealized structure, together with its designated coordinate system, is shown in Figure 2. The inner conductor of outer radius a is concentric with the outer conductor. The structure is located along the z-axis of the cylindrical coordinate system (ρ,ϕ,b) extending from $z=0$ to $z=s$. The ends of the structure are closed. The load impedance Z_o is connected between the inner conductor and the end cap at $z=0$, while another load impedance Z_s is connected between the inner conductor and the bulkhead at $z=s$. The aperture is centered at $\rho'=b$, $\phi'=\pi$, and $z'=\ell$ with the major axis of the aperture perpendicular to the z-axis. The semi-major axis of the aperture is a_e and the semi-minor axis of the aperture is b_e.

The model was illuminated by a suitable electromagnetic wave, and the current in the desired load impedance was measured with appropriate instrumentation. The frequencies of the incident wave, 300 MHz and 200 MHz, were chosen

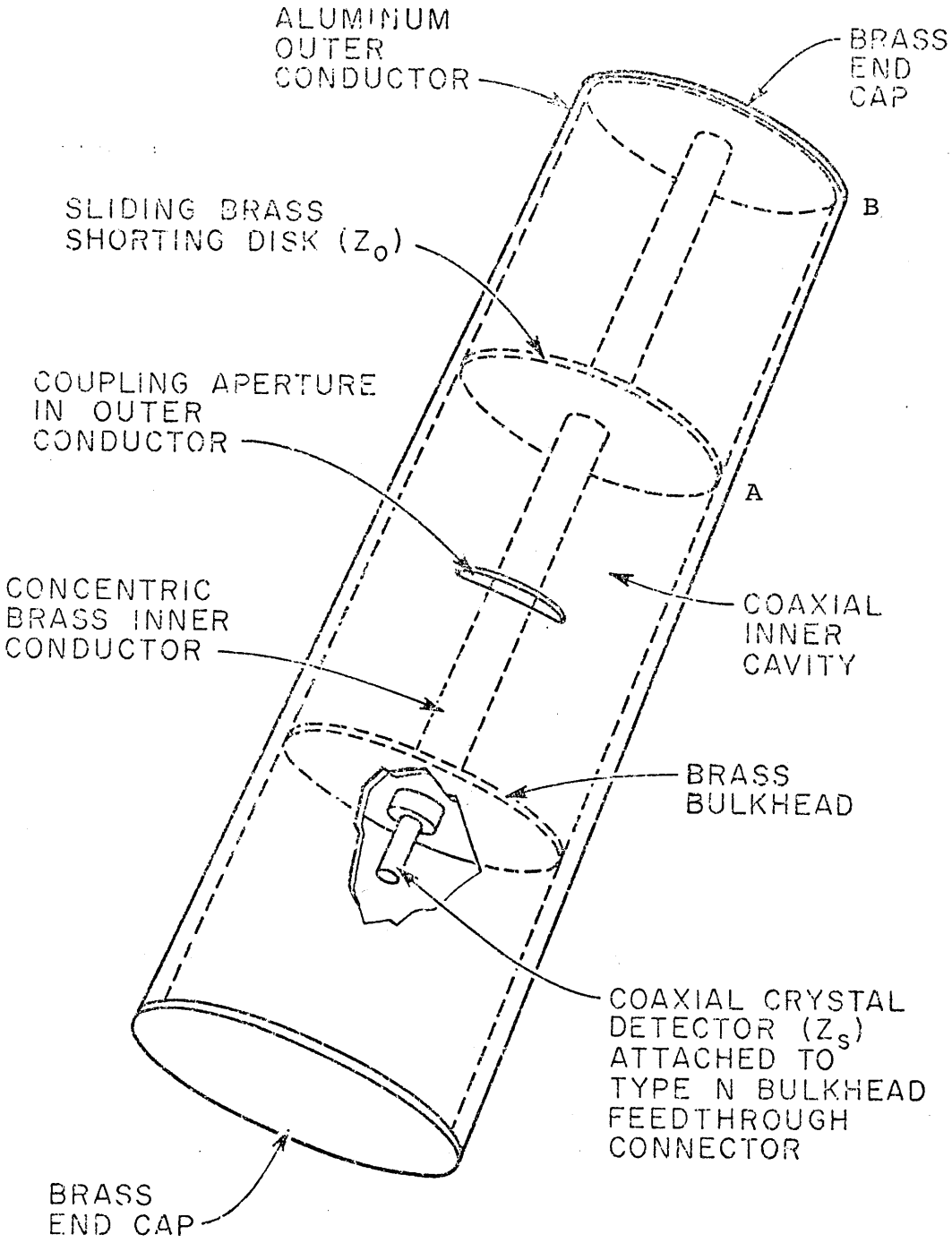

Figure 1. Sketch of the Experimental Model

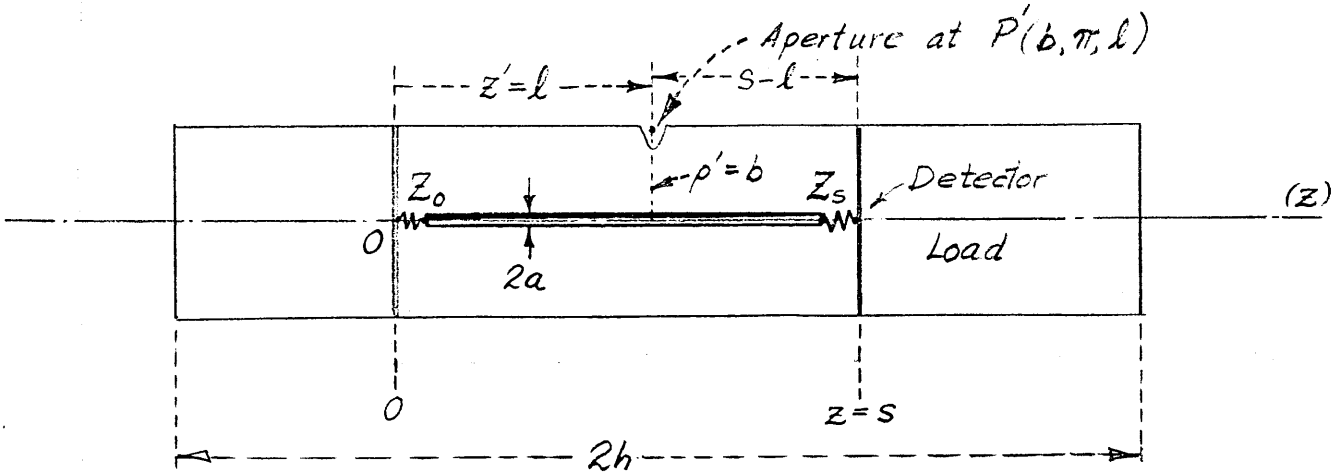

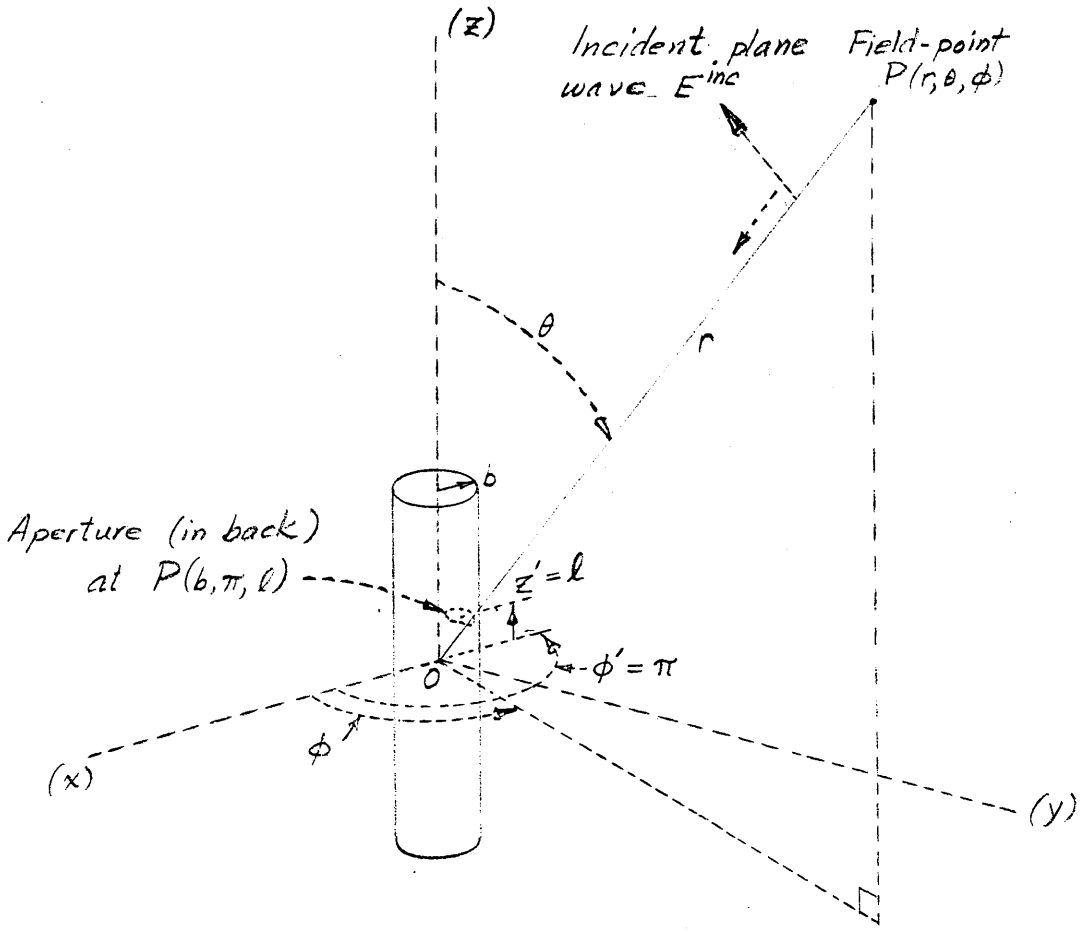

Figure 2. Side View of Idealized Model (above) and Coordinate System (below).

as a compromise between the need for the cylinder diameter to be small when compared to the operating wavelength while still large enough to facilitate the required machining, and the need to keep the overall dimensions small enough for easy handling.

The experimental data were taken on the outdoor antenna range located on the roof of the University of Colorado Engineering Center, and later verified at the NSWC/DL anechoic chamber.

1.1 Theoretical description of the problem

One of the major problems in determining the shielding effectiveness of the enclosure structure just described has been in obtaining an appropriate mathematical model for the energy transmission properties of an electrically small aperture.

The earliest solutions of such aperture problems utilized a Kirchhoff approach in which the diffracted field was expressed in terms of the incident field in the aperture. Stratton [1941] utilized a vector equivalent of this method. In 1944, while studying the coupling of electromagnetic energy from one cavity to another through a small aperture, Bethe [1944] showed that the Kirchhoff approach gave an incorrect solution for the case of the aperture being small compared to the wavelength. He therefore used a quasi-static approximation, considering the aperture to be immersed in uniform electric and magnetic fields, and expressed the penetration fields in terms of electric and magnetic dipoles imagined to be located at the aperture position. The magnitudes of these dipoles were assumed proportional to the normal electric and tangential magnetic fields that would exist at the aperture location if the aperture were absent. Bouwkamp [1954] pointed out that Bethe's analysis, while adequate for field

points at a distance large compared to the aperture diameter (at least greater than a wavelength), gave incorrect results for points nearer the aperture because of a missing term. More recently, Collin [1960], in a more direct manner, has derived explicit expressions for the equivalent electric and magnetic dipoles of an elliptical aperture using the Schelkunoff equivalence principle. A summary of the result he derived is included in Appendix A. In addition, Van Bladel showed, in 1970, that the equivalent dipoles for any electrically small aperture can be obtained from the solution of two linearly-independent integral equations. Using a variational technique, Fikhmanas and Fridberg [1973] also showed that the dipole moments are more critically dependent upon the aspect ratio, rather than the precise shape of the aperture.

If we now replace the aperture by its equivalent electric and magnetic dipoles (induced by the external field), we can analyze the aperture coupling problem in the usual manner according to the conventional theory of antennas and transmission lines. For instance, in the study of aperture radiation, we can first use transmission-line circuit analysis to obtain the normal electric and tangential magnetic field at the aperture due to an internal voltage generator placed at one end of the coaxial cylinder. These field expressions can then be used to calculate the equivalence dipole moments at the aperture. We can then think of the external surface of the enclosure from a tubular antenna point of view, and analyze the radiation problem from conventional linear cylindrical antenna theory, except that the excitation of the antenna is provided by dipole sources instead of a voltage generator. To obtain the fields coupled through the aperture, the use of the Lorentz reciprocity theorem would yield an expression for the load current produced

by an incident electromagnetic plane-wave in a load impedance located within a conducting enclosure containing a small aperture. A summary of the expression as derived by Harrison and King [1972] is included in Appendix B. On the other hand, Taylor and Harrison [1973] used conventional receiving antenna theory to formulate a solution for the identical cylinder-with-aperture problem, using a quasistatic approximation for a normally-incident field. Although the approaches taken in these two papers were completely different, the numerical results are nearly identical for the same normally-incident plane-wave case. In the same year, Chang, Harrison, and Taylor [1973] showed that, given a dissipationless line, the load current expressions originally derived by Taylor and Harrison by use of a series of approximations were in fact exact solutions. A more detailed discussion of these results is included in Appendix B. However, we should point out that Taylor and Harrison did not treat the case of an oblique-incidence plane wave. To generalize their approach, we have also utilized the work of Shen [1970] and discussed in Appendix B what modifications are required for its application to near-grazing incidence.

1.2 Detailed Description of the Experimental Model

A diagram and pictures of the experimental model are shown in Figures 3 and 4 . The outer conductor of the interior tunable coaxial structure was machined from four-inch O.D. tubing made of 6061 aluminum alloy, with a 0.375 inch wall thickness. To facilitate changing the coupling aperture size and shape as well as its axial location, and for ease of assembly, the outer conductor is subdivided into several shorter lengths which screw together. In the first model constructed, each

different coupling aperture was machined into a separate, interchangeable section of aluminum tubing. (In an alternative refinement, one such section of tubing was ported to accept several different mounting plates, each containing a different aperture configuration.) The four-inch O.D. tubing was selected because it provides sufficient wall thickness to allow the machining of screw threads, and is sufficiently rugged to allow considerable handling. In the vicinity of the aperture, the outer conductor was reduced in thickness to more nearly agree with the mathematical model for which zero wall thickness was assumed. This was accomplished by machining a flat surface on the outer conductor, centered on the aperture to make the wall thickness at the aperture semi-minor axis approximately 0.10 inch.

The inner conductor of the coaxial structure is made of 0.625-inch O.D. brass tubing. An adapter fitted at one end allows the connection to a Type N coaxial feed-through connector, mounted on a brass bulkhead. A polyethylene disk located next to the bulkhead supports the end of the inner conductor. This assembly forms one end of the interior coaxial cavity as shown in Figure 5. A coaxial crystal detector mount attached to the type N connector serves as the load impedance Z_s. At the other end of the coaxial structure, a sliding brass shorting plate (plate "A" in Figure 6) serves as the zero load impedance Z_0. Brass end caps are mounted on the ends of the 4" tube to complete the model, thereby isolating the exterior electromagnetic behavior of the cylinder from its internal behavior, except for the coupling provided by the aperture in the outer wall.

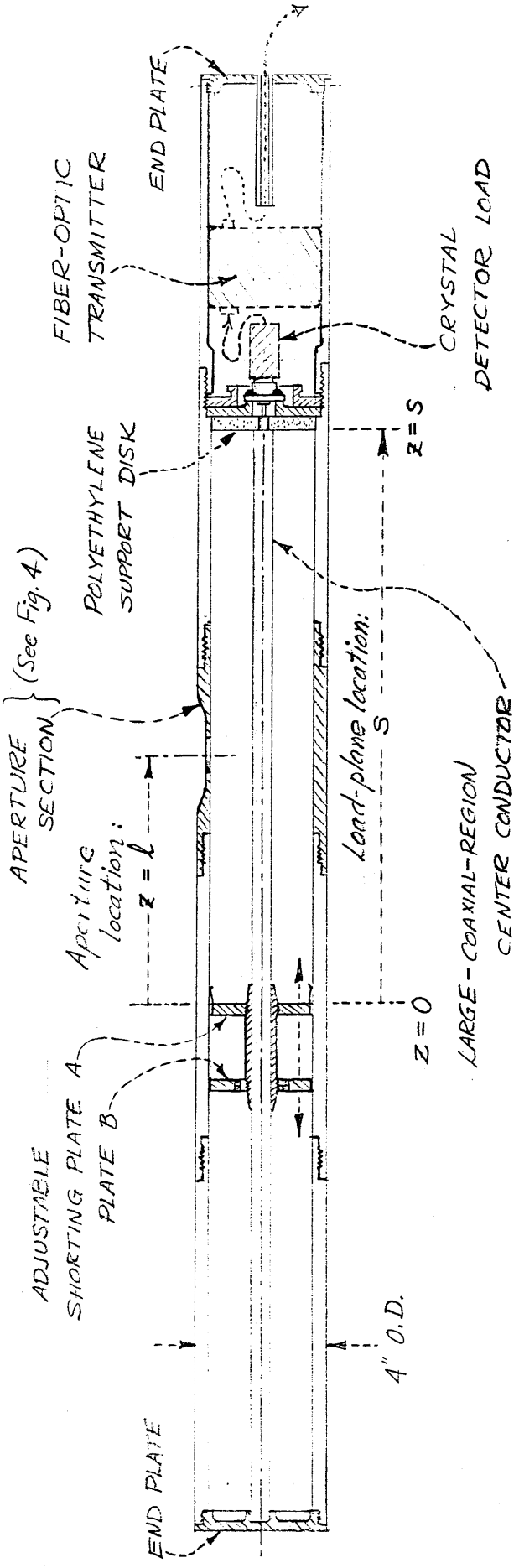

Figure 3. Sectional View of First Experimental Model

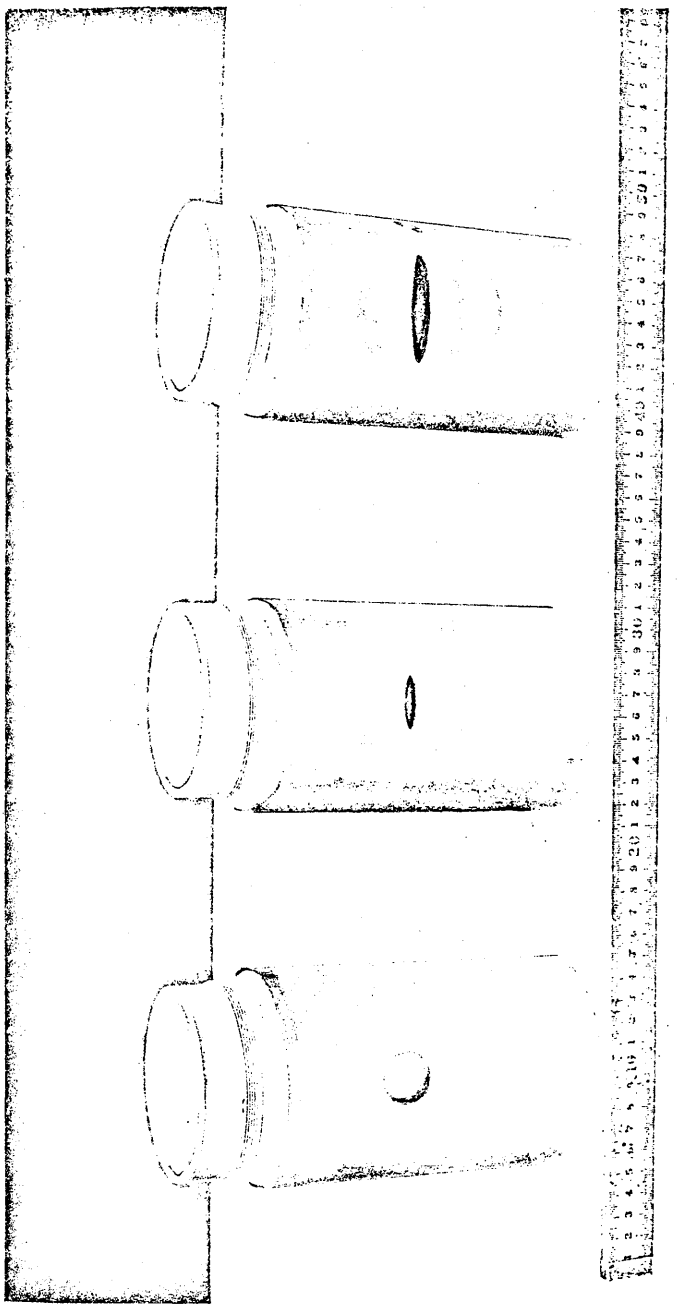

Figure 4. Apertures Used with the Experimental Model

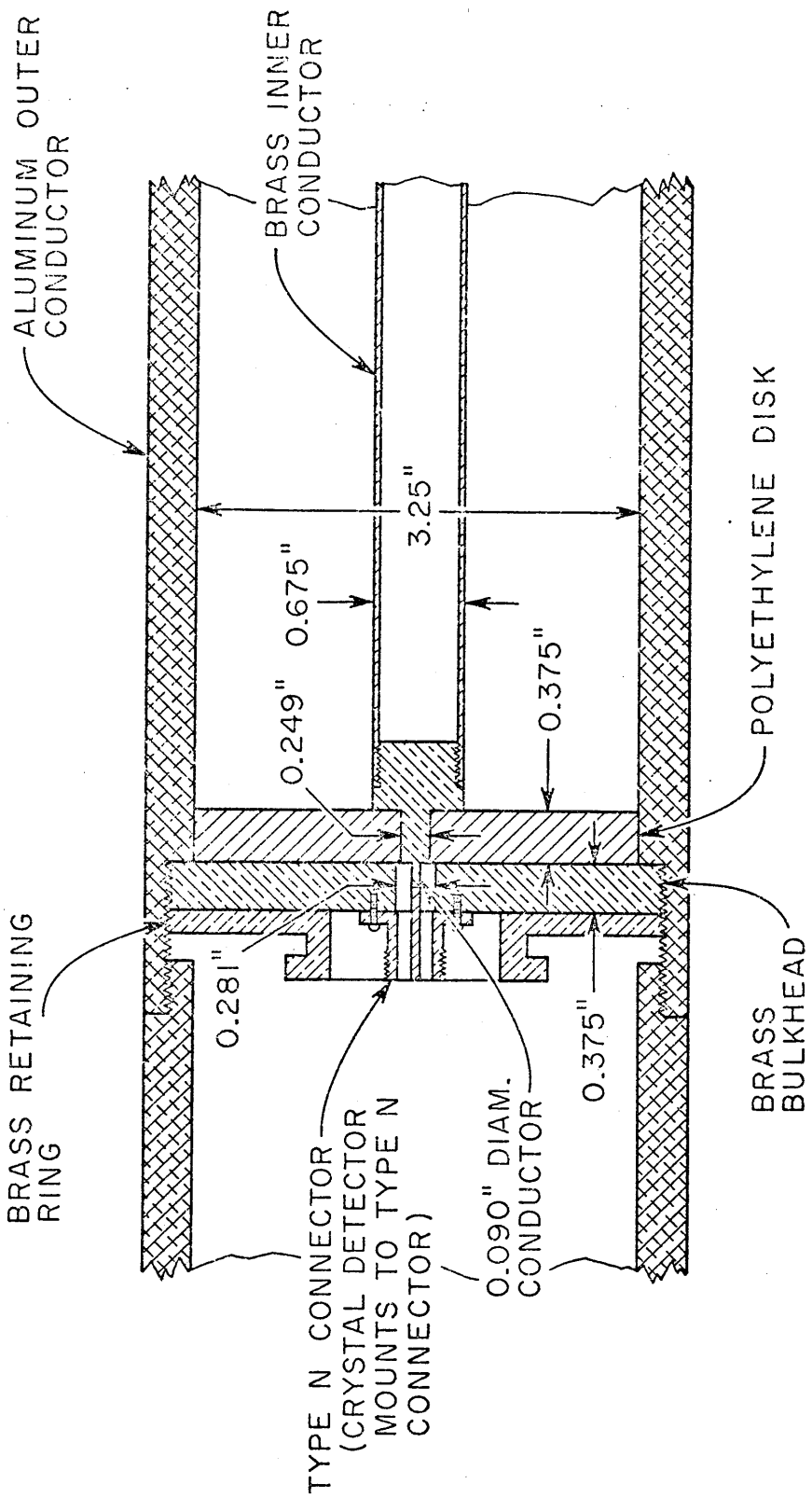

Figure 5. Load Impedance Z_s Detail

1.3 Measurement of the Load Impedances

The load impedance at the position $z = 0$ in Figure 3 is the shorting assembly, reasonably assumed to have zero ohms R-F impedance. Because of the discontinuities present at the crystal detector end of the large inner coaxial system, it was felt necessary to measure directly the R-F impedance presented by the crystal detector mount at the output plane of the coaxial system, (i.e. at the interface formed by the polyethylene disk and the air dielectric of the coaxial line region). To accomplish this, a special slotted center conductor was built, containing a small electric probe and crystal detector, moveable in the slot as shown in Figure 6. This slotted conductor replaces the normal center conductor of Figure 6. During this measurement, the sliding shorting plate assembly was removed, and a small conducting loop attached to a different brass end at the far end of the coaxial line was used to excite the interior of the coaxial system. No coupling aperture was then used in the outer conductor.

With the slotted center conductor and electric-field probe in place as described, an SWR meter (1000 Hz amplifier) was connected to the detected output of the probe as shown in Figure 6. The normal 50 ohm termination of the coaxial line, provided by the Hewlett-Packard Model 423B detector mount, was replaced by a 50 ohm dummy load to avoid the risk of crystal burnout in the detector mount. Then with energy coupled into the coaxial system through the input loop, the resulting SWR measurement by means of the sliding electric-field probe led to a load impedance, looking into the air-polyethylene interface at the plastic support slab just ahead of the crystal-detector mount, of $Z_s \cong 55$ ohms.

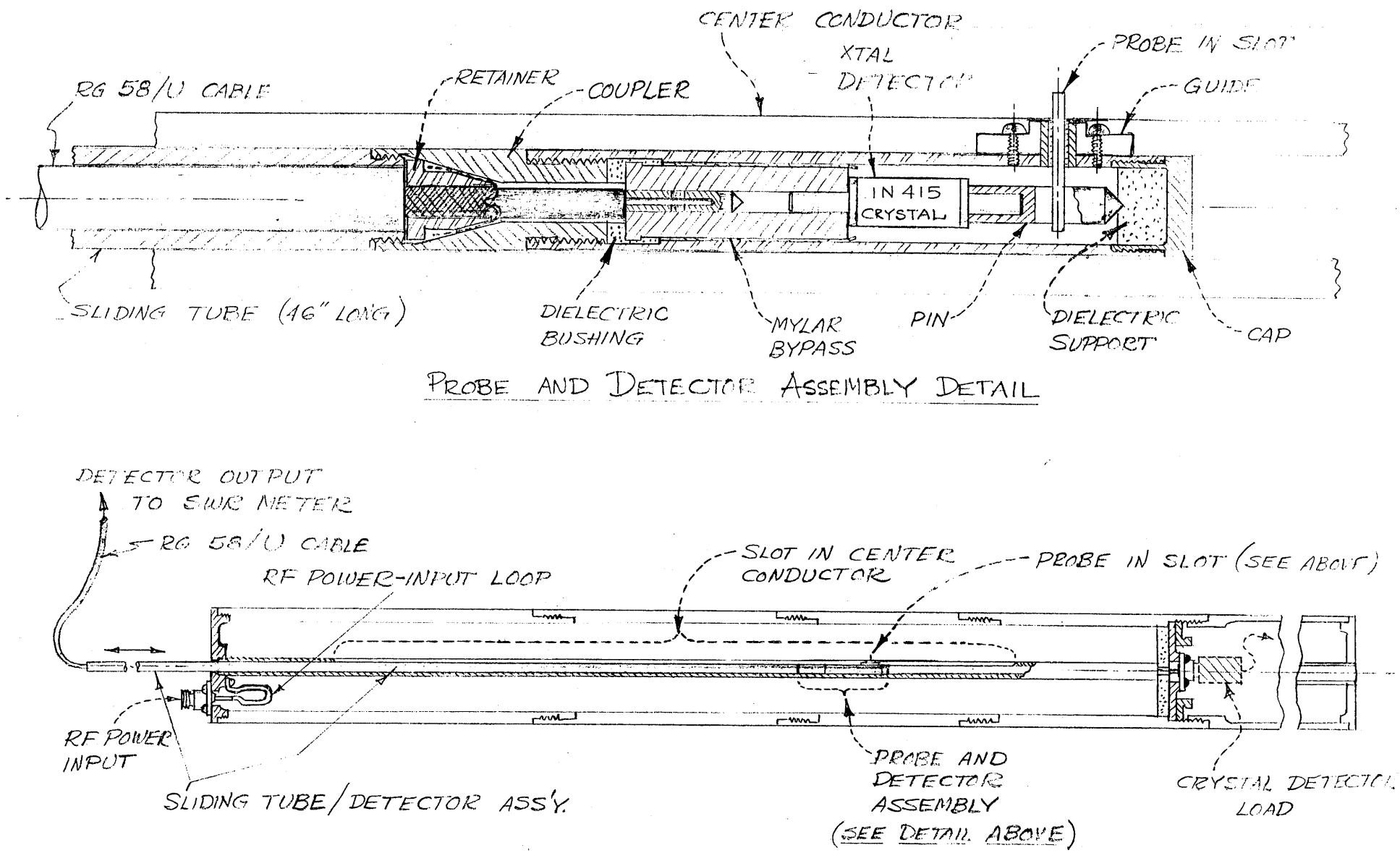

Figure 6. Model Supplied with Slotted Center Conductor, Probe and Detector Assembly, and RF Power Input Loop for Load Impedance Measurement (below). Above is Detail of Probe and Detector Assembly.

1.4 Instrumentation

1.4.1 Preface and General Description of Test Set-up The experimental data were taken on the University of Colorado outdoor antenna test range. The experimental model was mounted on a polyfoam support mast, and was illuminated by electromagnetic energy supplied by a high power oscillator and radiated from a transmitting dipole. (A more complete description of the test range is found in Section 1.5)

The output signal from the internally mounted crystal detector (load impedance Z_s) was carried over a few inches of coaxial cable to the transmitting unit of a fiber-optic data link, mounted in one end of the experimental model. A fiber-optic cable was connected from the latter to an externally located receiving unit a few meters away, which in turn was connected to an SWR meter (a tuned 1000 Hz amplifier), used to measure the magnitude of the crystal detector voltage output. From this value, the magnitude of the load current was calculated. The instrumentation used in the model calibration and in the pattern measurements is described in the following.

1.4.2 Crystal Detector Calibration A diagram of the crystal calibration equipment set-up is shown in Figure 7. A Hewlett-Packard Model 415B SWR meter was chosen to measure the crystal detector output because of its high-gain tuned (1000 Hz) amplifier and its square-law detector calibration. The narrow (30 Hz) bandpass of the amplifier was desirable for reducing the effects of noise from the detector and the fiber-optic data link. The incident wave was sinusoidal amplitude modulated. Thus, the output indicated by the SWR meter was dependent on four parameters: the modulation frequency, the modulation waveform, the percentage modulation, and the gain of the SWR meter amplifier; values of

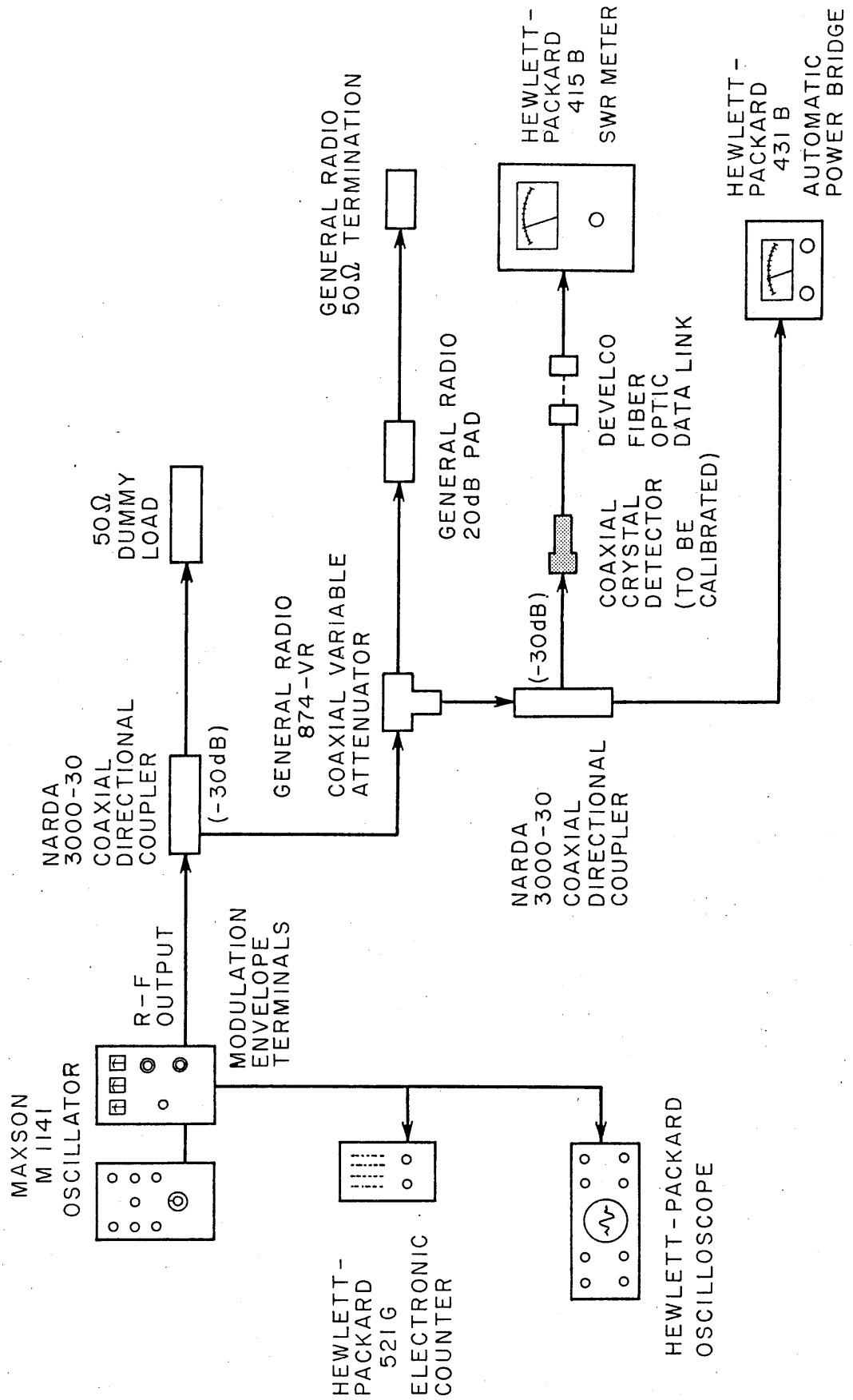

Figure 7. Instrumentation for Crystal Detector Calibration

these were fixed throughout the measurements. The modulation-signal frequency of 986 Hz yielded the maximum indication on the particular tuned SWR meter used, while the modulation was set at 40 percent, and the gain control of the SWR meter was set at its maximum. The monitoring equipment used included an electronic counter to measure the frequency, and a d-c oscilloscope to monitor the detected modulation waveform and the percentage modulation.

The calibration of the crystal detector was accomplished by recording the SWR meter indication versus the power measured by a Hewlett-Packard Model 431B automatic microwave power bridge, for several known input power levels, with the R-F test signal supplied by the same high-power oscillator used for the test measurements. A calibrated Narda Model 3000-30 coaxial directional coupler was used to supply known fractions of the R-F test signal to the power bridge bolometer mount and to the crystal detector mount being calibrated (with the crystal detector connected to the sampling port (30 dB down), and the bolometer mount connected to the primary output port). This desirable arrangement was utilized because the maximum power to be measured in the experimental tests by the crystal detector was to be far less than the least power measurable by the power bridge. Thus the exact amount of coupling attenuation provided by the directional coupler relative to its output level was easily measured using a second power bridge. The crystal detector calibration curve obtained for the particular HP 423A detector mount used is shown in Figure 8. That a precise square-law response was obtained from this crystal is evident from the exact correspondence of the 10:1 power change on the abscissa of this curve to a 10 dB change in the SWR meter indication on the ordinate.

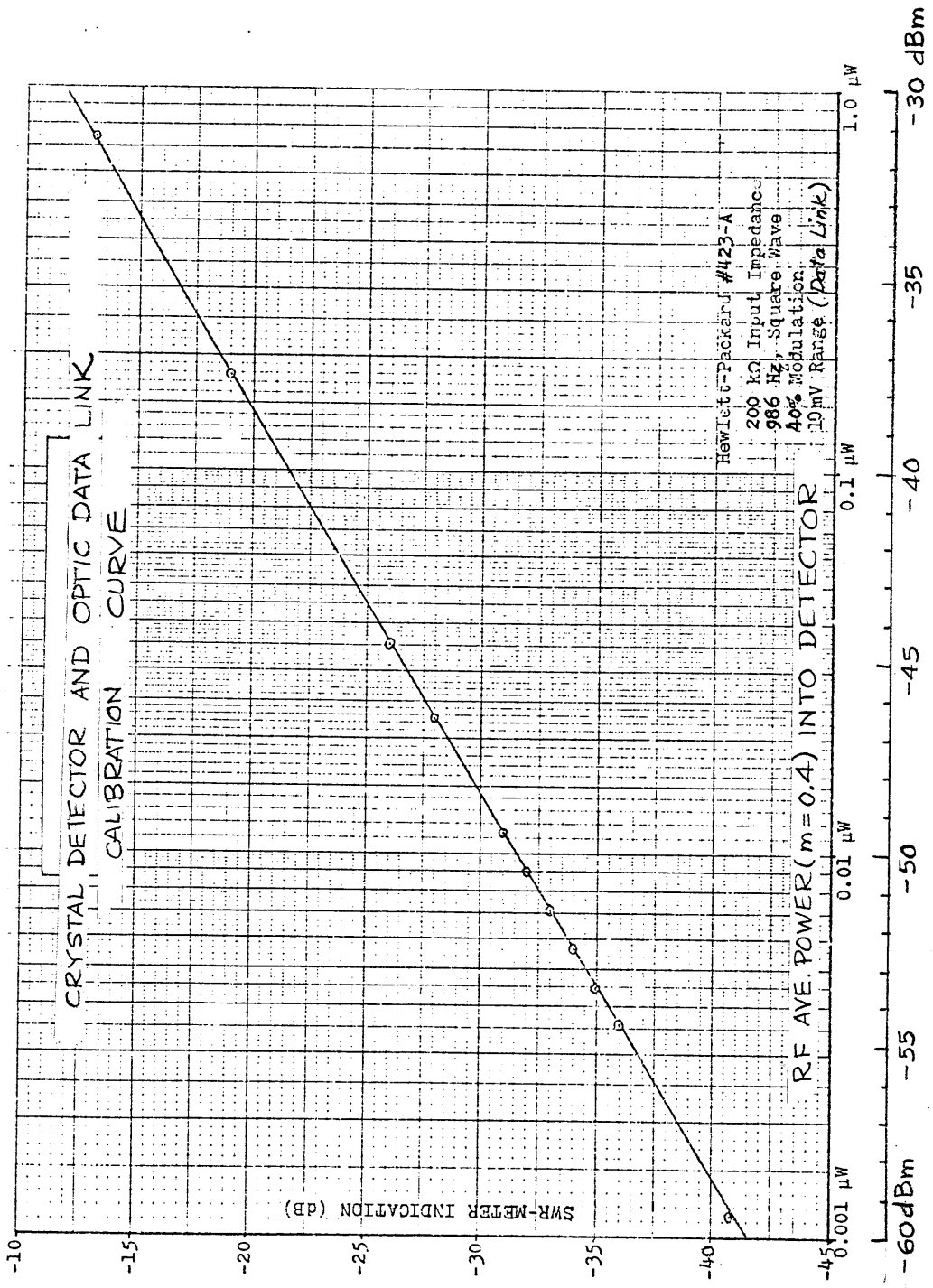

Figure 8. Calibration Curve for the HP423A Coaxial Detector Mount and Optic Data Link Employed.

1.4.3 Data Transmission Link Transmitting the audio-frequency signal from the internal crystal detector mount in the model to the externally located SWR meter presented several difficult problems. First, upon extracting the audio signal from the experimental model, one ran the risk of coupling unwanted R-F energy into the model, thereby possibly affecting the crystal detector. Second, a metallic cable attached to the end (or the side) of the model could provide an additional, unwanted contribution to the external surface current on the model, yielding a possible distortion of the desired results. Finally, the proximity of the metallic cable could alter the incident wave by producing nearby reflections, to cause a non-uniform electric field to arrive at the model. An optical fiber data transmission set was then utilized to transmit the signal from the crystal detector to the SWR meter. It was observed that the use of the thin, non-metallic fiber-optic cable essentially eliminated these problems.

A Develco Model 6112 optical fiber transmitter unit was modified to fit inside the experimental model. The only connection to the experimental model was the glass fiber cable, entering the model through a hole centered in the brass end cap, to which a four-inch long piece of brass tubing was internally attached. The inside diameter of the tubing was approximately 0.187 inch; thus it formed a small circular waveguide. Since the operating frequency of 300 MHz was far below the cutoff frequency of this circular waveguide, the propagation of any R-F energy from the exterior of the model to its interior via the data link was prevented.

1.4.4 Transmitter A Maxson Model M1141UHF power oscillator was used to generate the incident wave. The transmitter instrumentation is shown in Figure 9. The modulation signal was generated internally. An oscilloscope and an electronic counter were connected to the modulation terminals of the oscillator, to monitor the percentage modulation and the modulation frequency. In addition, the demodulated waveform on the oscilloscope provided a means of ensuring that the oscillator was tuned properly and generating a clean output signal free of spurious emissions.

The R-F power delivered to the transmitting antenna was measured with the Hewlett-Packard Model 431B power bridge and a Narda coaxial directional coupler. The operating frequency of the UHF oscillator was measured by heterodyning the output of the high-power oscillator and a reference signal generated by a General Radio Model 1209-C Unit Oscillator in a GR Model 874-VR coaxial mixer. The resulting output signal was detected by a GR Model 1216-A IF amplifier. By adding (or subtracting) the 30 MHz center frequency of the IF amplifier to the frequency to which the unit amplifier was tuned, the carrier frequency of the high-power oscillator was easily determined.

1.5 Assumptions Made in Using the Experimental Model

In order to construct a useful physical model, some departures from the assumptions made for the idealized model used in the theoretical derivations were found to be necessary. The assumptions made for the physical model were:

1. The only energy coupled from the exterior incident fields to the inside of the experimental model was that penetrating the aperture, a reasonable assumption because of the ample wall thickness.

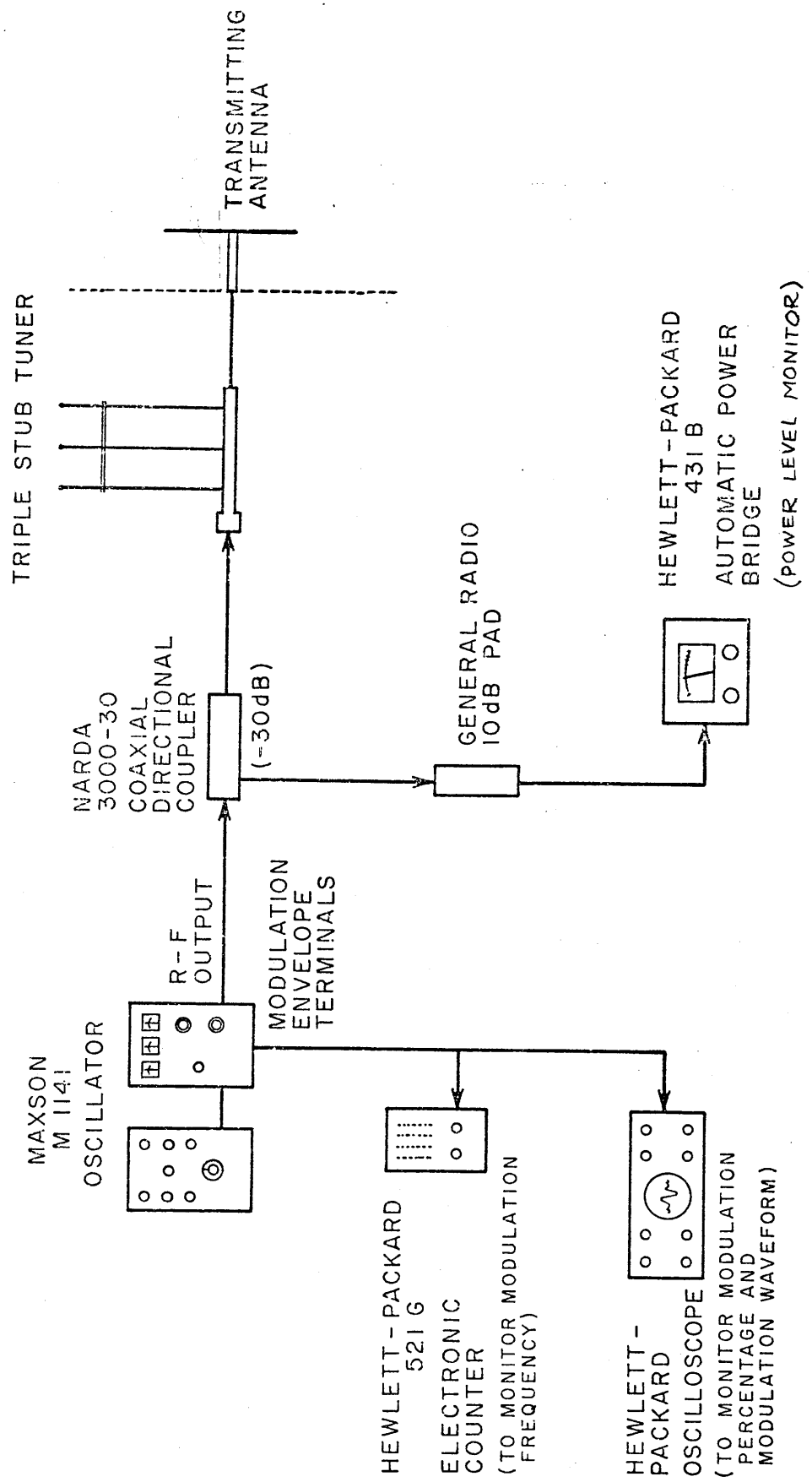

Figure 9. Transmitter Instrumentation

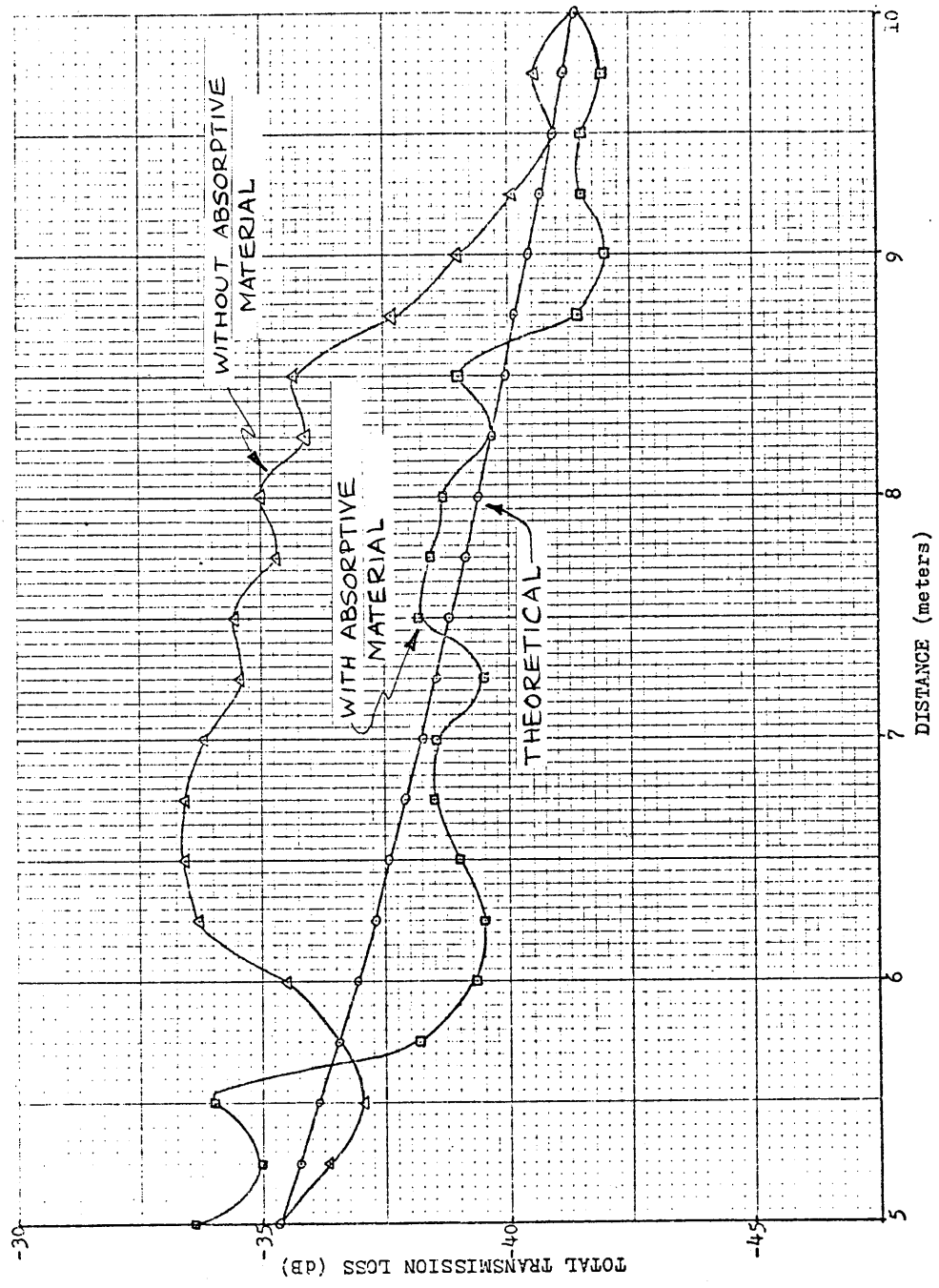

Figure 10. Total Transmission Loss versus Radial Distance

$$\frac{P_{av,r}}{P_{av,t}} = \frac{A_{er} A_{et}}{\lambda^2 r^2} \quad .$$

In the above, $P_{av,r}$ and $P_{av,t}$ are the received and transmitted average powers, respectively, A_{er} and A_{et} are the effective areas of the receiving and transmitting antennas, respectively, λ is the operating wavelength, and r is the radial distance from the transmitting to the receiving antenna in meters.

The effective area of an antenna is expressed as

$$A_e = g \frac{\lambda^2}{4\pi}$$

in which g is the gain of the antenna. The gain of the receiving half-dipole was taken to be 1.64. The transmitting antenna included a ground screen, yielding a theoretical gain of 3.28. Thus, with $A_{er} = 1.64\ \lambda^2/4\pi$ and $A_{et} = 3.28\lambda^2/4\pi$, one obtains the path loss, assuming far-zone operation:

$$\frac{P_{av,r}}{P_{av,t}} = \frac{5.38\lambda^2}{(4\pi r)^2} \quad .$$

Expressed in dB,

$$\text{Path loss} = 10 \text{ Log}_{10} \left\{ \frac{\sqrt{5.38}\,\lambda}{4\pi r} \right\}^2 = 20 \text{ Log}_{10} \frac{\sqrt{5.38}\,\lambda}{4\pi r} \quad .$$

To obtain the total transmission loss incurred between the measured transmitter power and the receiving-dipole power meter reading, one must add to the calculated path loss: (a) the losses of the connecting coaxial cables, (b) the insertion loss of the directional coupler used to measure the transmitted power, and (c) the scattering loss introduced by the transfer of power from the receiving antenna to the power meter. In the system used, the

cable losses provided by 88 feet of 50 ohm line, were measured to be 3.4 dB, the insertion loss was 0.3 dB, and the scattering loss into the matched load was 3 dB. The operating wavelength was one meter. Thus,

$$\text{Total transmission loss} = -6.7 + 20 \log_{10} \frac{\sqrt{5.38}}{4\pi r} \text{ [dB]}$$

The tests showed, from Figure 10, that the reflection from the surface of the range was significant. The addition of the absorptive material greatly reduced the interference effects of the reflected wave. The direct wave and the wave reflected from the test range surface were most nearly in phase at approximately 7.75 meters, as evidenced by the greatest difference between measured and theoretical power occurring at that distance. In order to reduce or avoid problems caused by out-of-phase waves arriving at the test point, $r = 7.75$ meters was chosen as the distance to be used on the test range with the experimental model. It is to be noted that experimental discrepancies such as the wave reflected from the test range surface added approximately 1.0 dB to the total power at the test point when the radial distance was 7.75 meters. In order to account for this additional incident wave, 1.0 dB was added to the input average-power reading $P_{av,i}$ obtained from the transmitter instrumentation (a correction factor of 1.258).

It should be observed that the foregoing procedure was adopted as a means for evaluating the particular idiosyncrasies of the outdoor test range on which the model measurements were made. Once the evaluation of the success of reducing the reflections from the floor surface had been made, no further application of the foregoing procedure was found necessary.

1.7 Computation of Field Strength at Test Location

To permit a comparison of the theoretical analysis of the model behavior with experimental result obtained, the value of the electric field

intensity E^{inc} established by the transmitting antenna at the location of the model under test needs to be known. The value of E^{inc} there can be obtained two ways: (a) by a direct measurement using a field-strength meter, or (b) from a calculation based on the measured average R-F power injected into the transmitting antenna. The determination of the incident field E^{inc} by method (b) is discussed in what follows.

The knowledge of the input power to the transmitting antenna and its gain are sufficient to enable calculating the electric field intensity E^{inc} at a distance r from the transmitting antenna, assuming r to be in the far zone. This relationship may be determined as follows. Assume the transmitting antenna for the moment to be an idealized "isotropic" antenna, i.e., radiating power into the far zone with equal densities in all directions. Then with $P_{av,t}$ denoting the input average power driving it, the time-average power density $\mathcal{P}_{av}^{inc}$ (a radial Poynting vector) at the radial distance r would amount to the power flux $P_{av,t}$ distributed uniformly over a sphere of radius r, divided by the area of the sphere, or $\mathcal{P}_{av}^{inc} = P_{av,t}/4\pi r^2$ watts per square meter. In the system used, the antenna was of course not isotropic, but rather a reflector-backed dipole having the maximum directive gain of $g = 3.28$; thus, the power density at the main-beam maximum and at the radial distance r is by definition g times the result above, or

$$\mathcal{P}_{av,r} = g \frac{P_{av,t}}{4\pi r^2} \quad [W/m^2]$$

With the time-average Poynting power-density vector at the farzone distance r given by $\mathcal{P}_{av}^{inc} = \frac{1}{2}E^{inc}H^{inc}$ in terms of the peak values E^{inc} and H^{inc} of the sinusoidal fields there (or by $P_{av,t} = E_{rms}^{inc} H_{rms}^{inc}$ in terms of rms values), one may write, with $H^{inc} = E^{inc}/\eta_o$ in the far zone (assuming an essentially uniform plane wave in the vicinity of the test model):

$$\mathcal{P}_{av}^{inc} = \left(\frac{E^{inc}}{2\eta_0}\right)^2 = g\,\frac{P_{av,t}}{4\pi r^2}$$

in which η_0 denotes the free-space intrinsic wave impedance 120π ohms. Solving for E^{inc} yields, for the peak electric field intensity at the distance r:

$$E^{inc} = \left[\frac{2\eta_0 g}{4\pi r^2}\,P_{av,t}\right]^{\frac{1}{2}} = \frac{(196.8\,P_{av,t})^{\frac{1}{2}}}{r} \quad [V/m]$$

If the rms (effective) value of the electric field is preferred, one obtains:

$$E_{rms}^{inc} = \frac{(98.4\,P_{av,t})^{\frac{1}{2}}}{r} \quad [V/m]$$

for the present case to which the transmitting antenna gain $g = 3.28$ applies. In the foregoing tests, unless otherwise specified, it is to be noted that the transmitted power from the Maxson transmitter was set at a constant value of 24.1 watts.

1.8 Influence of the Modulation Index m on the Measurements

A brief discussion may be in order concerning the effects of the amplitude-modulation of the r-f carrier upon the measured results obtained from the model tests. Observe first that the expression for the r-f peak sinusoidal electric-field magnitude, arriving at the model site from the transmitting antenna, and given earlier by

$$E^{inc} = \left[\frac{2\eta_o g}{4\pi r^2} P_{av,t}\right]^{\frac{1}{2}}$$

is certainly applicable to unmodulated r-f (CW) conditions. In the actual tests, of course, the r-f signal is sinusoidally amplitude-modulated (at 1000 Hz) with some modulation index m. Thus, whereas the value of the antenna r-f input average power $P_{av,t}$ into the transmitting antenna (matched to $R_o = 50\Omega$ input impedance) is given by

$$P_{av,t} = \frac{V_o^2}{2R_o}$$

if V_o denotes the feed-line r-f voltage amplitude, one observes under sinusoidal amplitude modulation conditions that the input average power increases to

$$P^{mod}_{av,t} = \frac{V_o^2}{2R_o}(1 + \tfrac{1}{2}m^2) = P_{av,t}(1 + \tfrac{1}{2}m^2)$$

if m is the modulation index and V_o is the same carrier voltage amplitude as before. Thus, the r-f signal power increases by $(1 + m^2/2)$ when the carrier is amplitude-modulated.

The latter value of average power $P^{mod}_{av,t}$ is, of course, the average power level actually monitored, under amplitude-modulation conditions, by

the HP431B thermistor power meter used both in the instrumentation system of Figure 9, and in the detector-load system calibration setup shown in Figure 7. For example, with a transmitter input average power of $P_{av,t}^{mod} = 24.1$ watts and $m = 0.65$, the amount of this power attributable to only the carrier is $P_{av,i}^{mod}$ divided by $(1 + m^2/2) = 1 + (0.65)^2/2 = 1.21$, yielding $P_{av,t} = 19.92$ watts. However it is to be noted that such corrections back to CW conditions do not, in fact, need to be made in connection with r-f average power levels (or for that matter, r-f voltage or current amplitude levels) measured at the antenna input terminals and at the detector-load input terminals, as long as comparisons are being made between quantities to which the same modulation index m is applicable. Thus, in looking for a model "response" as defined in Section 2.3 by the ratio $P_{av,s}/\mathcal{P}_{av}^{inc}$, both quantities involve the modulation index m, and upon converting each back to corresponding CW levels, a cancellation of the dividing factors $(1 + m^2/2)$ occurs, thus obviating any need for such conversions. This feature is of course simply a consequence of the system being linear.

Similar comments apply to model-response considerations making use of the response ratios

$$|I_s|/|E^{inc}| \quad \text{or} \quad |V_s|/|E^{inc}|$$

suggested at the beginning of Section 2.3. In such cases, with the Poynting average power density incident on the model being related to E^{inc} by $\mathcal{P}_{av}^{inc} = |E^{inc}|^2/2\eta_o$, it is seen again that the factor $(1 + m^2/2)$ is applicable to $\mathcal{P}_{av}^{inc}$ upon comparing its CW power density with that obtained when the signal is amplitude modulated. Therefore a comparison of the

incident electric field E^{inc} to an "equivalent value" E^{inc}_{mod} when that signal is modulated, shows an increase of the latter over E^{inc} by the factor $(1 + m^2/2)^{\frac{1}{2}}$. Furthermore, the average power reaching the detector load input impedance $Z_s = R_s + jX_s$ is written as

$$P_{av,s} = \tfrac{1}{2}|V_s||I_s| \cos\theta = \tfrac{1}{2}R_s|I_s|^2 = \tfrac{1}{2}G_s|V_s|^2$$

if G_s is the real part of the detector load r-f input admittance $Y_s = G_s + jB_s$. Thus, in view of the squared relationships, both the detector voltage and current amplitudes are subject to the same increase factor $(1 + m^2/2)^{\frac{1}{2}}$. Thus, the response ratios defined above on the basis of the detector load quantities $|I_s|$ and $|V_s|$ similarly require no conversions to corresponding CW levels.

1.9 Influence of the Detector Load Transition Region on the Measurements. An inspection of the interior coaxial system of Figure 3 (first model) and Figure 40 (second model) shows the presence of a 0.375" thick polyethylene disk transition region connecting the large coaxial-line interior of the model to the nominally 50-ohm crystal detector load, fitted to a Type N connector at the brass bulkhead just beyond the polyethylene disk. The question might arise as to whether the fact that the outer 3.25" diameter of the large coaxial region, in undergoing a discontinuous change to a much smaller (0.281") diameter at this location to generate higher-order coaxial-line modes there, might adversely contribute to an excessively high reactive component to the load impedance seen by the large coaxial line at the air-polyethylene interface that constitutes its load plane.

2.1.1 Effect on Model Patterns of Changes in Distance to the Test Position. It was found in Section (I)1.6 that even with the addition of absorptive material, the test-range surface produced a small residual reflected wave affecting the magnitude of the incident wave slightly at the test position on the outdoor antenna range. Since there was also a possible phase difference between the direct and reflected waves at the test position, it was desired to determine the effect of the reflected wave on the pattern of the experimental model. Hence, the radial distance from the transmitting antenna to the test position was changed incrementally, to alter slightly the phase relationship between the direct and reflected waves. The results shown in Figure 11 show no significant change in the pattern shapes for three radial distances differing by 0.5m increments. These results also reveal that the model was sufficiently far away from the transmitting antenna to place it in the far-zone of the latter, thereby assuring an incident wave that could be considered essentially uniform plane. These tests thus confirmed the suitability of using the test position 7.75 meters from the transmitting antenna.

2.1.2 Effect of Azimuthal Incidence Angle ϕ on Field Patterns. It was observed, in preliminary tests at an operating frequency of 300 MHz, that the pattern produced by rotating the experimental model azimuthally was not axially symmetric (independent of ϕ) as had been expected. In order to investigate further this phenomenon, involving a pronounced difference in magnitude between the "front" and "back" lobes (relative to aperture location), patterns were taken for an operating frequency of 300 MHz, and then at 200 MHz. Seven patterns were included in each series,

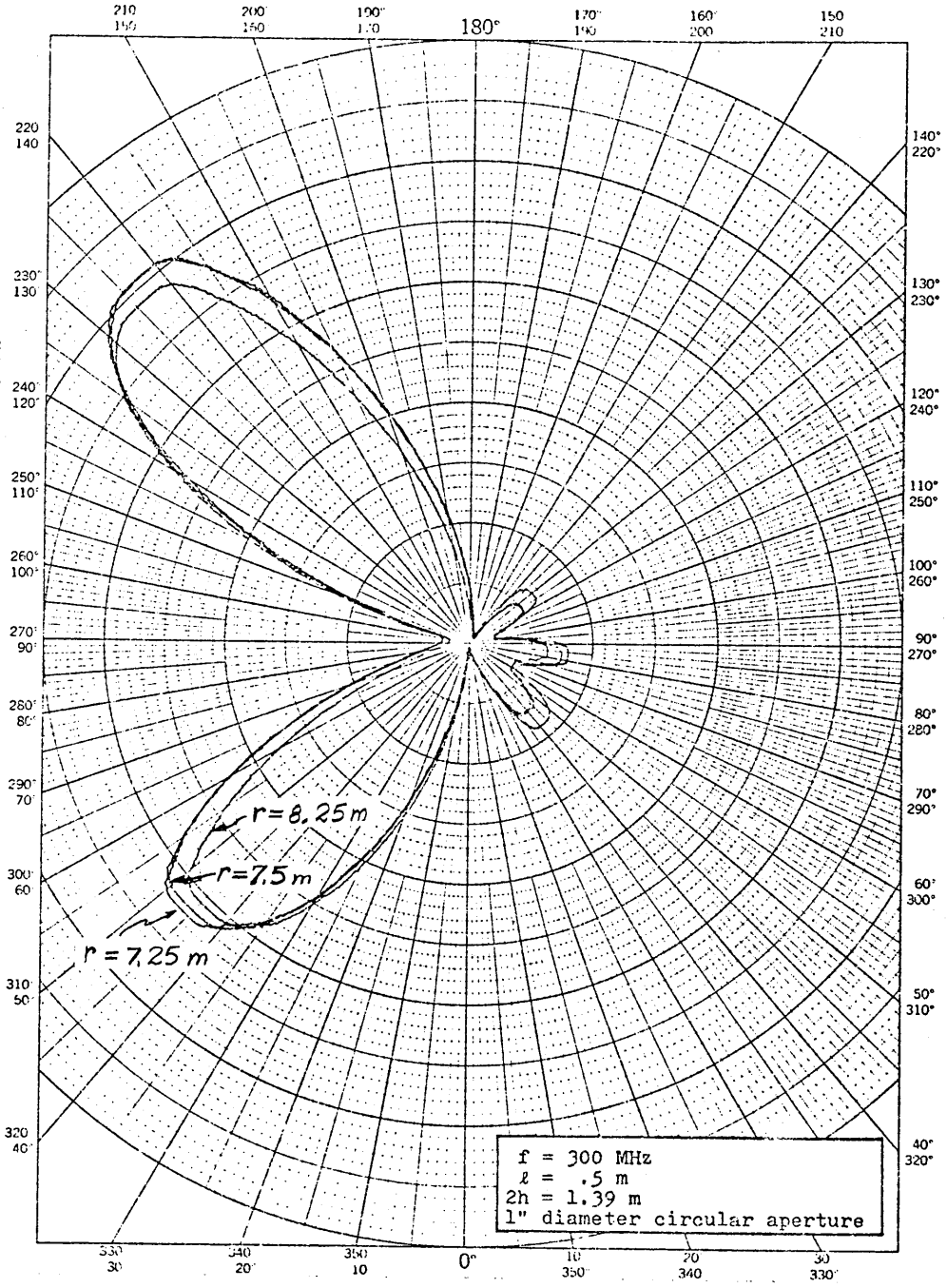

Figure 11. Power Delivered to Z_s versus θ for Three Radial Distances

with ϕ being increased from 0^{o} to 180^{o} in 30^{o} increments. The results at 300 MHz are shown in Figures 12 through 18, while the results for f = 200 MHz are shown in Figures 19 through 25. The one-inch diameter circular aperture was used for all patterns. The interior length ℓ was set at 0.5 m and the exterior length 2h was set at 1.39m.

Both series of patterns show the same azimuthal dependence on ϕ as the angle ϕ is increased, the large back lobes becoming smaller in magnitude while the small front lobes became larger in magnitude. At $\phi = 90^{o}$ (where the aperture is pointed skyward), all lobes were approximately equal in magnitude. These results would appear to indicate that the exterior current and charge density distributions were not essentially constant with respect to axial ϕ-variations, as had been assumed. This unexpected result seems to imply that even the radius of β_a=0.3 (and with apertures the order of 1 inch) is too large to allow the application of thin-wire antenna theory.

All of the solid-line patterns, taken by use of the University of Colorado outdoor antenna range at 300 MHz, and shown as the solid-line patterns in Figures 12 through 29, exhibit a lack of symmetry about the $\phi = 90^{o}$ plane, a fact which was later traced to a small degree of non-uniformity in the plane wave arriving at the model location. (This difficulty has been corrected in more recent tests.) In repeating these pattern tests at the indoor Dahlgren pattern range, it was observed that near-symmetry about the $\phi = 90^{o}$ does in fact exist at 300 MHz for the model, as corroborated by the typical dashed-line pattern results included for comparison purposes on the $\phi=0^{o}$ and $\phi = 90^{o}$ "cuts" shown in Figures 12 and 15. At 200 MHz, however, a definite asymmetry about the $\phi = 90^{o}$ plane is in evidence, and the correspondence between the results obtained at

the University of Colorado and the Dahlgren ranges is closer, as seen from the typical comparison of the solid- and dashed-line results graphed for the $\phi = 0^{o}$ case on Figure 19.

At an operating frequency of 200 MHz, the anticipated asymmetry about $\theta = 0^{o}$ is not as strong as for 300 MHz. This is evidently due to the much greater relative contribution from the equivalent electric dipole, which is proportional to an anti-symmetric charge density distribution, and thus does not exhibit the axially asymmetric properties characterizing the equivalent magnetic dipole. Also, at 200 MHz, the offset distance of the aperture from the center of the experimental model was smaller (compared to the wavelength), yielding a smaller degree of asymmetry relative to the magnetic equivalent dipole.

2.1.3 Effect of Interior Cavity Length on Field Patterns A study of the analytical solutions discussed in Appendices A and B shows that when the distance ℓ from the center of the aperture to the load impedance Z_0 is one-quarter wavelength, only the electric equivalent dipole contributes to current in the load Z_s; while when ℓ is one-half wavelength, only the magnetic dipole contributes to the current in Z_s. Since the exterior current distribution has a maximum at the center of the length of cylinder when the cylinder is three-halves of a wavelength long ($f = 300$ MHz), the charge density distribution has a minimum there ($\rho(z) \sim \frac{\partial}{\partial z} I(z)$). Thus, at 300 MHz the equivalent electric dipole has a very small magnitude when compared to the magnetic equivalent dipole. However, at an operating frequency of 200 MHz, the current distribution has a minimum at the center of the cylinder length while the charge density distribution reaches a

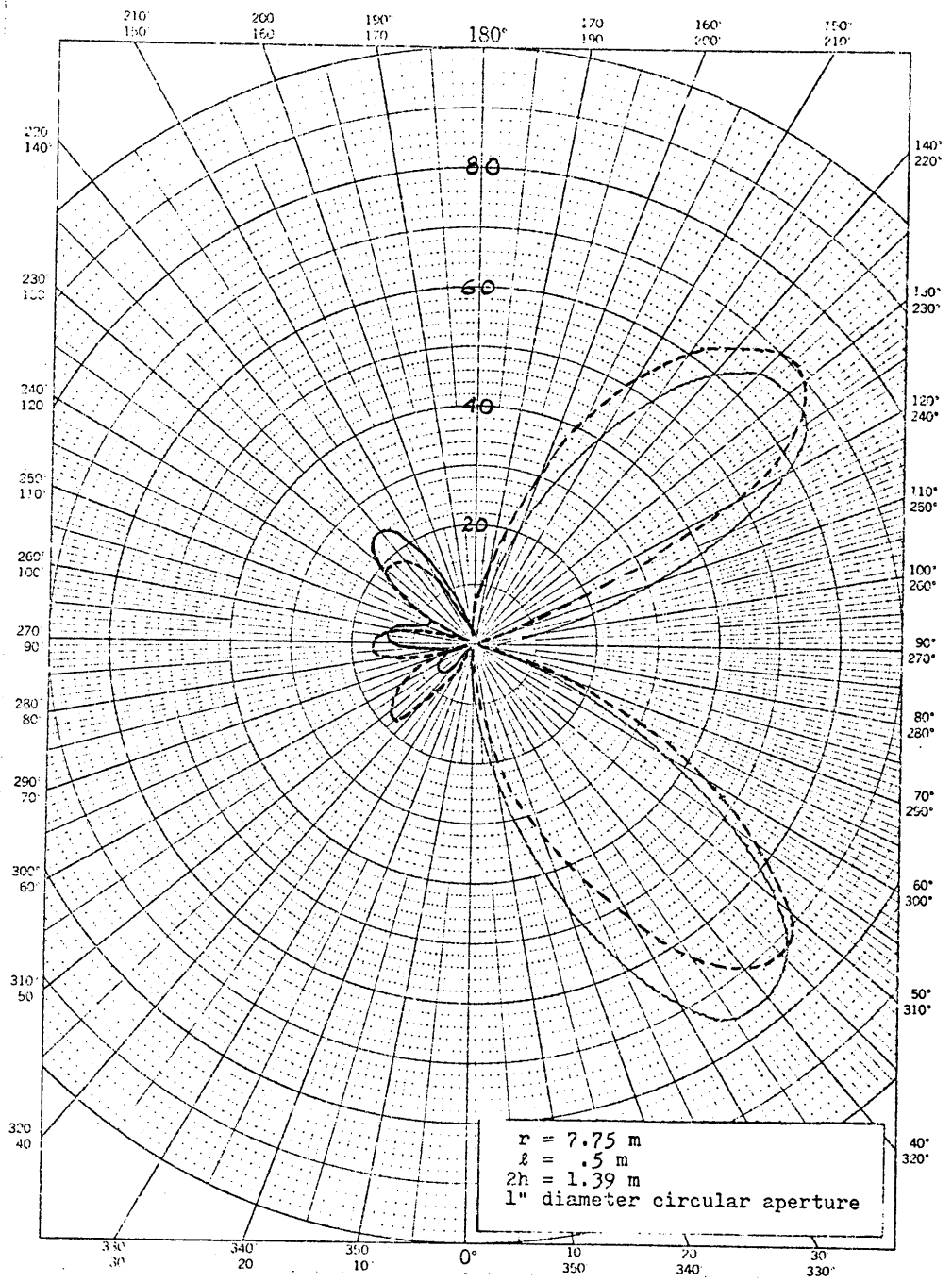

Figure 12. Power Delivered to Z_s versus θ for $\phi = 0^\circ$ at 300 MHz.
Solid Line: From Univ. of Colo. pattern range.
Dashed: From Dahlgren pattern range.

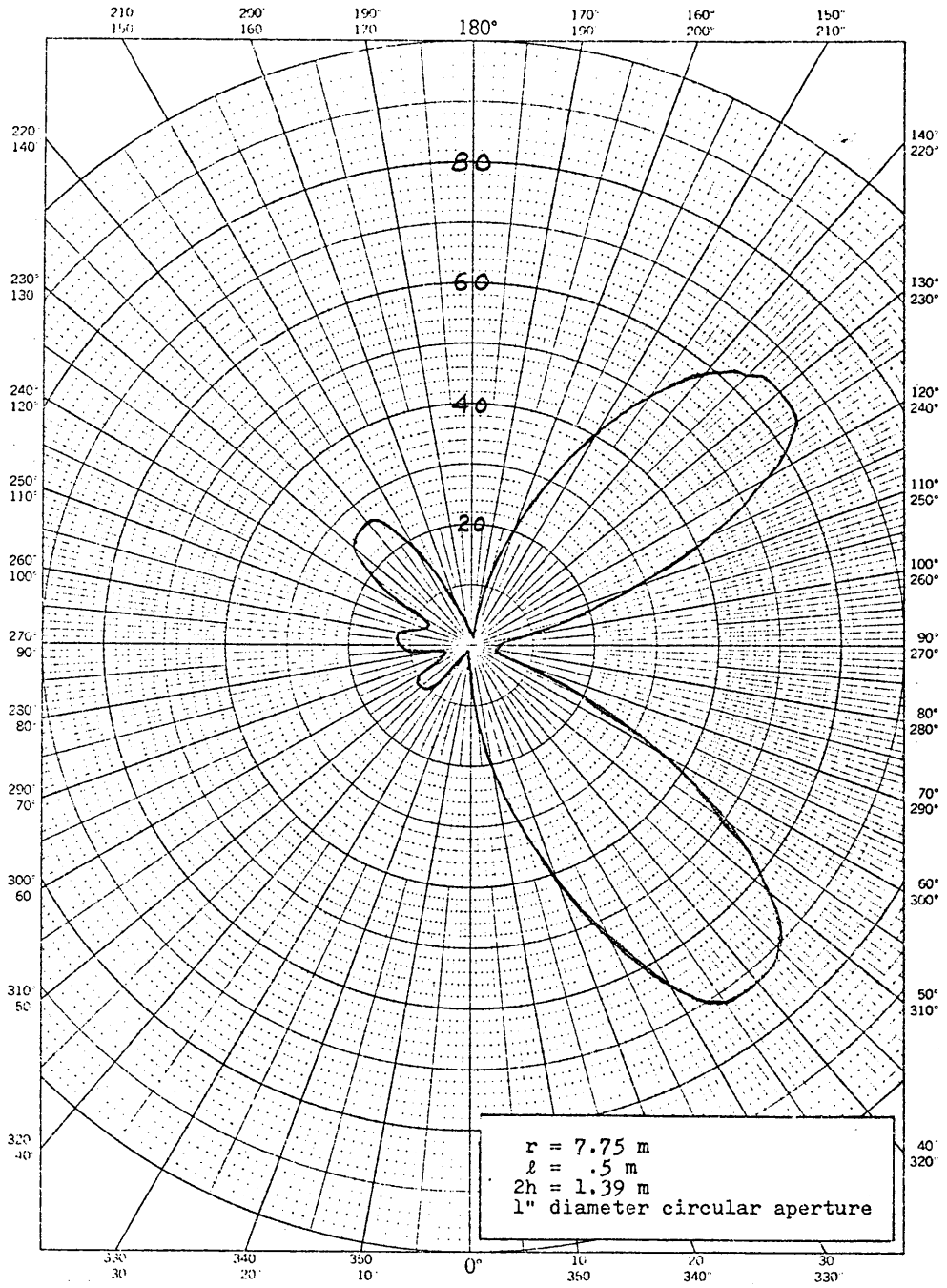

Figure 13. Power Delivered to Z_s versus θ for $\phi = 30^c$ at 300 MHz

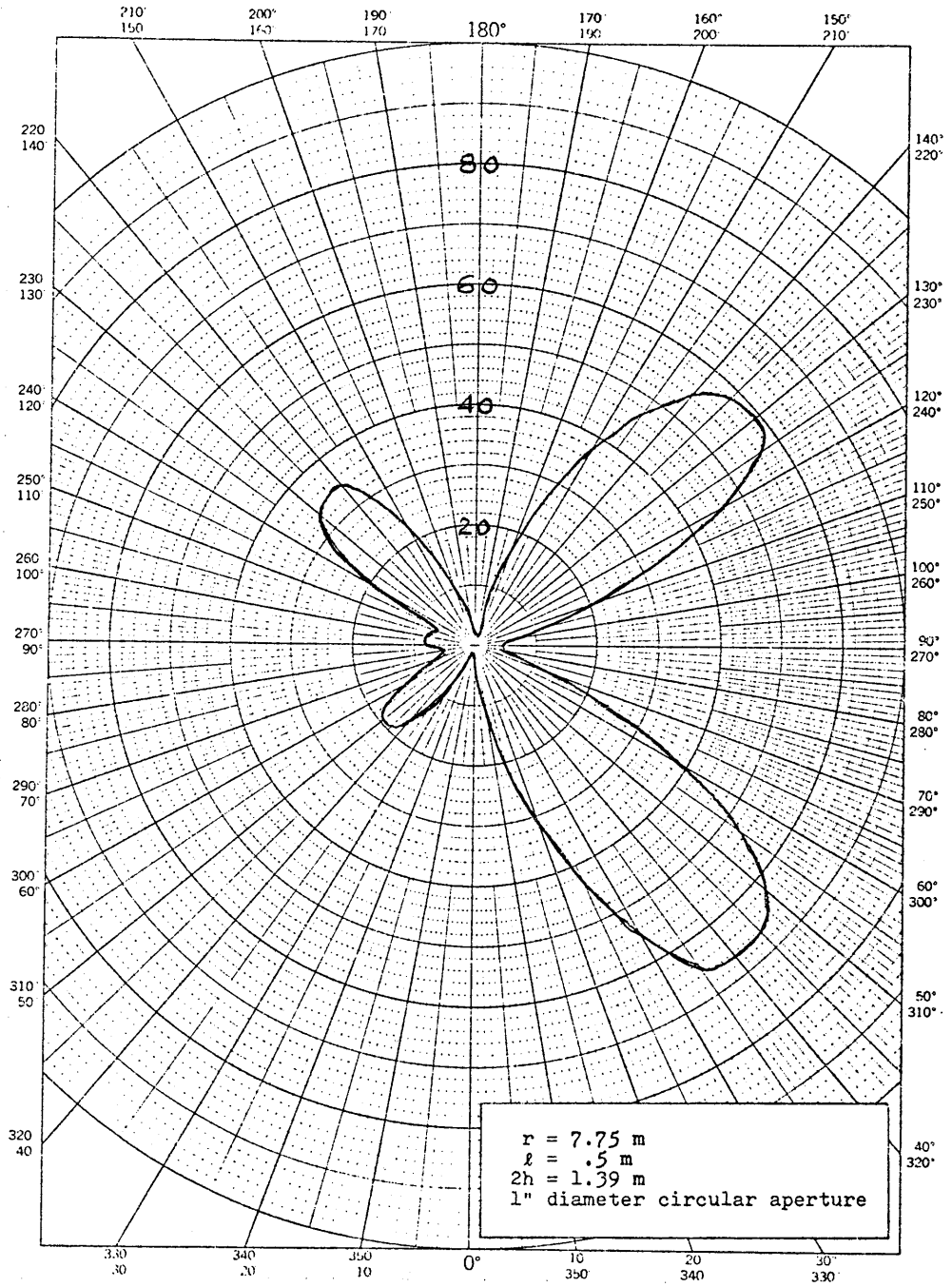

Figure 14. Power Delivered to Z_s versus θ for $\phi = 60^{\circ}$ at 300 MHz

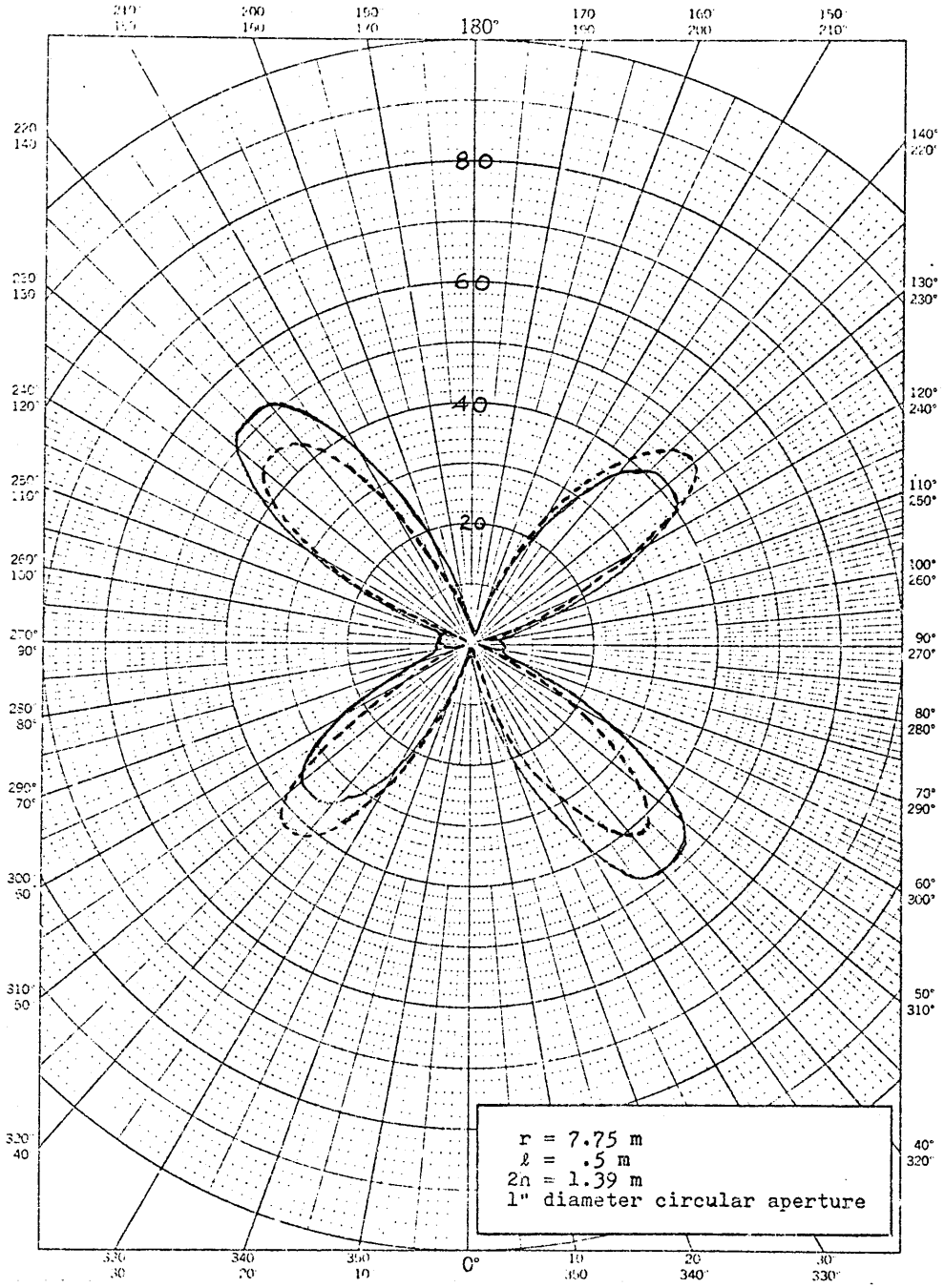

Figure 15. Power Delivered to Z_s versus θ for $\phi = 90^\circ$ at 300 MHz.
Solid line: From Univ. of Colo. pattern range.
Dashed: From Dahlgren pattern range.

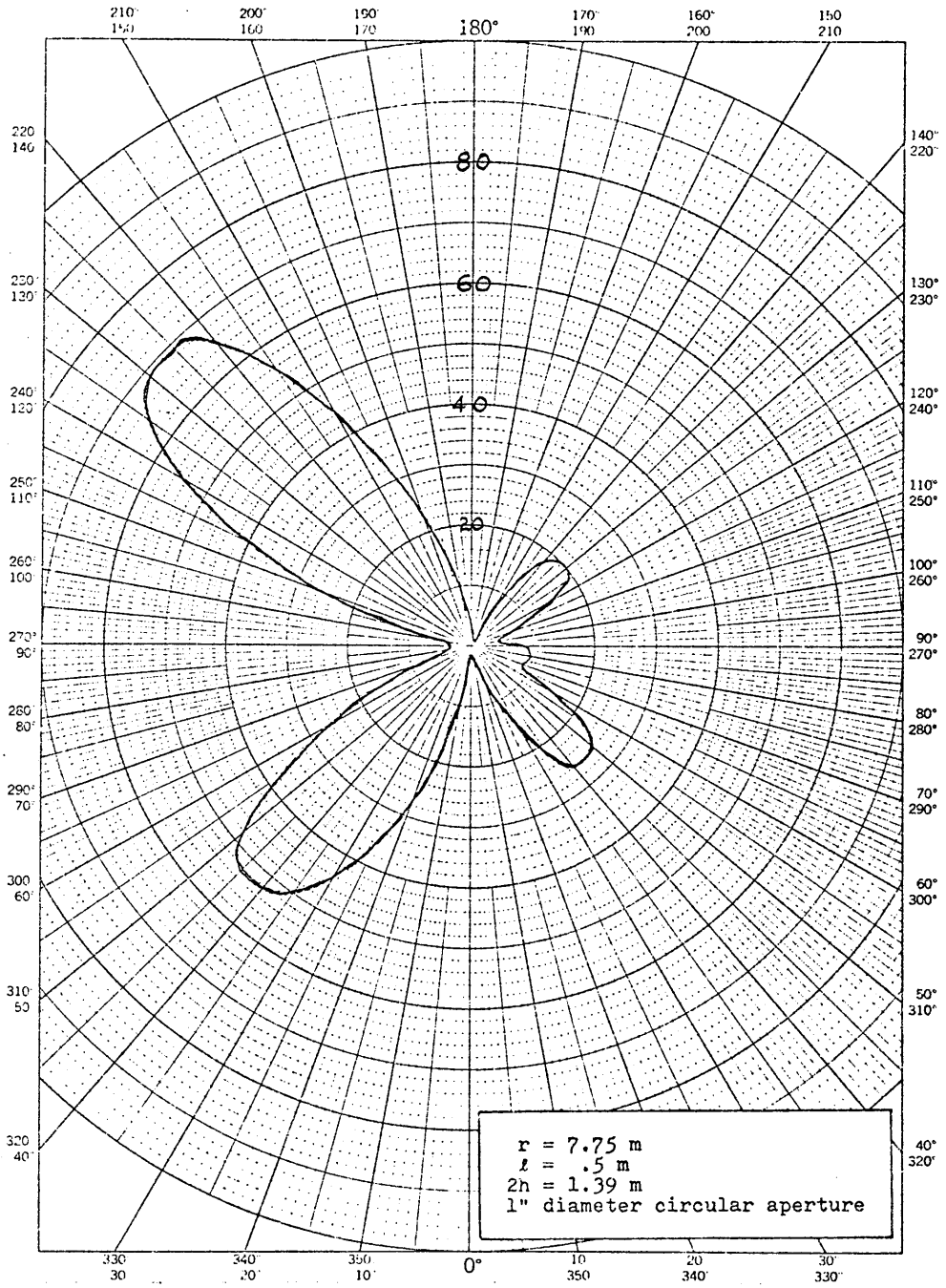

Figure 16. Power Delivered to Z_s versus θ for $\phi = 120^{\circ}$ at 300 MHz

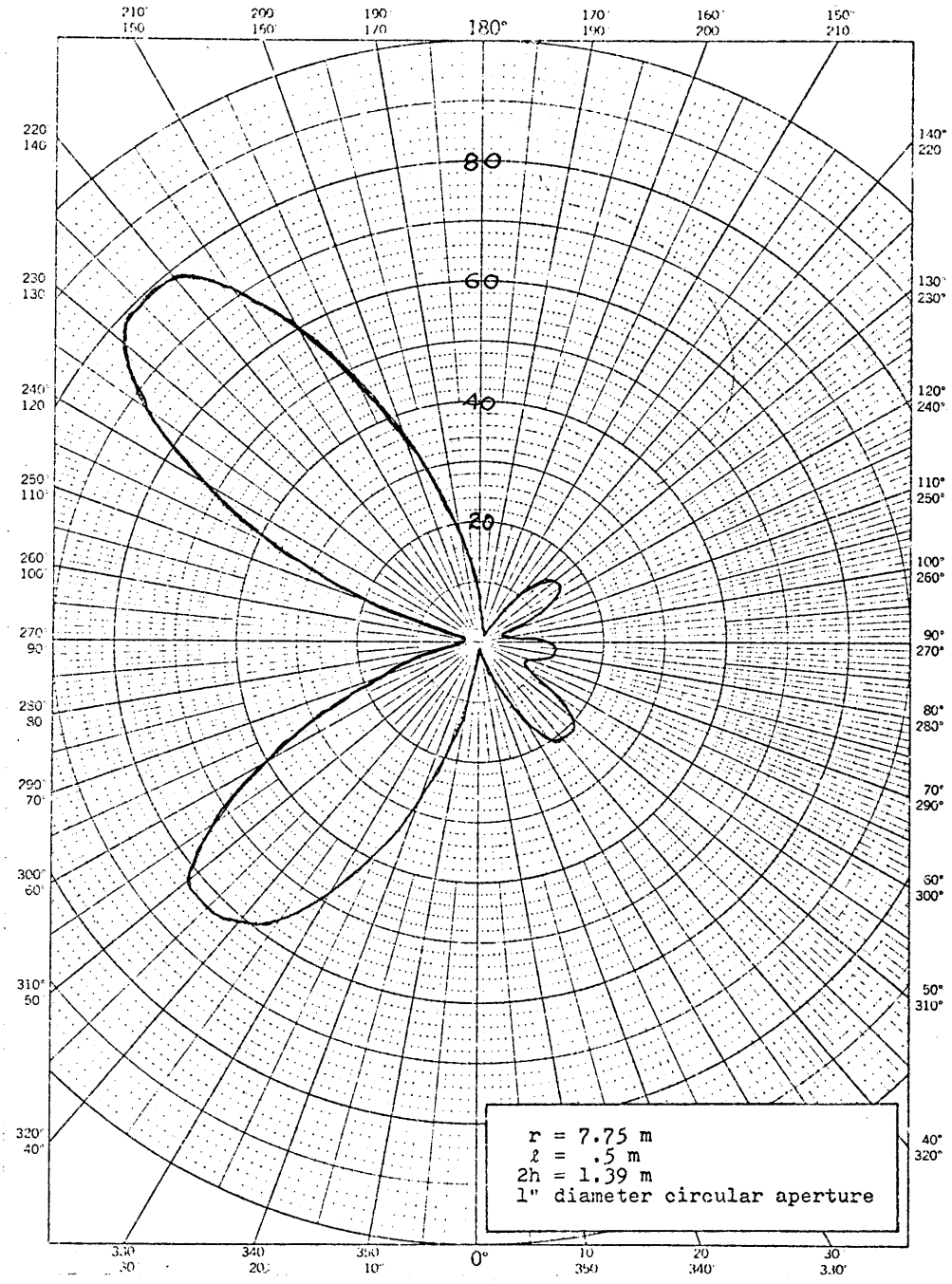

Figure 17. Power Delivered to Z_s versus θ for $\phi = 150^{\circ}$ at 300 MHz

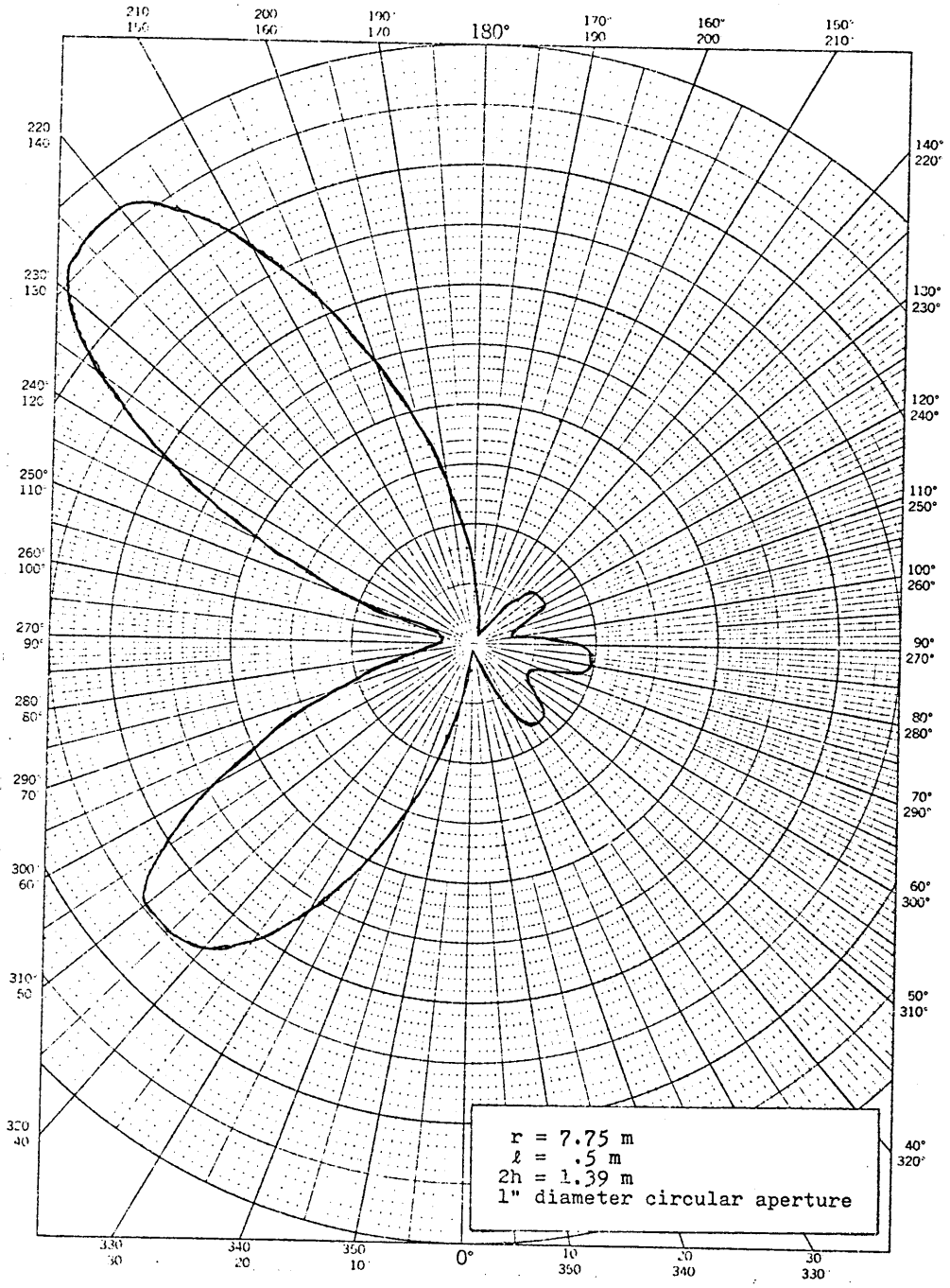

Figure 18. Power Delivered to Z_s versus θ for $\phi = 180^{o}$ at 300 MHz

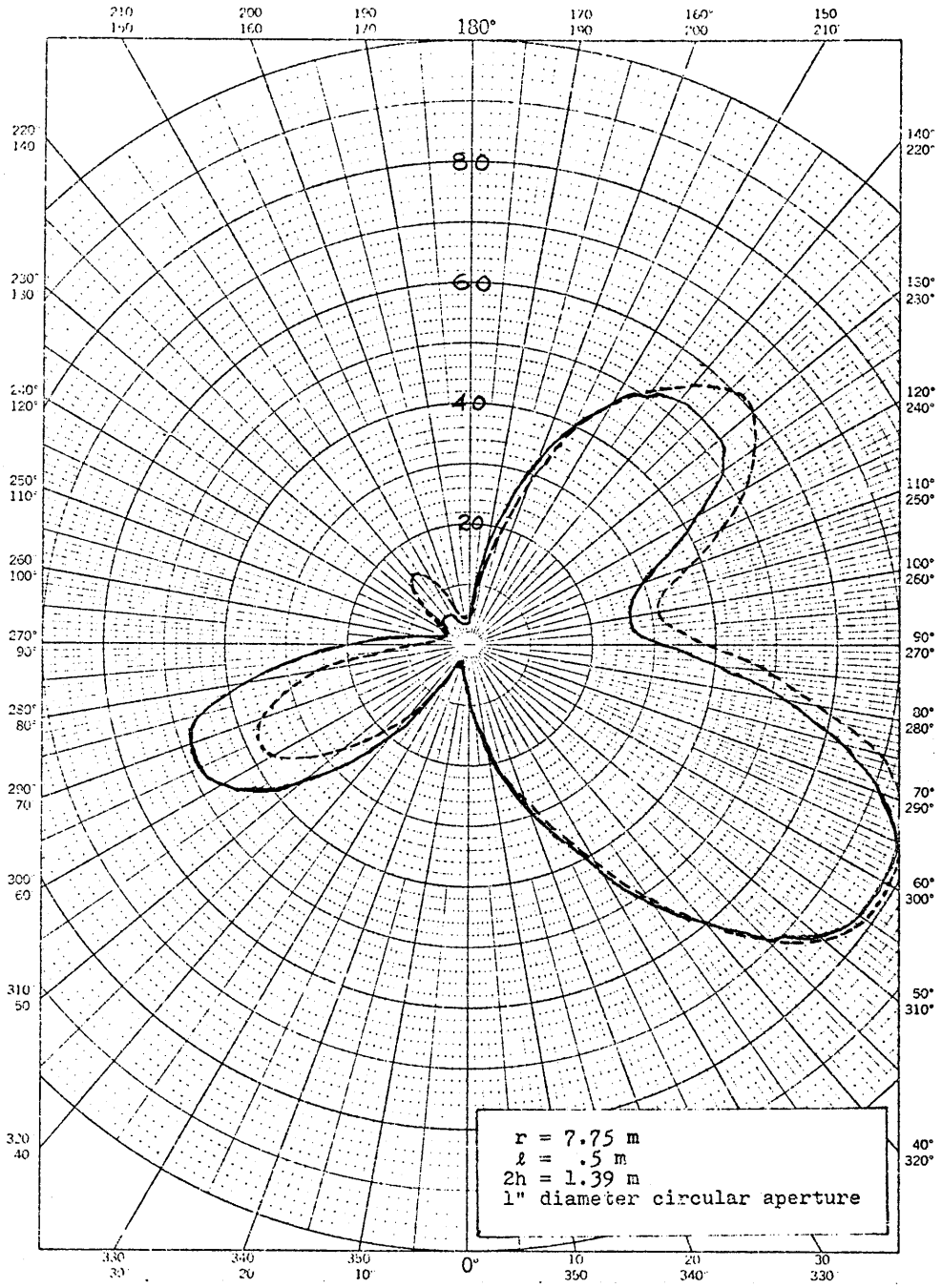

Figure 19. Power Delivered to Z_s versus θ for $\phi = 0^{\circ}$ at 200 MHz.
Solid line: From Univ. of Colo. pattern range.
Dashed: From Dahlgren pattern range.

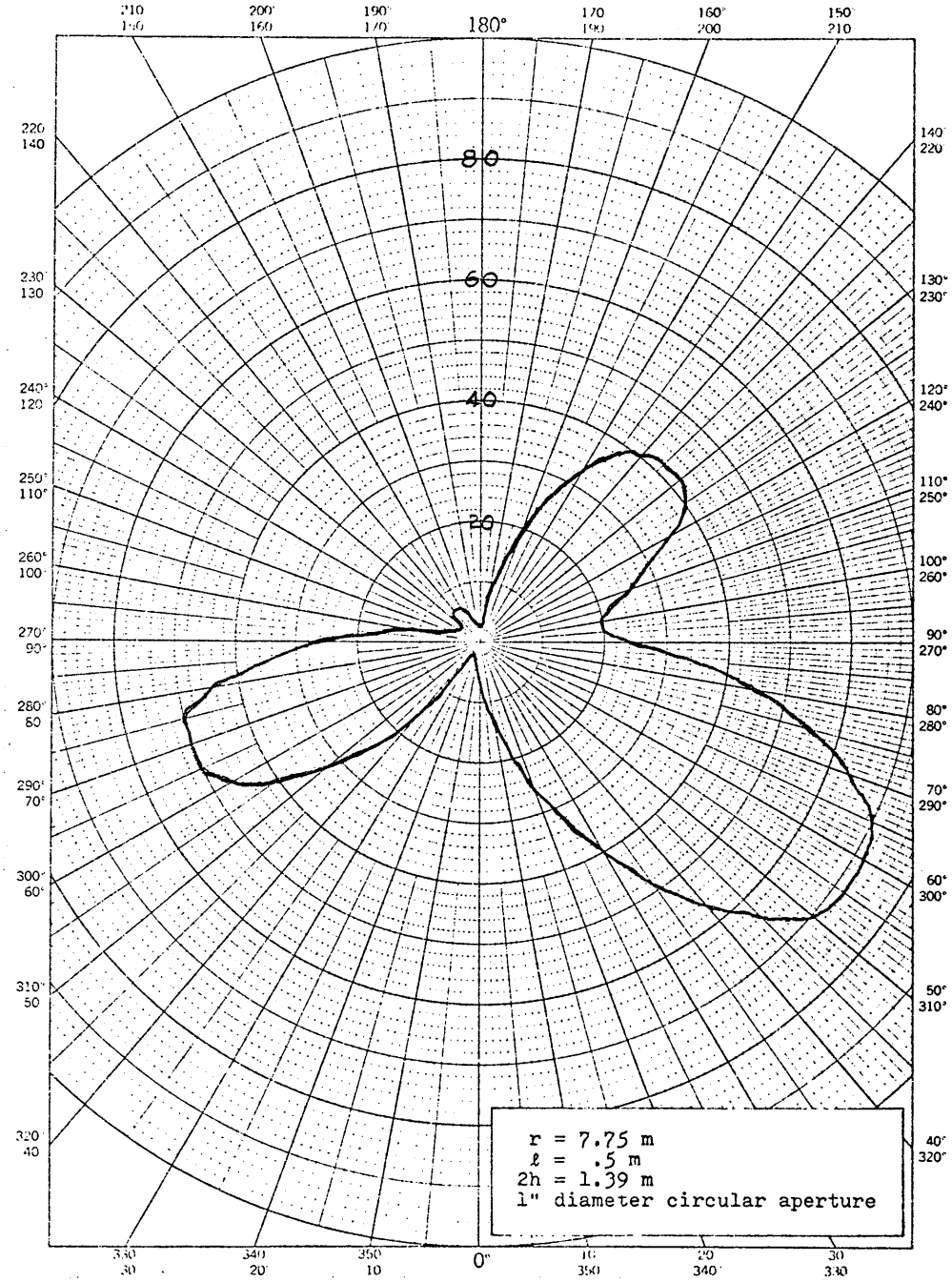

Figure 20. Power Delivered to Z_s versus θ for $\phi = 30^{\circ}$ at 200 MHz

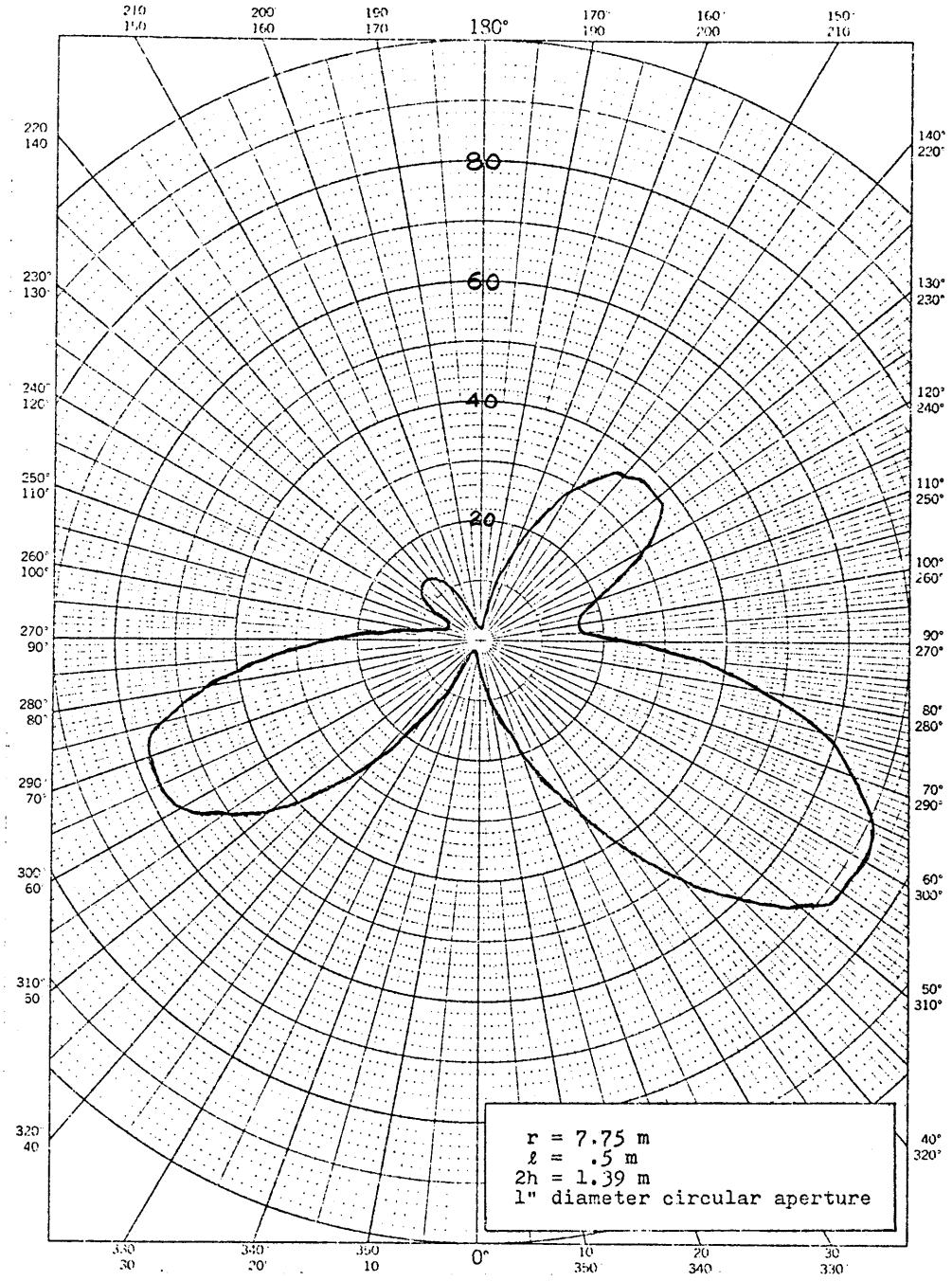

Figure 21. Power Delivered to Z_s versus θ for $\phi = 60^{\circ}$ at 200 MHz

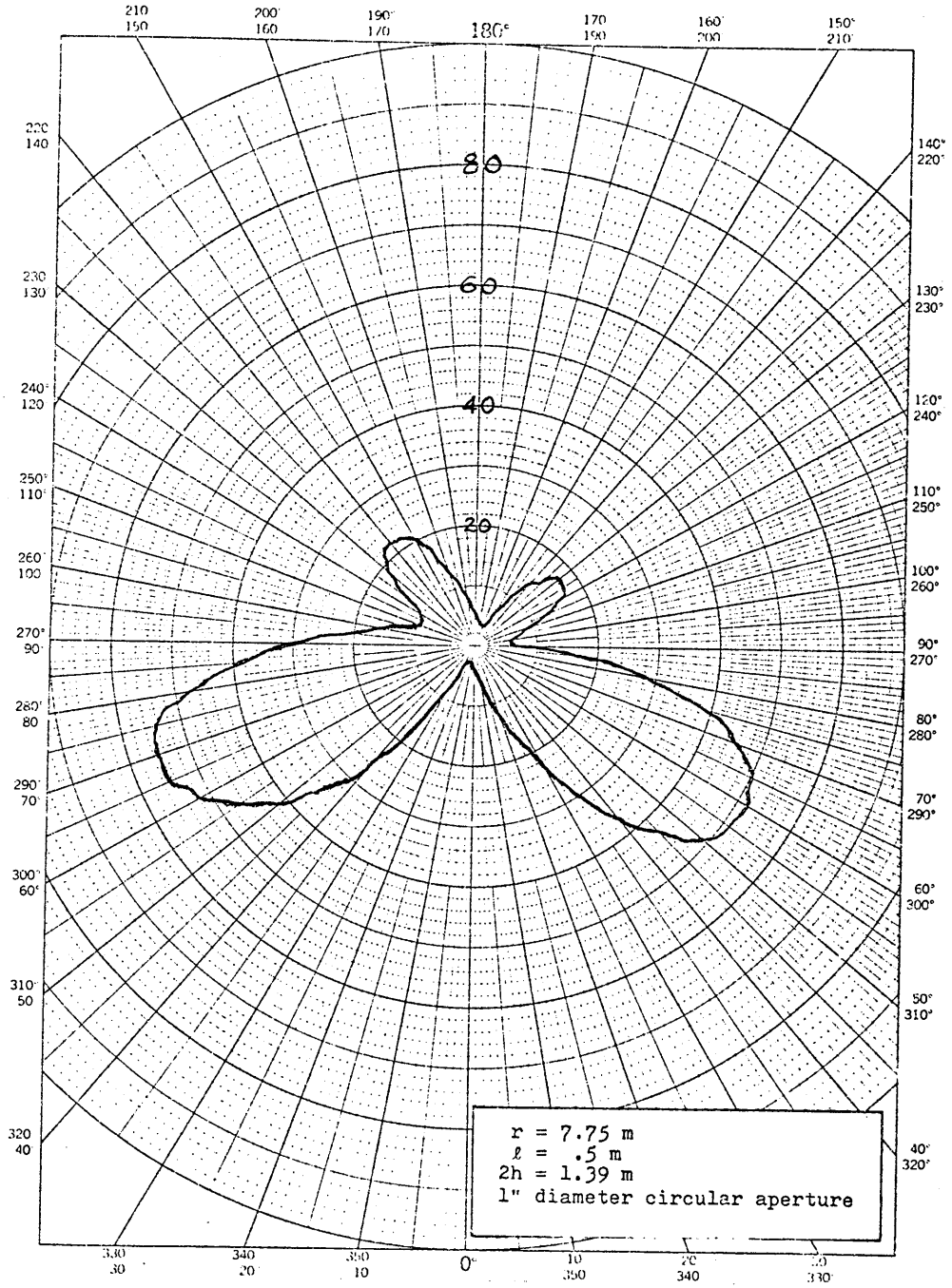

Figure 22. Power Delivered to Z_s versus θ for $\phi = 90^{o}$ at 200 MHz

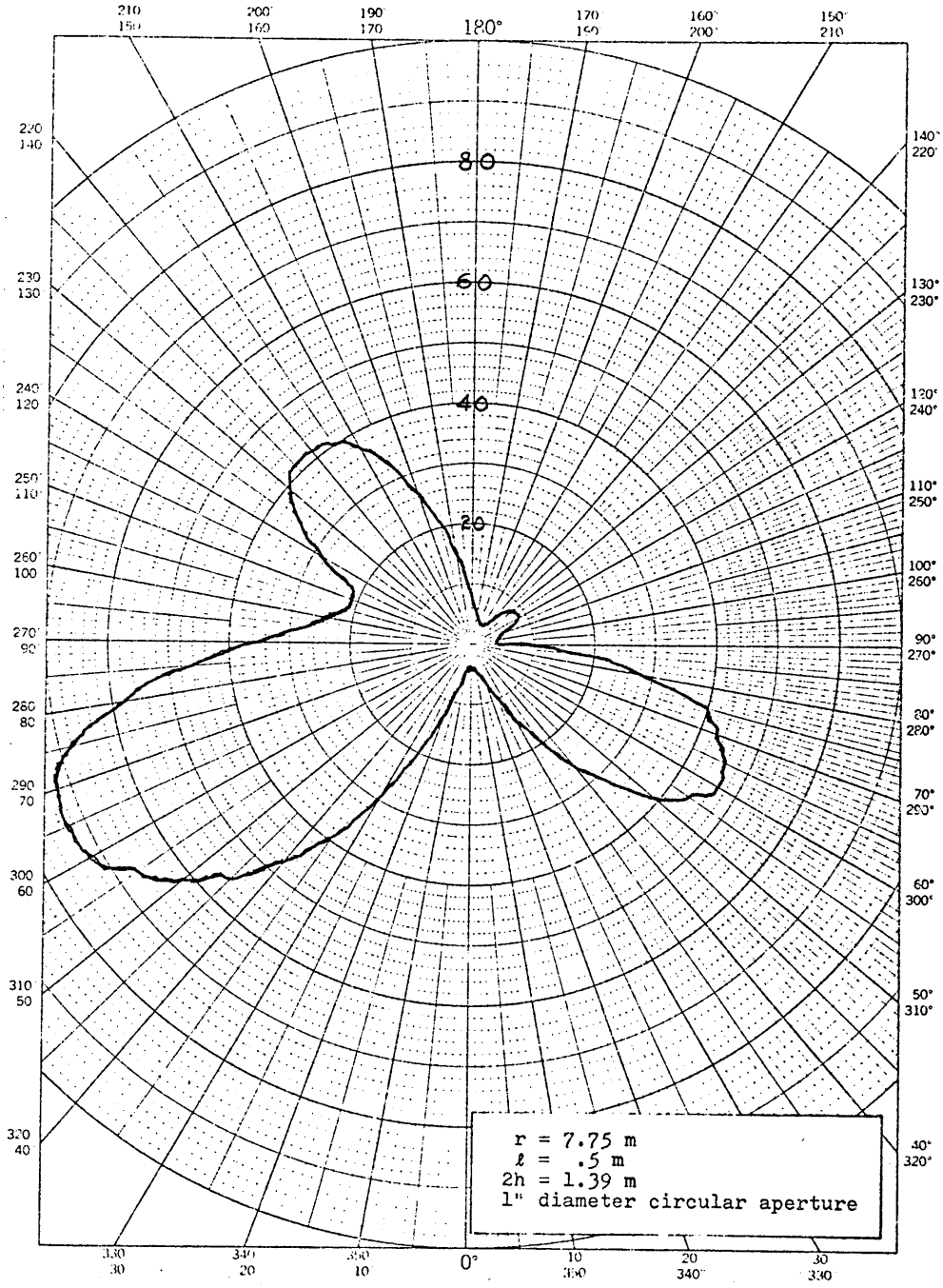

Figure 23 . Power Delivered to Z_s versus θ for $\phi = 120^{o}$ at 200 MHz

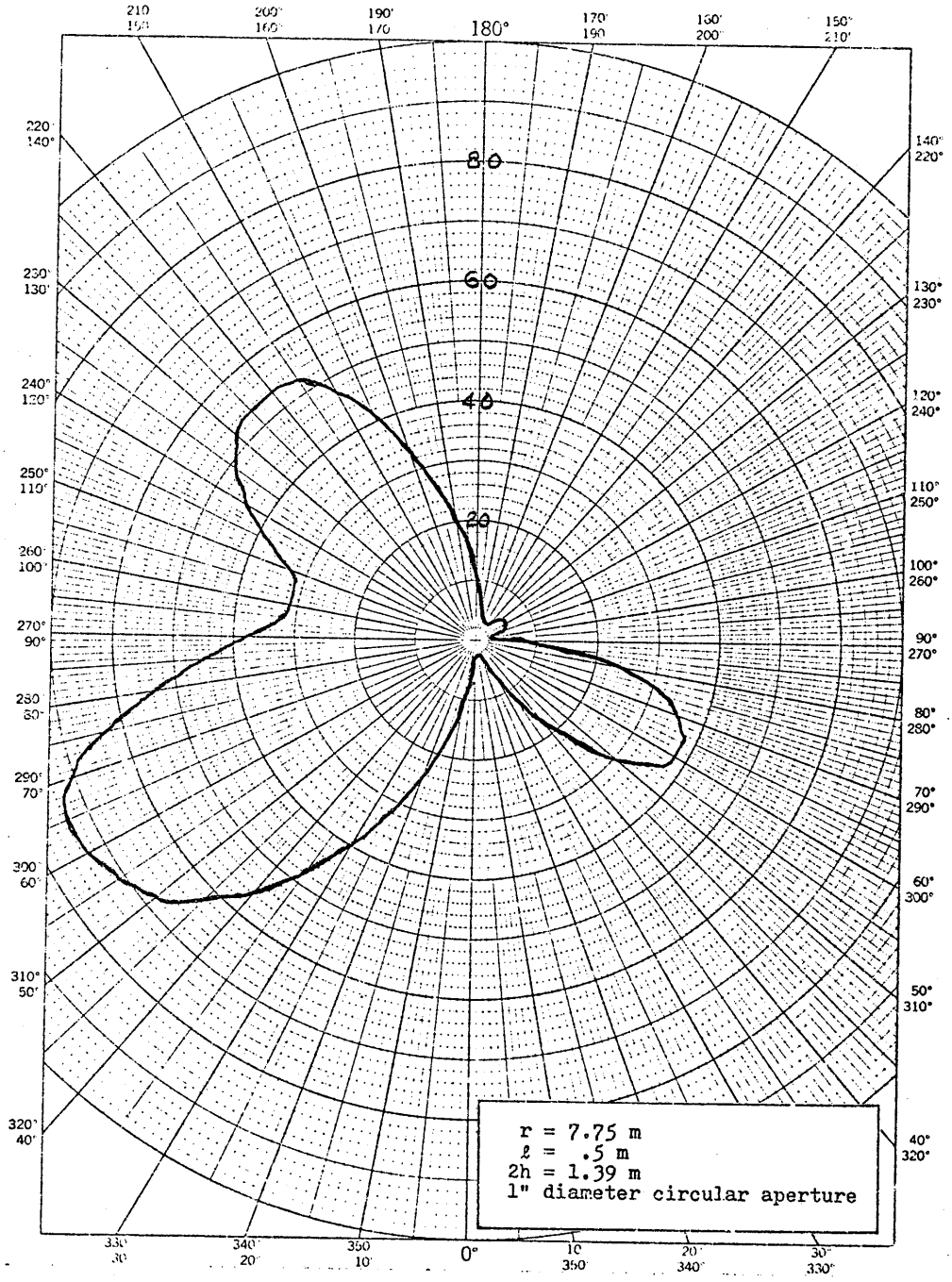

Figure 25. Power Delivered to Z_s versus θ for $\phi = 180^{\circ}$ at 200 MHz

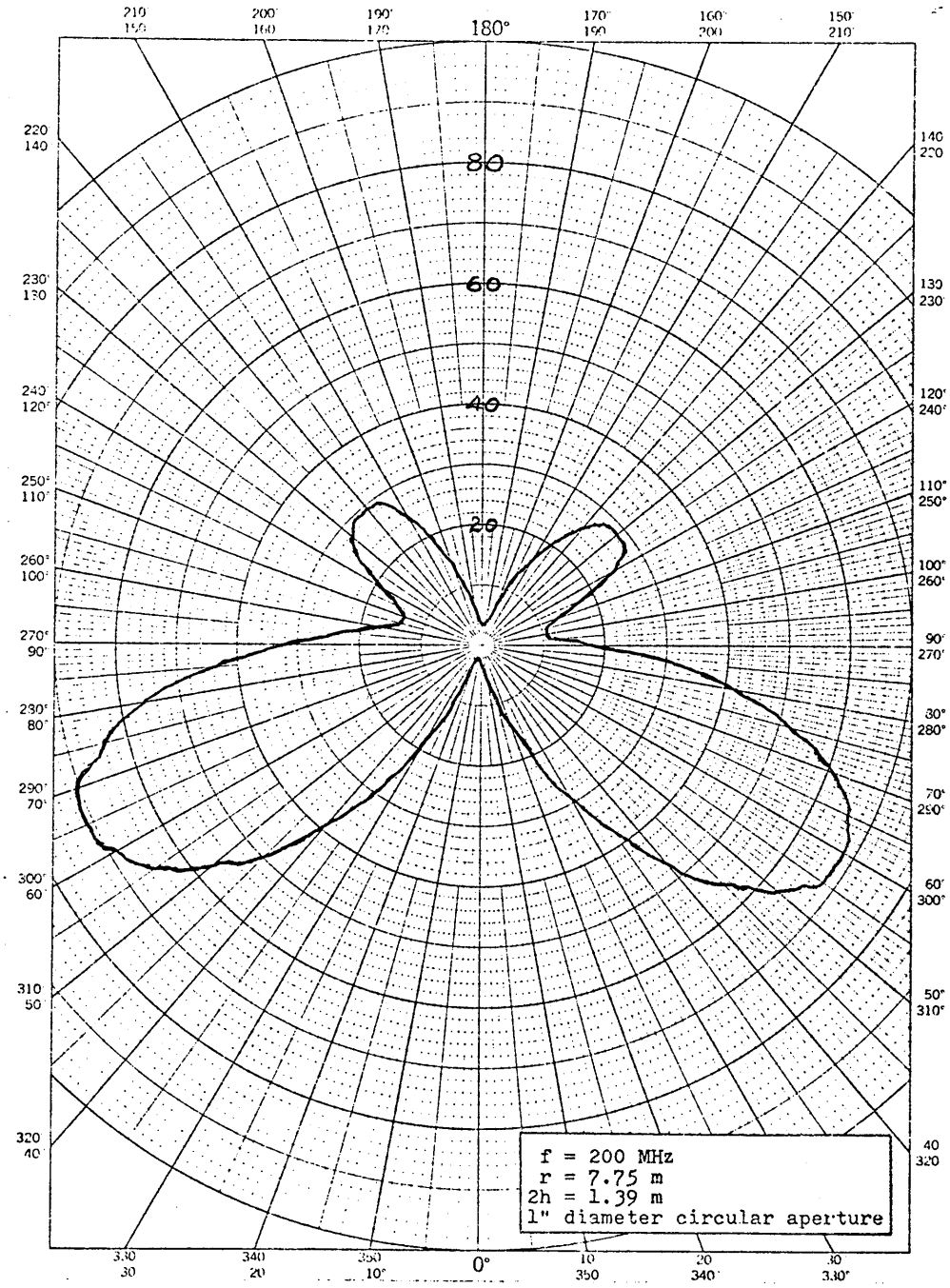

Figure 26. Power Delivered to Z_s versus θ for ℓ = .5 m at $\phi = 90^o$

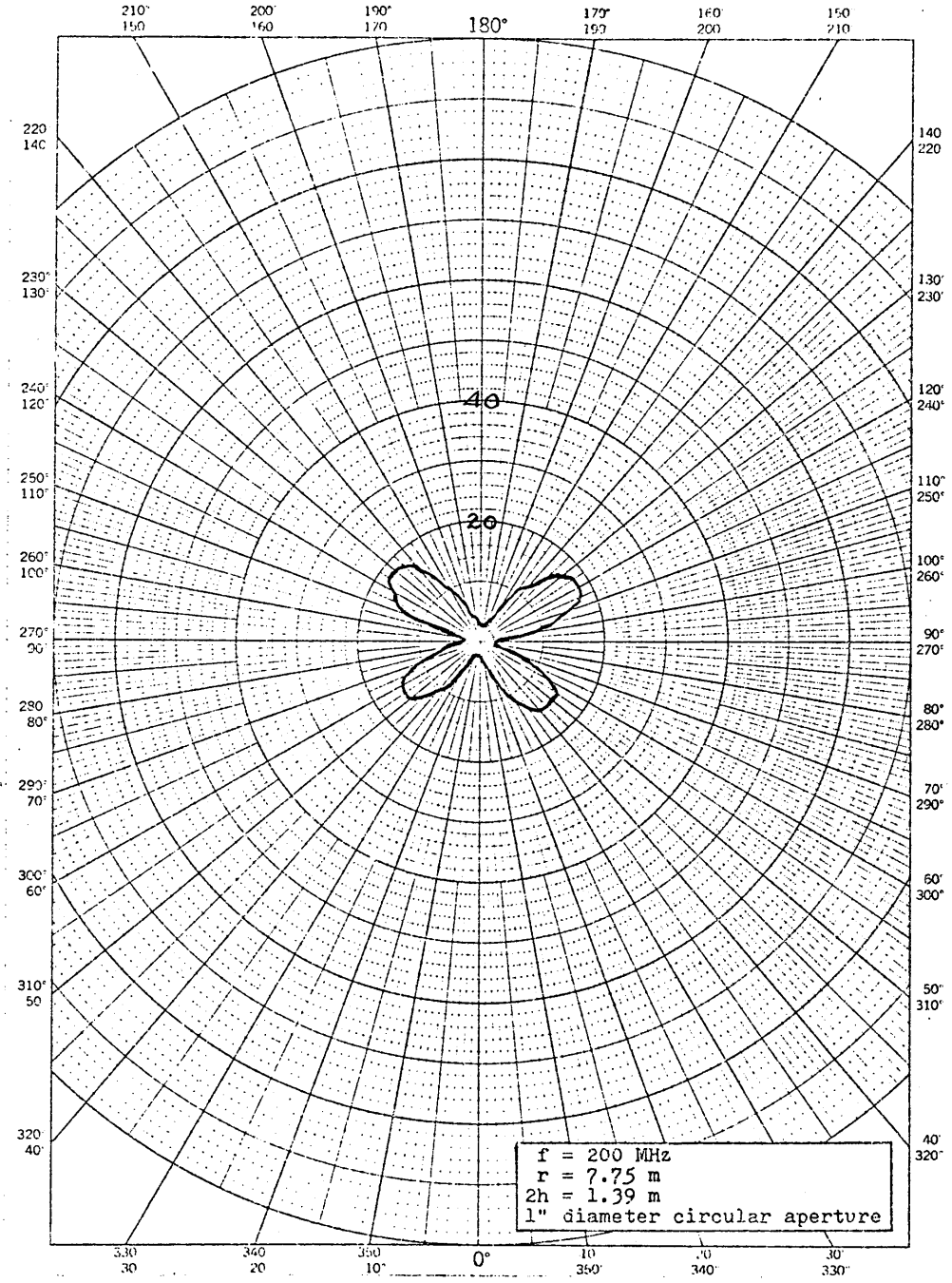

Figure 27. Power Delivered to Z_s versus θ for ℓ = .375 m at $\phi = 90^o$

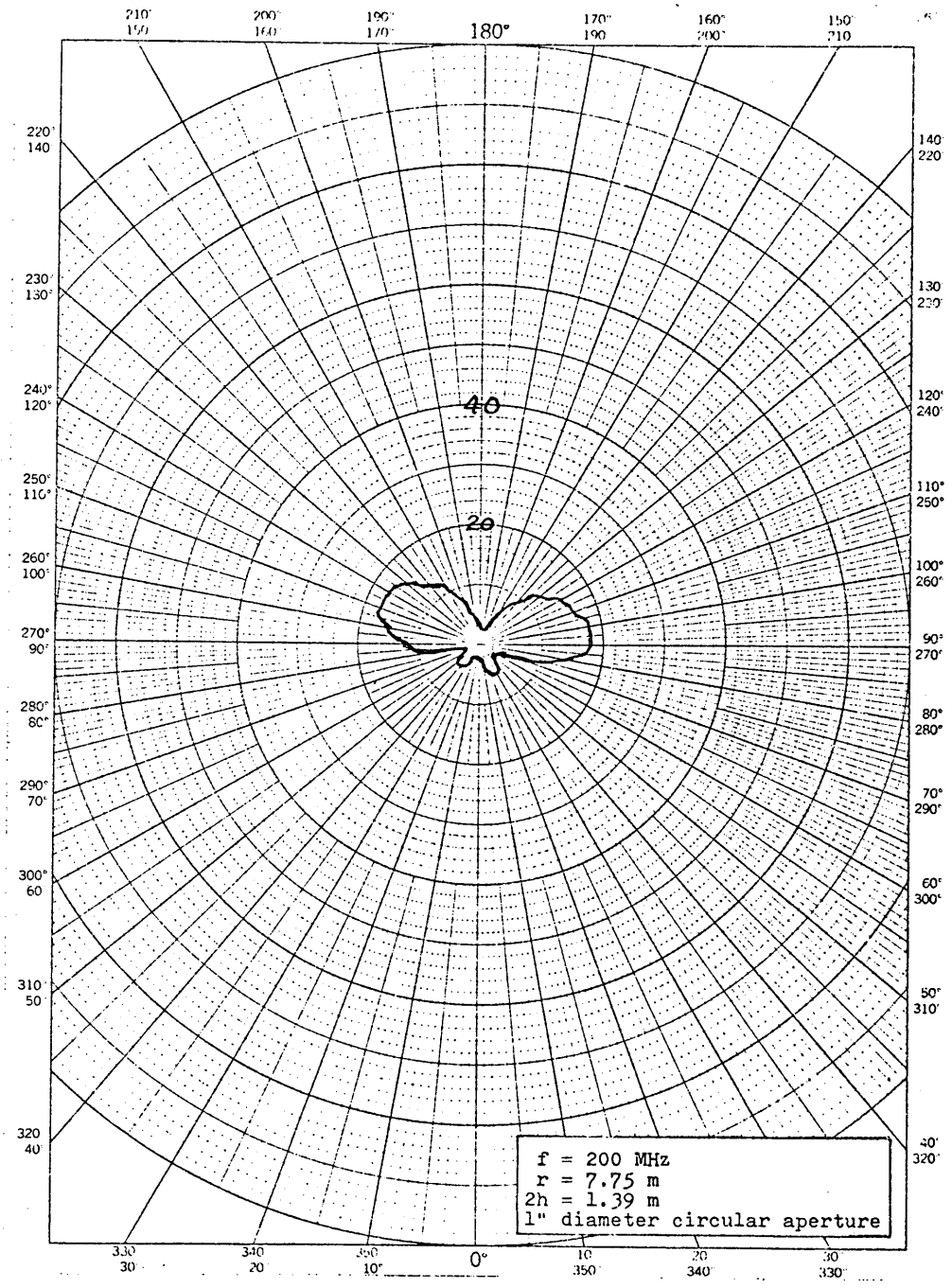

Figure 28 . Power Delivered to Z_S versus θ for ℓ = .25 m at $\phi = 90^{o}$

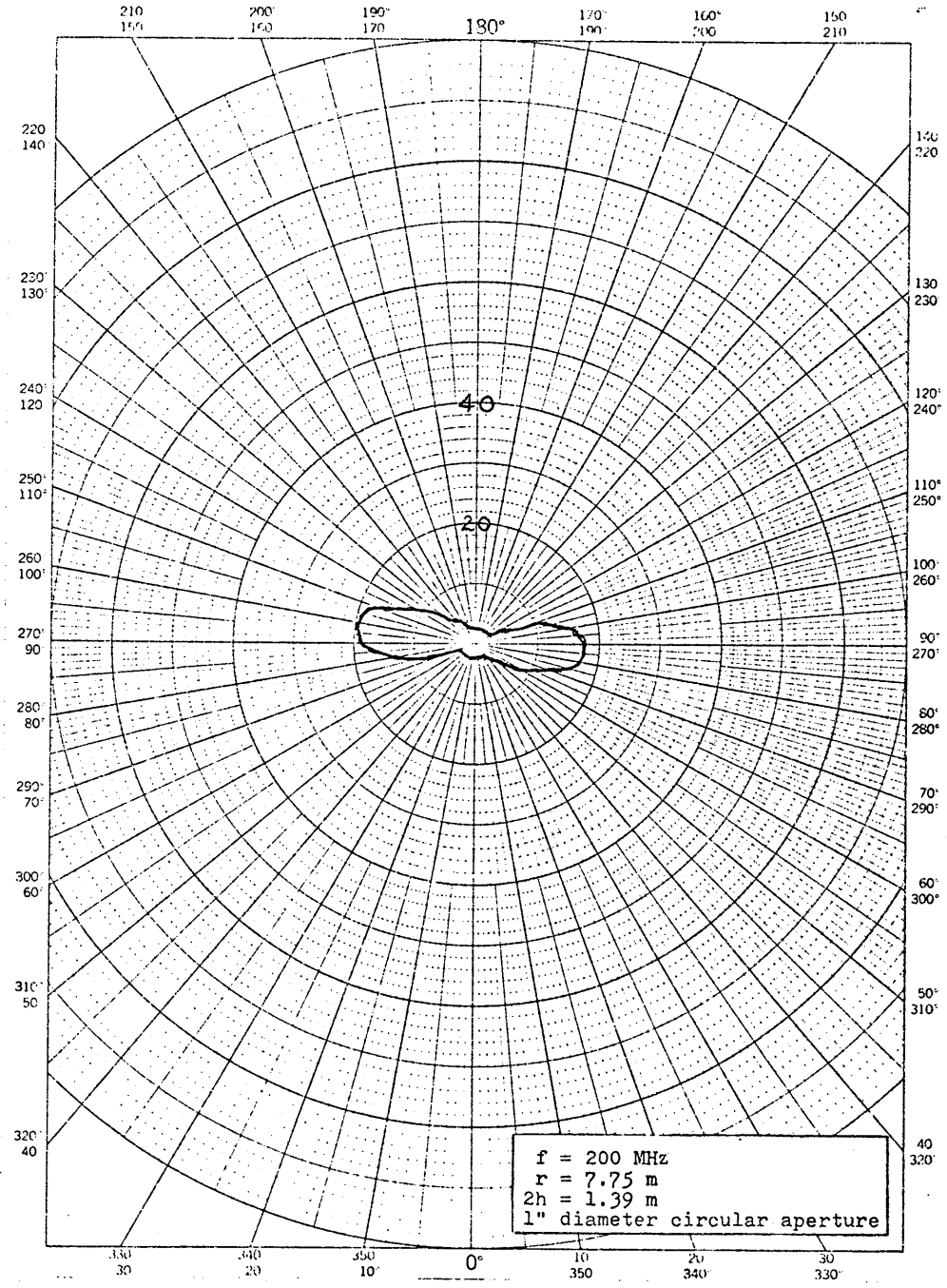

Figure 29 . Power Delivered to Z_s versus θ for ℓ = .125 m at $\phi = 90^{o}$

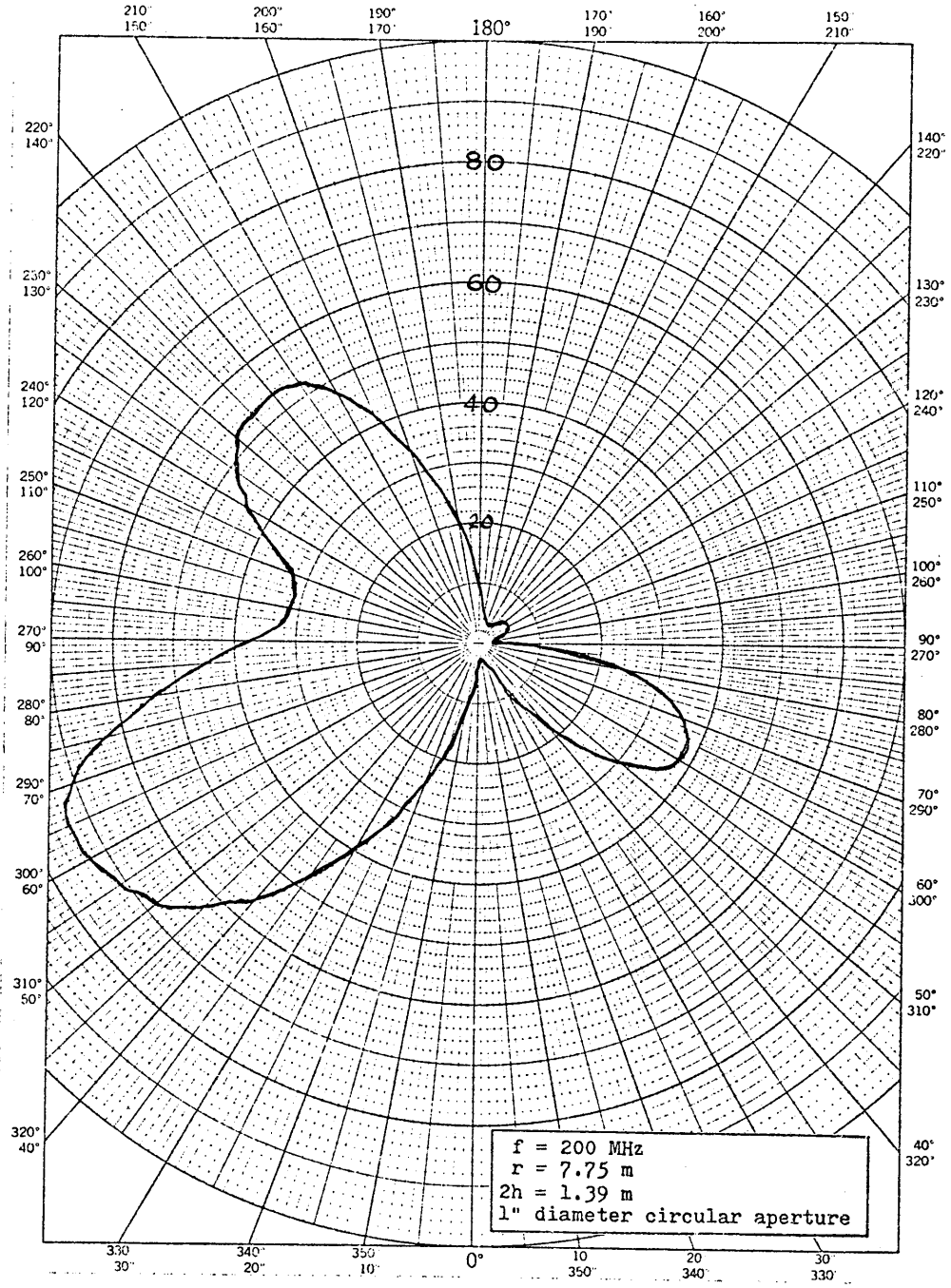

Figure 30. Power Delivered to Z_s versus θ for ℓ = .5 m at $\phi = 180^{o}$

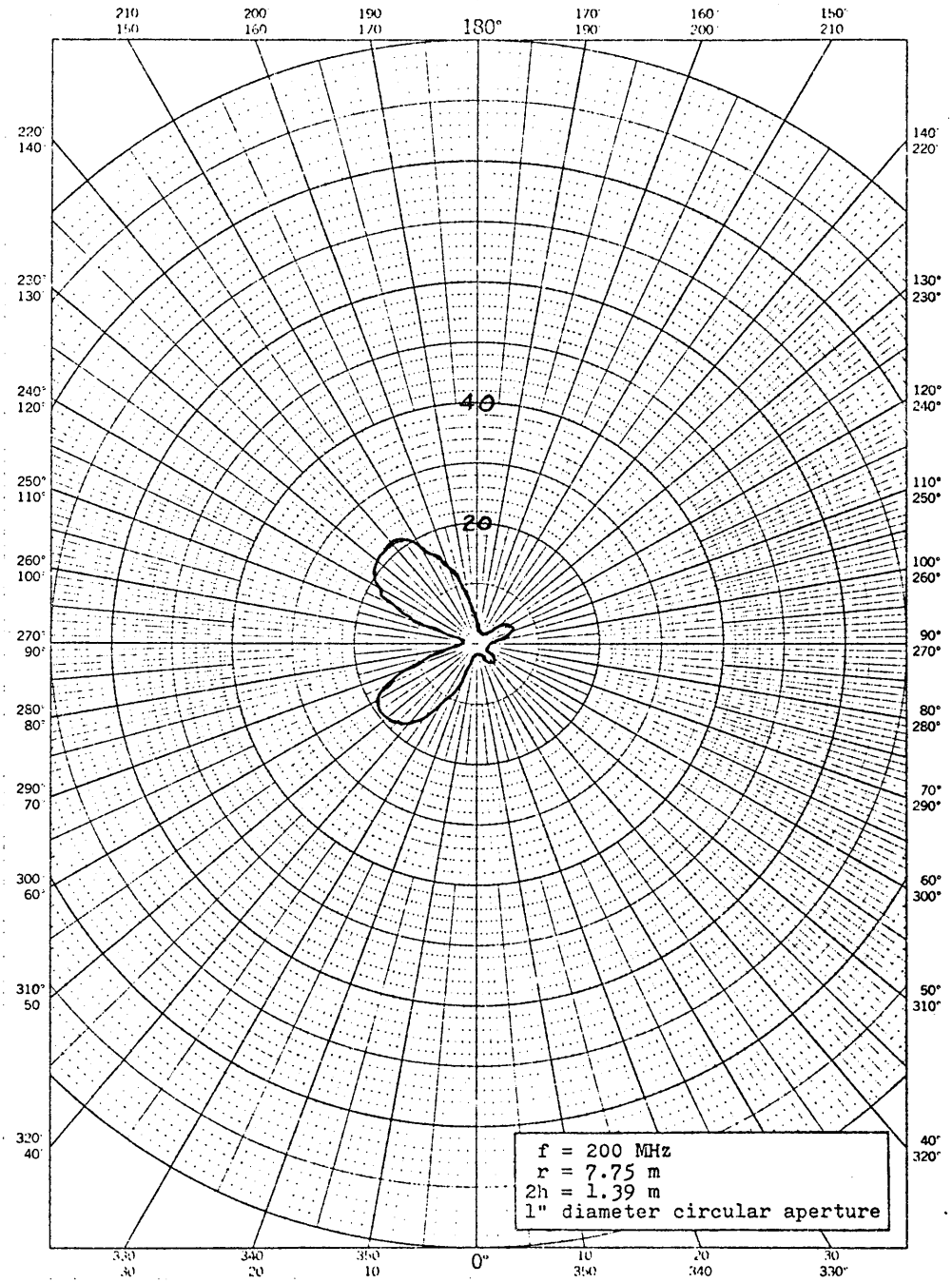

Figure 31. Power Delivered to Z_s versus θ for ℓ = .375 m at ϕ = 180°

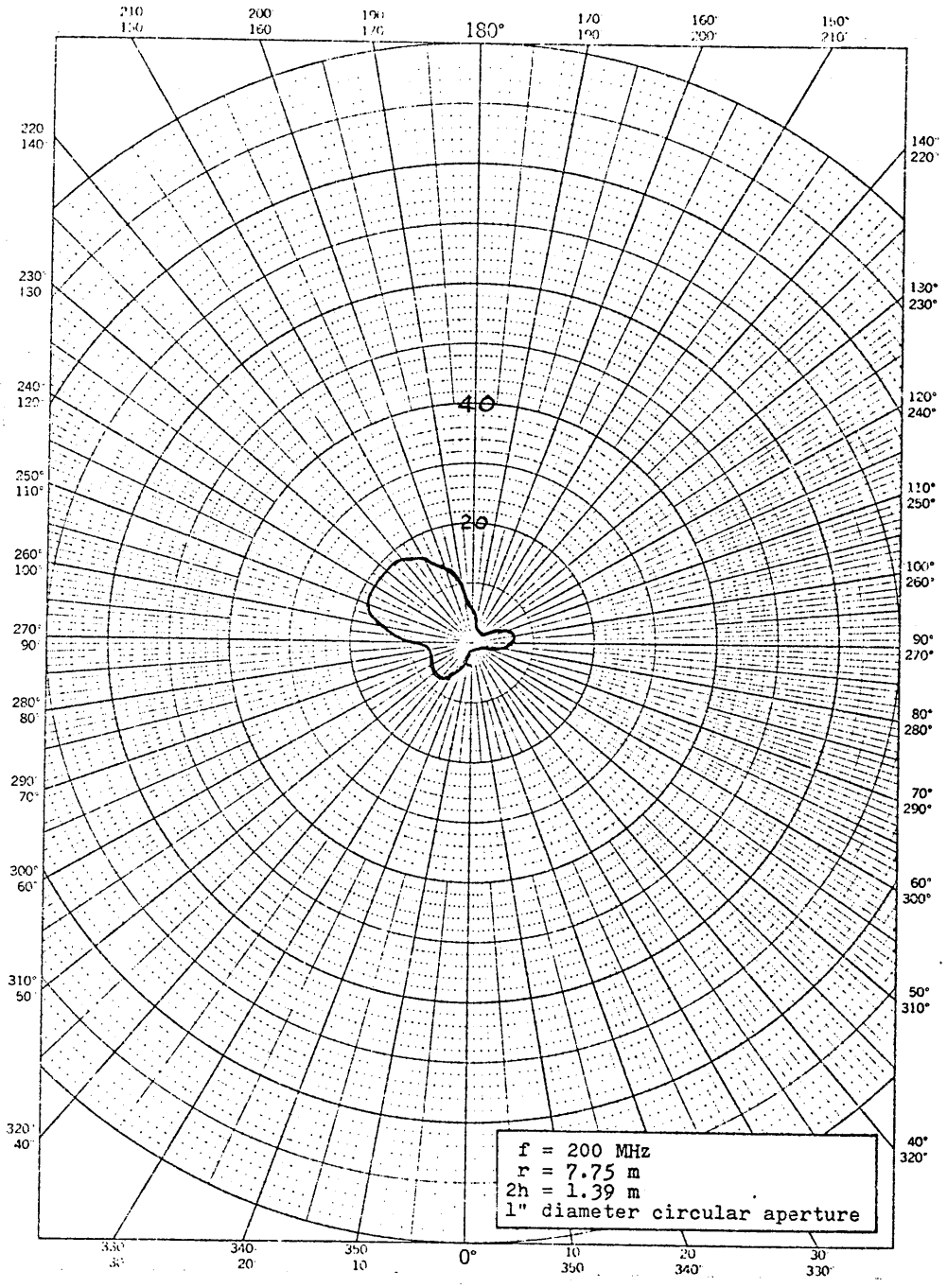

Figure 32. Power Delivered to Z_s versus θ for ℓ = .25 m at $\phi = 180^o$

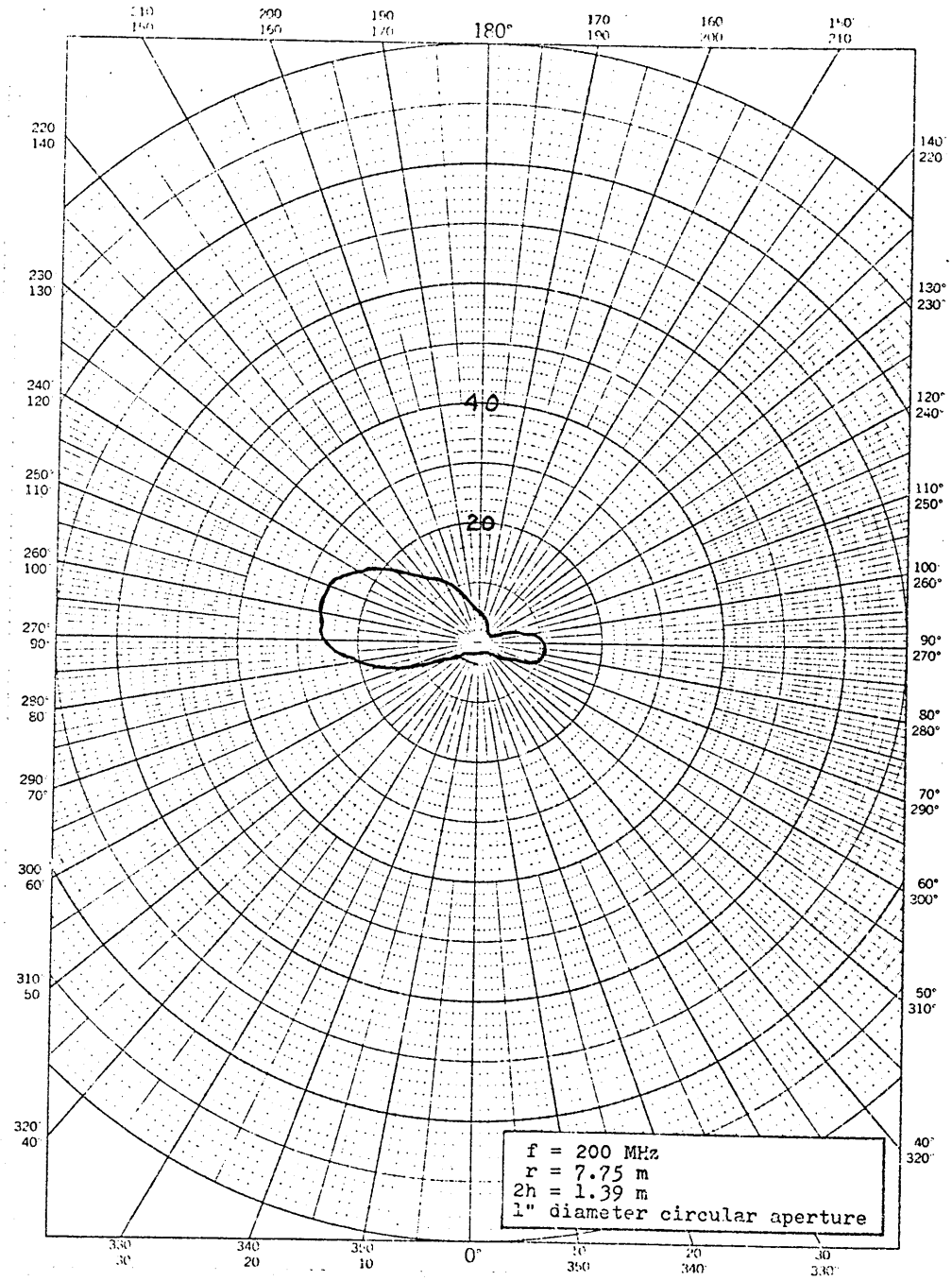

Figure 3.3. Power Delivered to Z_s versus θ for ℓ = .125 m at $\phi = 180^o$

2.1.4 Effect of Aperture Shape and Size on Field Patterns. According to the mathematical representation of the diffracting properties of the aperture as discussed in Appendix A, the relative magnitudes of the electric equivalent dipole and the magnetic equivalent dipole are in part determined by the eccentricity of the aperture. It was seen in the preceding section that the field patterns produced by the experimental model can be altered by changing the internal cavity tuning, and therefore also the relative contributions of the magnetic and electric equivalent dipoles. In this section, it is verified that changing the eccentricity of the aperture produces related results.

For this test, the patterns produced by the experimental model with a circular aperture and with an elliptical aperture were compared. The eccentricity of the circular aperture was zero and the eccentricity of the elliptical aperture was approximately 0.975. Thus, according to Collin [1960, p. 298], the contribution to the load current in Z_s from a magnetic equivalent dipole of unity magnitude is twice that of an electric equivalent dipole of unity magnitude for the circular aperture; while for the elliptical aperture, the unit magnetic equivalent dipole should contribute approximately 35 times as much to the load current in Z_s as the unit electric equivalent dipole. An operating frequency of 200 MHz was used, with $\phi = 180^{o}$.

The results of the tests with the two different apertures are shown in Figures 34 and 35. As expected, the patterns show a significant difference evidently due to the contribution from electric equivalent dipole. Also, it is seen by comparing Figure 35 with Figure 33 from the preceding section that the pattern produced by adjusting the interior length of the

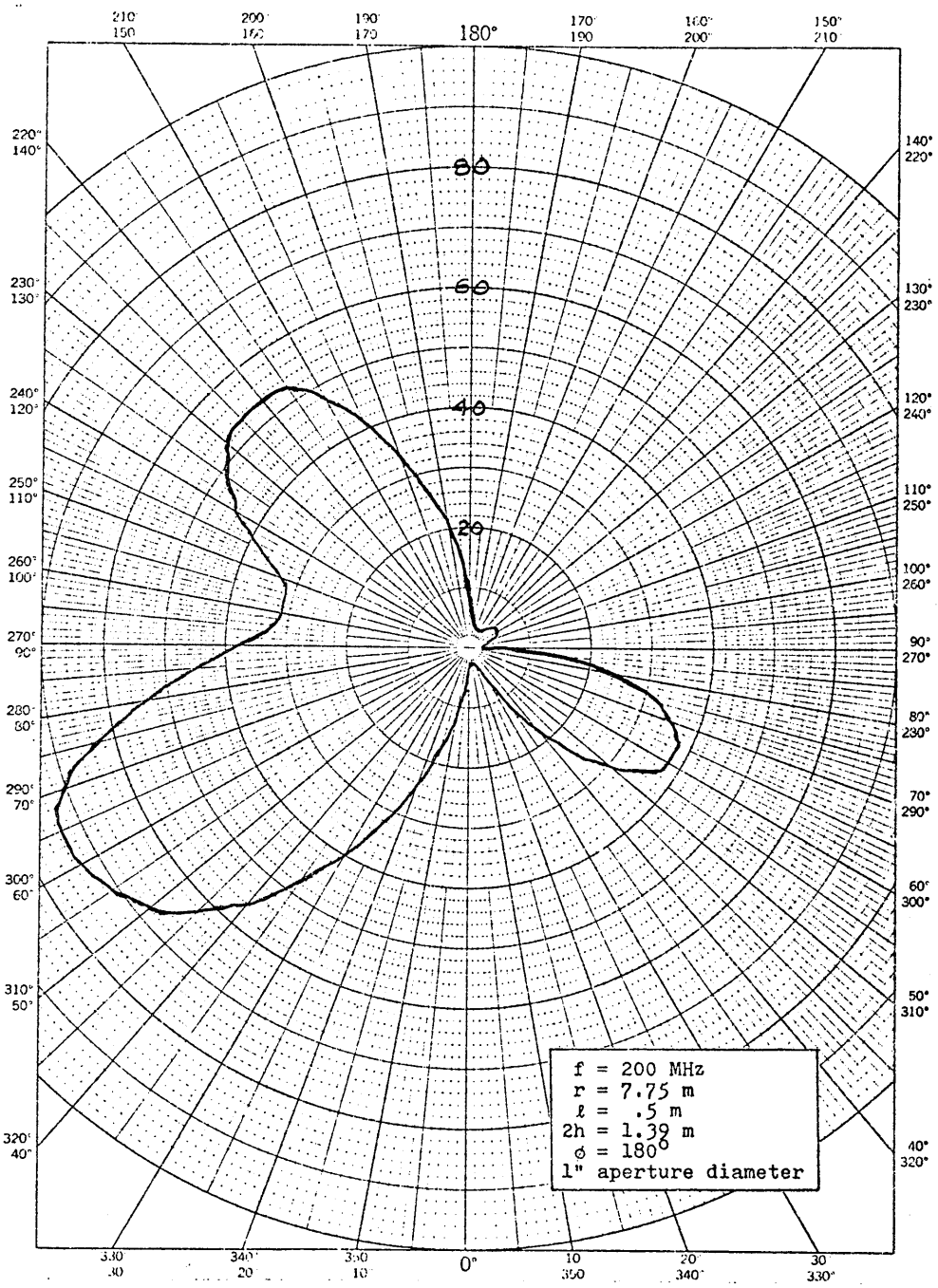

Figure 34. Power Delivered to Z_s versus θ
(Aperture Eccentricity = 0)

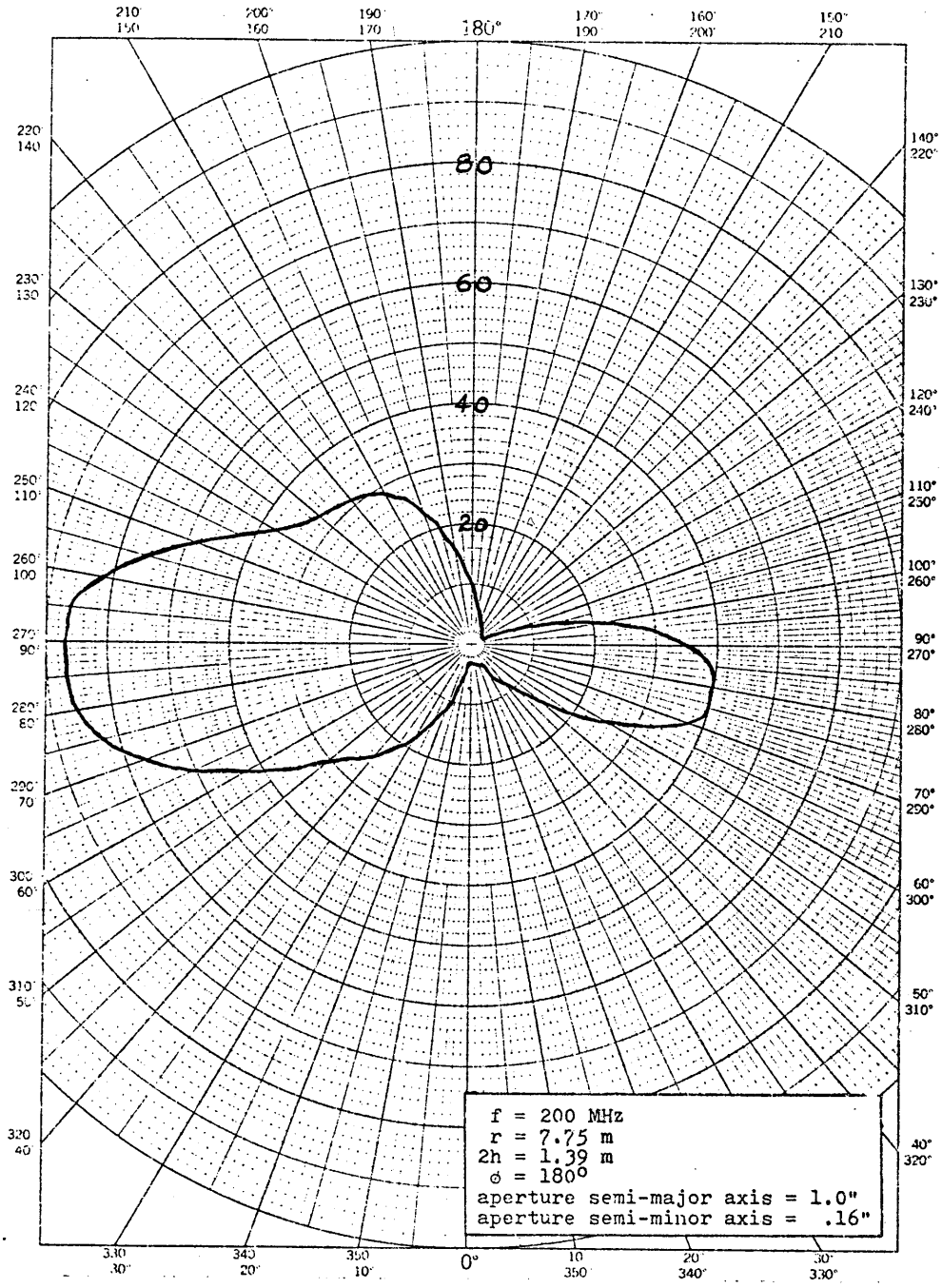

Figure 35. Power Delivered to Z_s versus θ
(Aperture Eccentricity ≅ .975)

experimental model (thereby maximizing the contribution from the magnetic equivalent dipole) has the same shape as the pattern produced by altering the shape of the aperture shape in the experimental model to achieve the same purpose. This further confirms the fact that the exterior surface charge-density and current distributions have different azimuthal angular dependences.

2.2 Measurement of Current Magnitude in the Load Impedance

In Appendix B, analytical solutions yielding the relative power delivered to the load impedance Z_s (proportional to the current in Z_s squared) as a function of the angle of incidence of the incoming plane wave are investigated. In this section a comparison is made of the measured magnitude of the current in Z_s, for a given angle of incidence, to the current magnitude predicted by the analytical solutions. The current in Z_s was calculated by taking the square root of the measured average power delivered to the crystal detector divided by the resistive R-F impedance of the crystal detector load. A fixed θ-angle of 45^o was used. Data were taken for ϕ-angles of 90^o and 180^o. At each ϕ-angle, three different apertures were used, and with each aperture four different external lengths were used. Thus, a total of 24 measurements were taken. The internal length ℓ was fixed at 0.5 m. The operating frequency was 300 MHz.

The results are shown in Figures 36 through 38, plotted as the magnitude of load current against external length in wavelengths. The calculated and measured data for these figures are found in Tables I through IV.

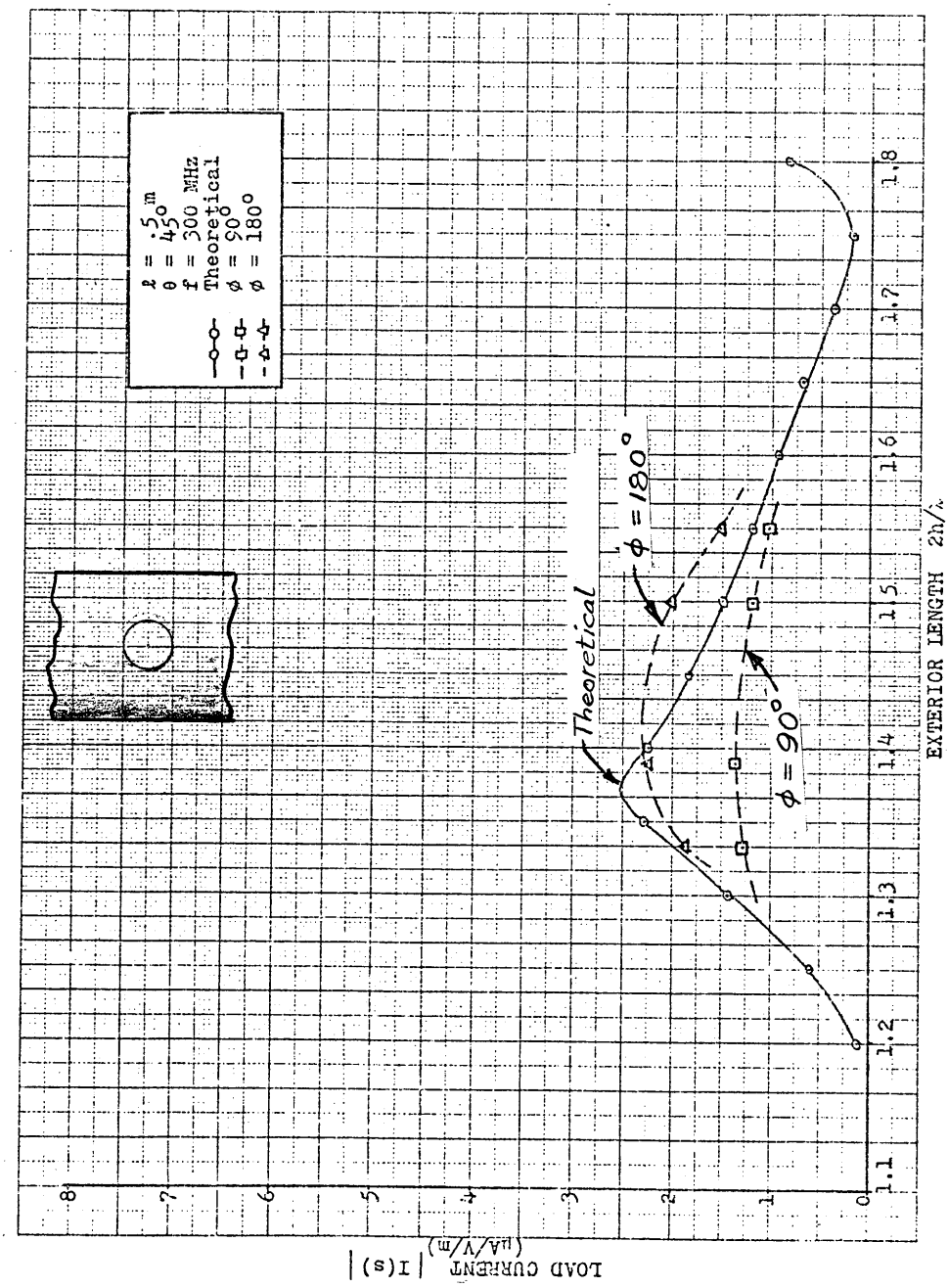

Figure 36. Current in Z_s versus Exterior Length for the Circular Aperture

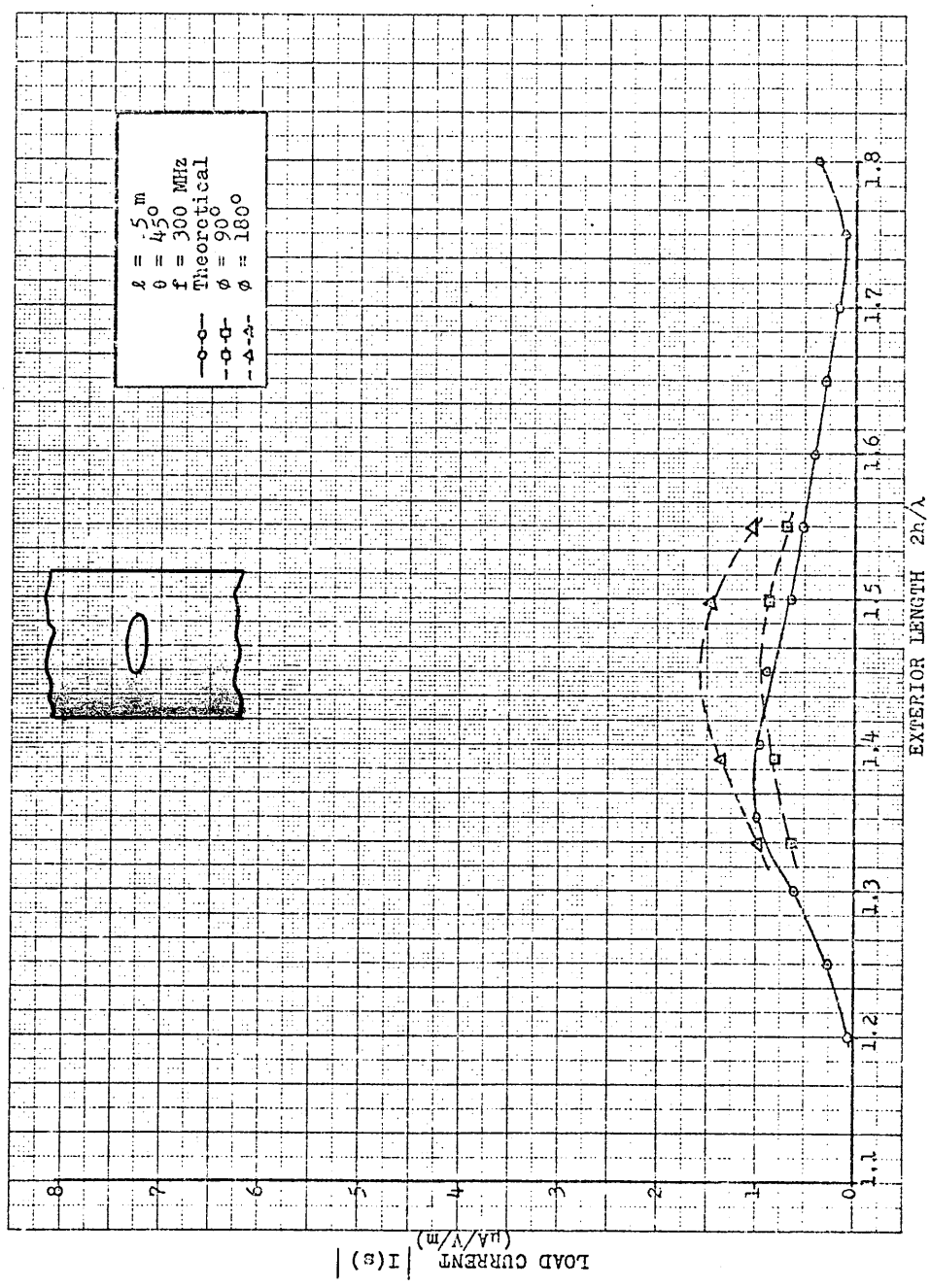

Figure 37. Current in Z_s versus Exterior Length for the Small Elliptical Aperture

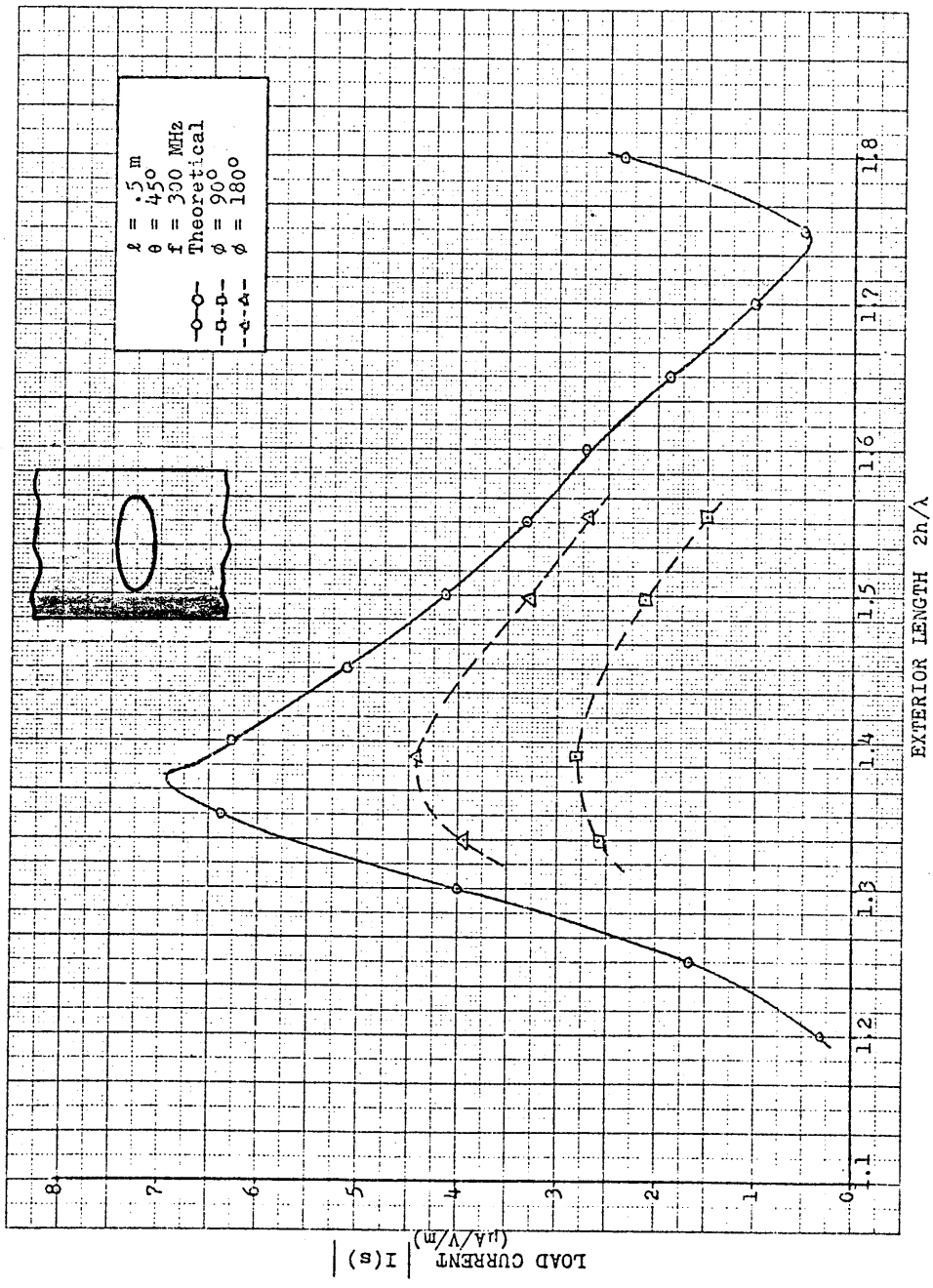

Figure 38 . Current in Z_s versus Exterior Length for the Large Elliptical Aperture

TABLE I

THEORETICAL LOAD CURRENT IN Z_s VERSUS EXTERIOR LENGTH

$2h/\lambda$	$\lvert I(s) \rvert$ (μA)		
	1" diameter circular aperture	$\frac{1}{4}$" x 1" elliptical aperture	$\frac{1}{3}$" x 2" elliptical aperture
1.20	.11	.05	.31
1.25	.60	.26	1.66
1.30	1.44	.62	4.00
1.35	2.29	.98	6.37
1.40	2.25	.96	6.27
1.45	1.89	.79	5.11
1.50	1.48	.64	4.13
1.55	1.20	.51	3.33
1.60	.94	.40	2.62
1.65	.68	.29	1.89
1.70	.37	.16	1.01
1.75	.18	.08	.51
1.80	.85	.37	2.37

$\theta = 45^\circ$
$f = 300$ MHz
$\ell = .5$ m

TABLE II

MEASURED LOAD CURRENT VERSUS EXTERIOR LENGTH
FOR THE ONE-INCH CIRCULAR APERTURE

Total exterior length $2h/\lambda$	Aperture offset distance z/λ	SWR meter reading (dB)		$\lvert I(s) \rvert$ ($\mu A/V/m$)	
		$\phi = 90^\circ$	$\phi = 180^\circ$	$\phi = 90^\circ$	$\phi = 180^\circ$
1.333	.055	-31.8	-28.6	1.29	1.88
1.390	.036	-31.4	-27.2	1.36	2.24
1.498	.047	-32.5	-28.0	1.20	2.02
1.555	.076	-33.8	-30.3	1.02	1.55

$r = 7.75$ m
$f = 300$ MHz
$\ell = .5$ m
$\theta = 45^\circ$
effective transmitted power = 45 dBm

TABLE III

MEASURED LOAD CURRENT VERSUS EXTERIOR LENGTH
FOR THE SMALL ELLIPTICAL APERTURE

Total exterior length $2h/\lambda$	Aperture offset distance z/λ	SWR meter reading (dB)		$\lvert I(s) \rvert$ ($\mu A/V/m$)	
		$\phi = 90^\circ$	$\phi = 180^\circ$	$\phi = 90^\circ$	$\phi = 180^\circ$
1.333	.055	-38.0	-34.0	.64	.98
1.390	.036	-35.8	-31.4	.82	1.36
1.498	.047	-35.4	-30.9	.85	1.44
1.555	.076	-37.5	-33.9	.67	1.02

$r = 7.75$ m
$f = 300$ MHz
$\ell = .5$ m
$\theta = 45^\circ$
effective transmitted power = 45 dBm

TABLE IV

MEASURED LOAD CURRENT VERSUS EXTERIOR LENGTH
FOR THE LARGE ELLIPTICAL APERTURE

Total exterior length $2h/\lambda$	Aperture offset distance z/λ	SWR meter reading (dB)		$\lvert I(s) \rvert$ ($\mu A/V/m$)	
		$\phi = 90^\circ$	$\phi = 180^\circ$	$\phi = 90^\circ$	$\phi = 180^\circ$
1.333	.055	-26.0	-22.3	2.57	3.95
1.390	.036	-25.2	-21.4	2.82	4.41
1.498	.047	-27.5	-23.8	2.13	3.28
1.555	.076	-31.0	-25.5	1.50	2.70

$r = 7.75$ m
$f = 300$ MHz
$\ell = .5$ m
$\theta = 45^\circ$
effective transmitted power = 45 dBm

The results show excellent agreement for $\phi = 90^{o}$, and agreement within an order of magnitude for $\phi = 180^{o}$. The results appear reasonable since the rotational current previously noted in Section 4.2 should cause the smallest deviation from thin-antenna theory for $\phi = 90^{o}$. Also, although a small shift in the location of the maxima is evident between the theoretical curves and the measured curves, fairly close agreement with respect to the shape of the curves was obtained. Thus, it would appear that the Harrison and Taylor solution incorporating the Shen current formulation does provide a fairly reliable solution for this problem.

The large elliptical aperture produced lower magnitudes of load current relative to the theoretical values for the various test cases than did the other two apertures. The large elliptical aperture had a semi-major dimension of one inch as compared to the one-half inch semi-major dimension of the other two apertures. Possibly the greater wall thickness near the ends of the major axis of the elliptical aperture, or the greater curvature of the surface bounded by the larger aperture, resulted in the lower magnitudes of current produced in the load impedance Z_s than predicted by the theory, when the large elliptical aperture was used.

2.3 Conclusions

Probably the most important conclusion reached was that for a cylinder radius of approximately 0.05 of a wavelength, with apertures of sizes described in here, the thin-wire antenna theory does not appear to be valid. Evidently a significant "shadowing effect" occurs, which results in the exterior current on the directly-illuminated portion of the experimental model being greater than the exterior current on that portion of the experimental model not directly illuminated.

The Harrison and Taylor solution with the Shen formulation being used to express the exterior current distribution provides reasonably accurate solutions for the problem provided the azimuthal angle of incidence ϕ is not near 0^{o} or 180^{o}. Numerical difficulties may evidently arise using the Shen formulation at near grazing incidence, particularly for θ near 180^{o}. Reasonable agreement between the theoretical and experimental results for both pattern measurements and magnitude measurements was obtained for ϕ-angles of both 90^{o} and 180^{o}. The experimental results would appear to support Collin's expressions for the polarizability functions, assuming the Shen current formulation is valid for $\theta = 45^{o}$.

Finally, it is worth noting that the most difficult problem encountered in the development of the experimental model was that of transmitting the information signal from the internally mounted crystal detector to the test instrumentation. Before incorporating the fiber-optic data link, a coaxial cable was used for the purpose of carrying the output signal of the experimental model to the SWR meter used to measure the voltage output. In spite of using a coaxial cable that was thin compared to the cylinder and a quarter-wave R-F choke between the cable and the experimental model, the field scattered from the cable produced such a great alteration of the incident fields and exterior current distributions on the model that it was impossible to obtain meaningful data. Variations in the output signal were as easily produced by moving the coaxial cable as by moving the model itself, and the effects of the coaxial cable on the experimental model could not be separated from the experimental results. The use of a non-metallic data link should be considered mandatory for any similar future experiments.

PART III

ELECTROMAGNETIC PENETRATION FROM THE END OF A SHIELDED COAXIAL CYLINDER

Chapter I

Introduction and Theory

The second physical model we have investigated involves the penetration of electromagnetic energy past a recessed end-cap assembly at one end of a cylindrical enclosure into an otherwise identical coaxial structure, as described in Part II. A sketch of the basic configuration involving the recessed endcap is shown in Figure 39. It consists of a metallic, circular short-circuiting plate recessed at a distance d from the end of a cylindrical enclosure, and a protruding metallic rod of length ℓ. The size of the plate is designed to be somewhat smaller than the inner cross section of the enclosure, so that a gap (in the form of an annular aperture with $\frac{1}{4}$" width or less) exists, which then provides the only port-of-entry for electromagnetic leakage into the system inside the enclosure. The conducting rod, on the other hand, is included in the design in order to simulate, in some idealized sense, any electric wiring that might exist in front of the short-circuiting plate to produce a coaxial wave-guiding structure there. A detailed description of the construction of the recessed end-cap assembly is given later.

1.1 Theoretical Description of the Model

In the case of electromagnetic penetration through small holes on the surface of a conducting enclosure, it was mentioned that the external

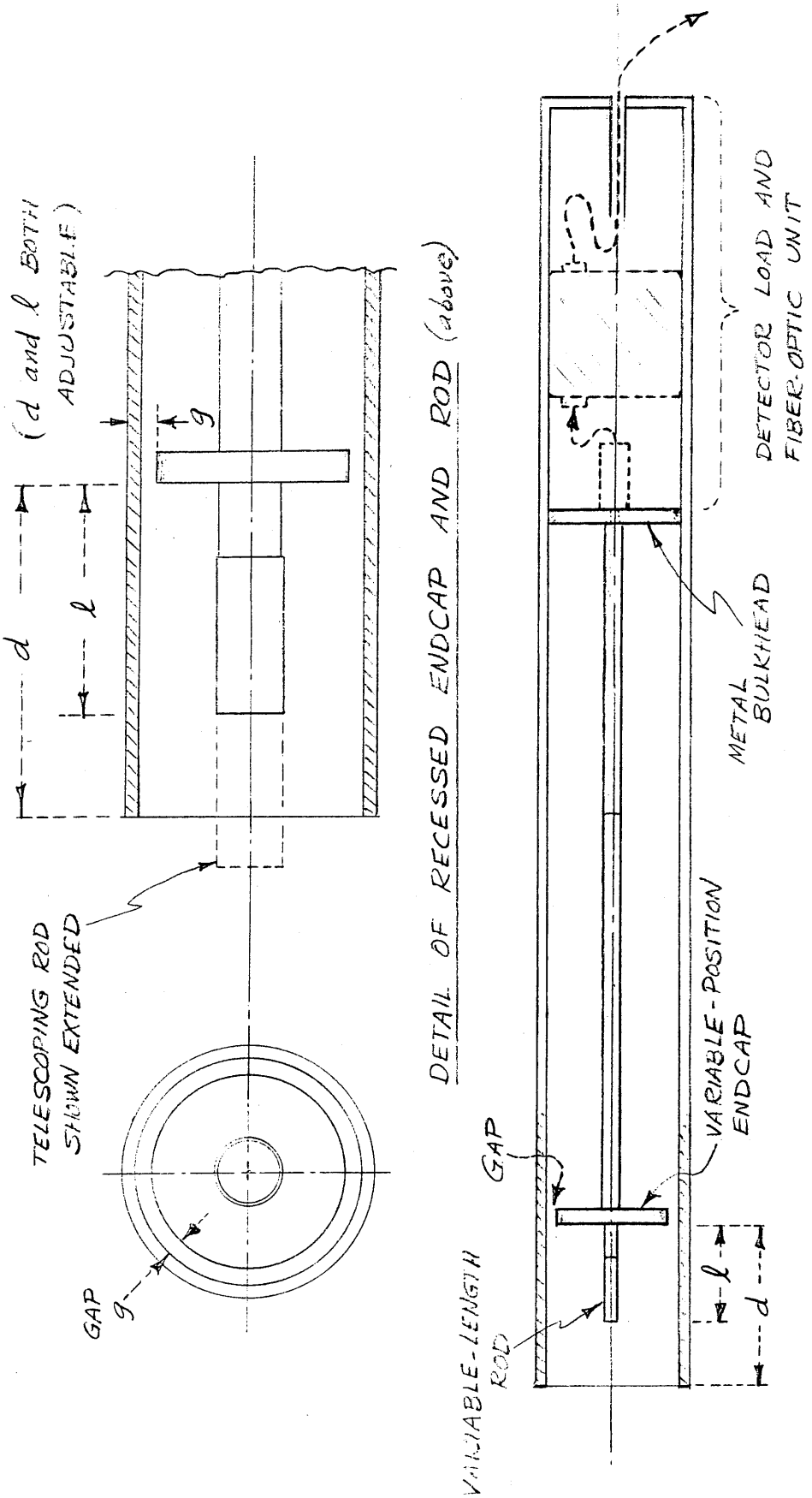

Figure 39. Second Experimental Model, with Recessed Annular Gap and and Variable Length Rod.

surface of the enclosure can be viewed as a receiving cylindrical antenna, while the inside surface of the enclosure and the center conductor form a coaxial structure which can be analyzed according to conventional transmission-line theory. In order to take care of the coupling between the external "antenna" and internal "transmission-line" provided by the small aperture, we need only to replace the aperture by the equivalent electric and magnetic dipoles existing on both sides of the enclosure. The magnitude and direction of those dipoles are then determined by the unperturbed normal electric and tangential magnetic fields (that exist there without the aperture), or alternatively by the charge and current distributions existing at the location of the aperture. However, such an approach can not be applied easily to the present situation, not only because the aperture is now recessed into the cylinder, but also because current near the end usually can not be computed with any acceptable degree of accuracy from any conventional antenna theory. As a consequence, very little is available in the literature concerning theoretical evaluation of the penetrating electromagnetic energy into the enclosed system, at least in the framework of linear antenna theory.

A related problem which has been treated quite extensively in the past concerns the electromagnetic radiation from an open, circular waveguide. Weinstein [1969]; Levine and Schwinger [1948], among others, have used the so-called Wiener-Hopf technique to obtain an analytical expression for the radiation pattern of a TE- or TM- mode in an open circular waveguide. The same technique has also been applied successfully to the radiation of a cylindrical antenna [Chen and Keller, 1962; Shen, et al., 1968; Mittra and Lee, 1971] ; a dipole-excited, semi-infinite, cylindrical antenna [Chang,1973];

surface of the enclosure can be viewed as a receiving cylindrical antenna, while the inside surface of the enclosure and the center conductor form a coaxial structure which can be analyzed according to conventional transmission-line theory. In order to take care of the coupling between the external "antenna" and internal "transmission-line" provided by the small aperture, we need only to replace the aperture by the equivalent electric and magnetic dipoles existing on both sides of the enclosure. The magnitude and direction of those dipoles are then determined by the unperturbed normal electric and tangential magnetic fields (that exist there without the aperture), or alternatively by the charge and current distributions existing at the location of the aperture. However, such an approach can not be applied easily to the present situation, not only because the aperture is now recessed into the cylinder, but also because current near the end usually can not be computed with any acceptable degree of accuracy from any conventional antenna theory. As a consequence, very little is available in the literature concerning theoretical evaluation of the penetrating electromagnetic energy into the enclosed system, at least in the framework of linear antenna theory.

A related problem which has been treated quite extensively in the past concerns the electromagnetic radiation from an open, circular waveguide. Weinstein [1969], Levine and Schwinger [1948], among others, have used the so-called Wiener-Hopf technique to obtain an analytical expression for the radiation pattern of a TE- or TM- mode in an open circular waveguide. The same technique has also been applied successfully to the radiation of a cylindrical antenna [Chen and Keller, 1962; Shen, et al., 1968; Mittra and Lee, 1971] ; a dipole-excited, semi-infinite, cylindrical antenna [Chang,1973];

to a receiving dipole antenna [Shen]; and to the problem of the diffraction by a cylinder [Williams, 1956]. However, the electromagnetic field inside the cylinder is determined accurately usually only when the radius of the cylinder is large enough to support the propagation of a waveguide mode.

Actually, Shen's work on the receiving antenna can, in principle, be extended to obtain information regarding the electromagnetic penetration from the end of a cylinder, once a correct expression is obtained for the case of a near-grazing incident plane wave. Such an extension is currently being pursued [Chang and Lee, private communication] and the result is summarized in Appendix C. In their method, the field penetrating into the interior of the cylinder is obtained from a similar multi-reflection concept. When a plane wave is incident upon one end of the cylinder, the electromagnetic field partially penetrates into the hollow cylinder in the form of an evanescent field for a waveguide below cutoff, and is partially guided along the external surface in the form of an unperturbed plane-wave, superimposed upon a wave emanating from the edge of the cylinder. These two component waves then propagate to the other end on the outer surface of the enclosure as if there exists a generator located at this end. Upon arriving at the other end, they both reflect. This multi-reflection process continues indefinitely between the two ends of the cylinder, whereupon each time it arrives at the end with the recessed aperture, a portion of the field is leaked into that region in a form of an evanescent field. Thus, the total field that eventually gets inside can be looked upon as a combination effect of the direct illumination of a long, open, cylindrical waveguide and the cumulative penetration due to the standing-wave established by the current on a cylindrical receiving antenna of finite length.

1.2 Modified Model for Electromagnetic Penetration via One End

Figure 40 shows how the physical model of Figure 3 was modified to obtain electromagnetic penetration into the internal coaxial structure via a recessed endcap surrounded by a peripheral air gap. A comparison of Figure 3 with Figure 40 shows that the latter modification was obtained by making the following changes in Figure 3:

1. The section containing the aperture in the cylinder wall in Figure 3 was replaced with a screw-in section of identical 4" O.D. aluminum tubing of the same length, but having no aperture.

2. The sliding shorting-plate structure ("A" and "B"), used to simulate the impedance $Z_o = 0$ in Figure 1, was removed and not used.

3. The center conductor, a one-piece 0.625" O.D. tube in Figure 3, was replaced by the telescoping center conductor of Figure 40, terminated in a movable conducting end cap of reduced size, leaving an annular ring-aperture of width g around the end cap. The telescoping center conductor enables the adjustment of the distance d from the end cap to the cylinder end. Foam polystyrene ($\varepsilon_r = 1.02$) was used to center the endcap, to provide the uniform gap-width g. Unless otherwise specified, $g = 0.25"$.

4. An optional, short conducting rod of variable (telescoping) length ℓ was screwed into the exterior side of the end cap, to simulate the possible "wiring" that might exist in front of the endcap, thereby producing an additional wave coupling due to the TEM mode on that coaxial wave-guiding structure. Unscrewing this short, telescoping rod from the end cap provides

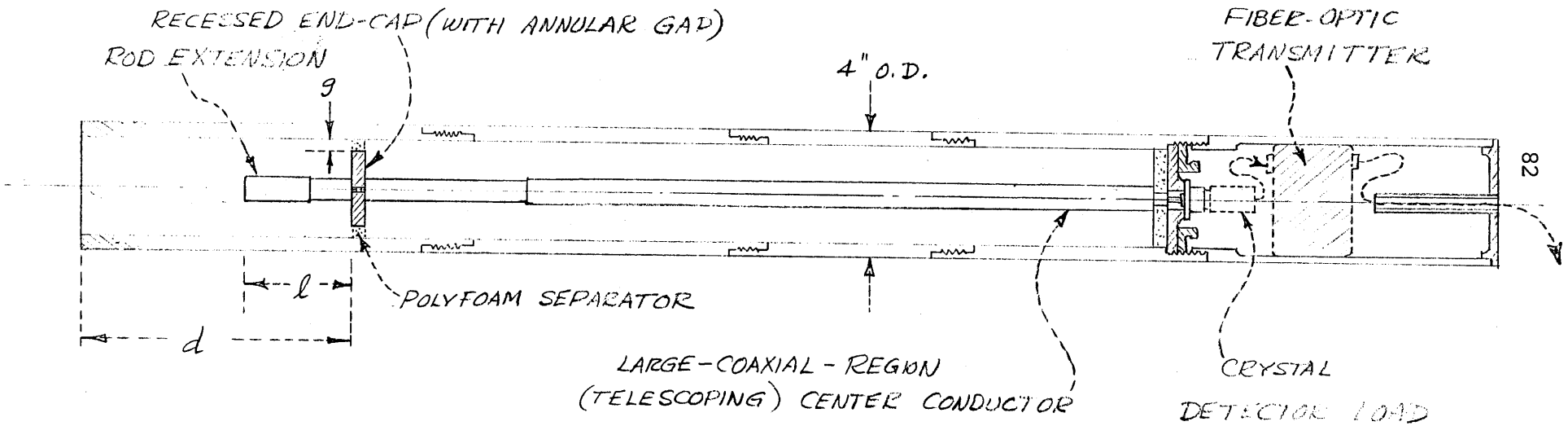

Figure 40. Second Experimental Model Details

optional wave coupling to the annular aperture by way of the resulting short section of hollow circular waveguide.

With these modifications, the coordinate system adopted for the second model is assumed the same as shown in Figure 2, the movable, conducting endcap being located along the cylinder z-axis at the $\theta = 0$ position shown. The axial symmetry that exists for this model so modified dictates that no ϕ-variation of its field pattern will exist, so only one pattern in any ϕ-plane needs to be taken for any particular choice of the end-cap location d and rod-length ℓ.

1.3 Measurement of Model Response and Calibration of the Crystal Detector and Associated Circuitry

In obtaining the field patterns to be described for the end-aperture model, only relative level comparisons, at major-lobe maxima, were made. If one is to make an absolute comparison of the experimental pattern data with a suitable analytical theory for this model, then values of the absolute response of the model, preferably at the major-lobe maxima, need to be measured. This response may again be conveniently defined as described in Section 2.2 of Part II (and plotted in Figures 36 through 38) for the first model; there a "response" was defined as the ratio of the r-f load current amplitude $|I_s|$ induced in the crystal detector input impedance Z_s (at $z = s$ in Figure 2), divided by the incident electric-field amplitude $|E^{inc}|$ associated with the arriving uniform plane wave (arriving at an arbitrary angle of incidence θ as in Figure 2). This response $|I_s|/|E^{inc}|$ evidently has the units of ampere per V/m. Equally useful and equivalent definitions of model response are expressible in terms of the detector-load

r-f voltage (instead of load current), or even in terms of the average r-f power absorbed by the detector load. Hence, $|V_s|/|E^{inc}|$ or $P_{av,s}/\mathcal{P}_{av}^{inc} = P_{av,s}/|E^{inc}|^2/2\eta_o$ are useful definitions of model response, in which V_s, I_s are related by the detector input r-f complex impedance Z_s, $\mathcal{P}_{av}^{inc} = |E^{inc}|^2/2\eta_o$ is the incident Poynting average power density, and the detector input power is expressed in terms of the complex load current and voltage by $P_{av,s} = \frac{1}{2}\,\mathrm{Re}(V_s I_s^*) = \frac{1}{2}\,|V_s||I_s|\cos\theta$, if θ is the load impedance angle. In the event of a matched or nearly matched detector load (Z_s roughly equal to the characteristic impedance of the interior coaxial structure of the model), then there would be no particular advantage of any of these three definitions of response over the other. In the event of a highly mismatched load impedance, however, (with Z_s highly reactive, or perhaps close to a short-circuit or an open-circuit condition), then there would possibly be some advantage to using the average-power definition. Of course, for a perfectly shielded model having no coupling aperture, each of these response ratios would reduce to zero.

In what follows, let us adopt the definition of "model response" in terms of the average power $P_{av,s}$ absorbed by the detector load; i.e., define: Response = $P_{av,s}/\mathcal{P}_{av}^{inc}$ watt per W/m^2. To evaluate this response experimentally, the following measurements are seen to be required:

1. The electric-field amplitude $|E^{inc}|$ of the essentially uniform plane wave impinging on the model on the antenna test range (at the desired incidence angle θ) must be found. With the model located in the far-zone region of the transmitting antenna used to illuminate the model, with a known amount of r-f (average input) power $P_{av,t}$ driving the antenna, and presuming the antenna gain g to be known, the value of E^{inc} at the model

site can be determined as described at the end of Section 1.6 in Chapter 1 of Part II, yielding the peak value, for CW conditions:

$$E^{inc} = \left[\frac{2\eta_o g}{4\pi r^2} P_{av,t} \right]^{\frac{1}{2}} \quad [V/m]$$

An alternative procedure is to measure the electric field E^{inc} directly at the model location by use of a field-intensity meter. A recent innovation of this type is the non-directional probe and direct-reading power-density meter system invented by R. Bowman at the National Bureau of Standards in Boulder, Colorado. This instrument was employed (courtesy of Mr. Bowman) to check the incident electric field intensity provided by the E^{inc} expression above, and was found to give agreement within five to ten percent at 300 MHz, considered to be quite adequate for present purposes.

2. The r-f average power $P_{av,s}$ absorbed by the detector load (at $z = s$ in the model) must also be measured. Because of the very low power levels usually involved (of the order of microwatts to picowatts), a calibration of the crystal detector load and its associated circuity (feeding the Develco fiber optic data link and the Hewlett-Packard 415B tuned-amplifier "SWR meter" output, in the version used), becomes necessary. This has already been described in Section 1.4.2 of Part II, relative to Figure 7, but is discussed here a bit further in relation to the sinusoidal amplitude-modulated r-f carrier used.

It is to be noted that, without any (1000 Hz) modulation of the r-f carrier, no signal output would be obtained from the HP415B tuned amplifier. The 300 MHz carrier used in these tests was therefore modulated using a 1000 Hz sinusoidal modulation signal (required by the tuned amplifier of the

HP415B "SWR meter" output indicator), employing a constant modulation index, m. In conjunction with these response tests made on the second (end-penetration) model, a different crystal detector load and tuned amplifier (SWR meter) were used than those employed with the first model; consequently, a new calibration curve for the output indicator system (detector load plus Develco fiber optic unit plus HP415B meter) had to be obtained, making inapplicable the one given in Figure 8.

The calibration system shown in Figure 7 was once more employed. The r-f generator (Maxson) was set by an oscilloscope for 65% modulation (m = 0.65) using a 1000 Hz sinusoidal modulation frequency, at a monitored constant average power output (24.1 watts as in the model tests). Upon varying the average power input into the matched crystal detector load (varied by use of the GR874-VR variable coaxial attenuator, and read by means of the HP431B power bridge), the corresponding relative output voltage (in dB) obtained from the meter of the HP415B tuned amplifier was obtained, to yield the calibration curve of Figure 41. The crystal input r-f average power, measured by the HP431B power meter, was varied from -10dBm (0.1 mW) to - 50 dBm (0.01 μW) for this particular calibration. Thus, if some particular output reading, say -30dB, were observed on the HP415 tuned amplifier while testing the model response under plane-wave illumination conditions on the test range, the calibration curve would signify the detector input average power of -36.9 dBm, or 0.2042 μW, assuming the same conditions of modulation index (m = 0.65) and sinusoidal modulation frequency (1000 Hz) as required by this calibration curve.

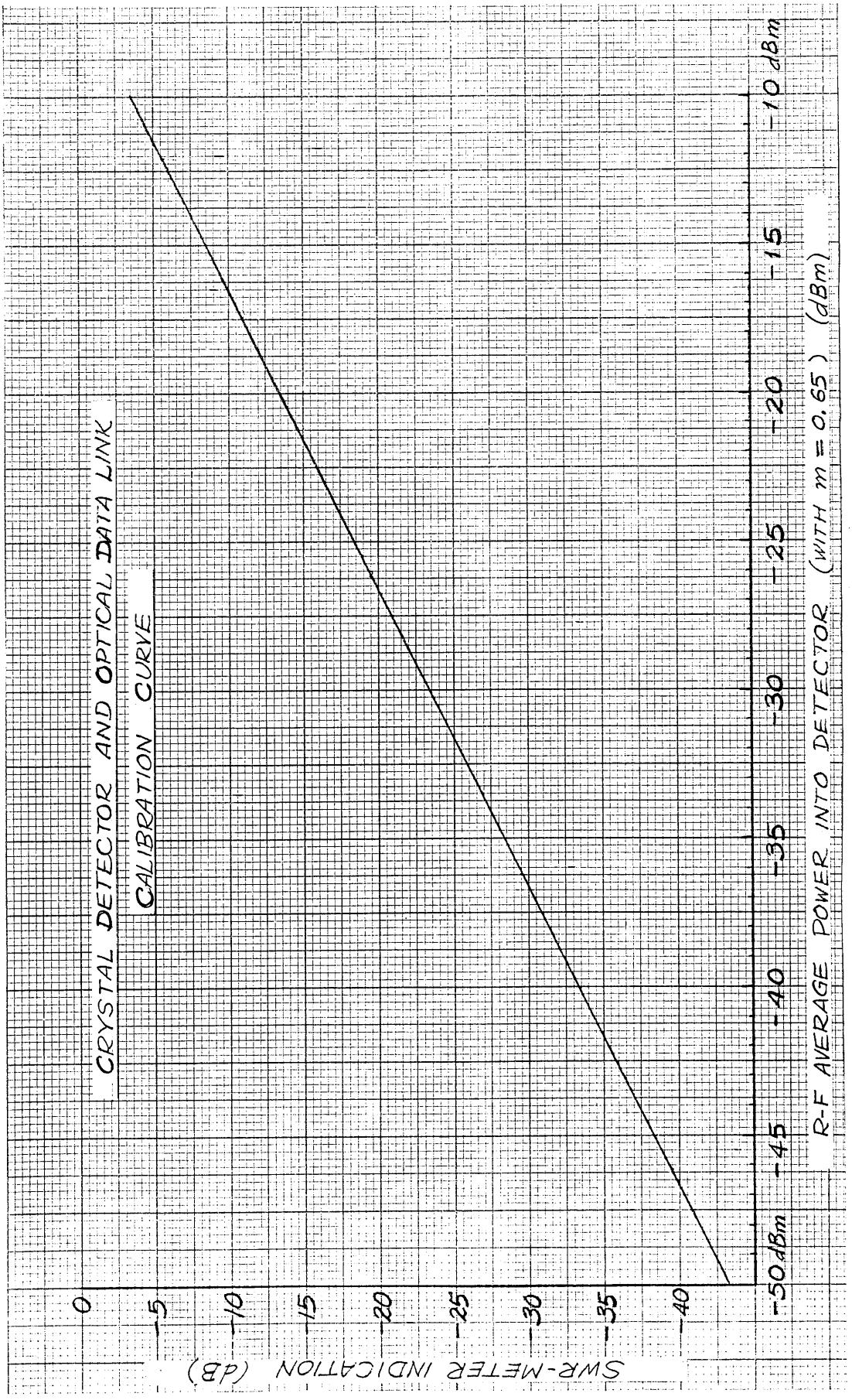

Figure 41. Calibration Curve for the HP423B Coaxial Detector Mount and Optical Data Link (Feeding HP415B SWR meter).

Chapter 2

Experimental Results

2.1 Experimental Pattern Results for the Modified End-Aperture Model

While the detailed theoretical pattern analysis of the detector response to a plane wave incident on the modified model in Figure 40 has yet to be completed, considerable insight is to be gained from experimental tests of the model concerning what plausible directions the theoretical effort might take. Thus, a series of experimental patterns of detected power versus plane-wave arrival-angle θ were obtained for the modified model on the same test range described in Section 1.6 of Part I.

Several representative power (E^2) patterns obtained from this model are shown in Figures 42 through 47, for typical adjustments of the endcap position d and rod-length ℓ as denoted in Figure 39. The dB level indicated on each of these patterns refers to the relative amount of received power occurring at the major-lobe maximum. In Figure 42, for example, with the end cap position d = 0 (flush with the cylinder end in Figure 39) and the center rod protruding from the end cap by $\ell = 5.4$ cm, the six-leaved pattern revealed a major-lobe maximum at the relative level of 10.7 dB. This may be compared with the 7.1 dB level obtained in Figure 43, obtained with d = o (the same, flush endcap position) but for $\ell = 0$ (the center rod is absent), showing a diminution of the major-lobe maximum power level by 3.6 dB. Similarly, as seen in Fig. 44, moving the end cap in to the recessed position d = 3 cm and with the rod length again brought out to $\ell = 5.4$ cm, the main-lobe maximum was reduced by another 4.1 dB to the indicated 3 dB relative level, a consequence mainly of the reduction of the length of rod protruding from the cylinder end. In Fig. 44, the additional attenuation obtained upon removing the

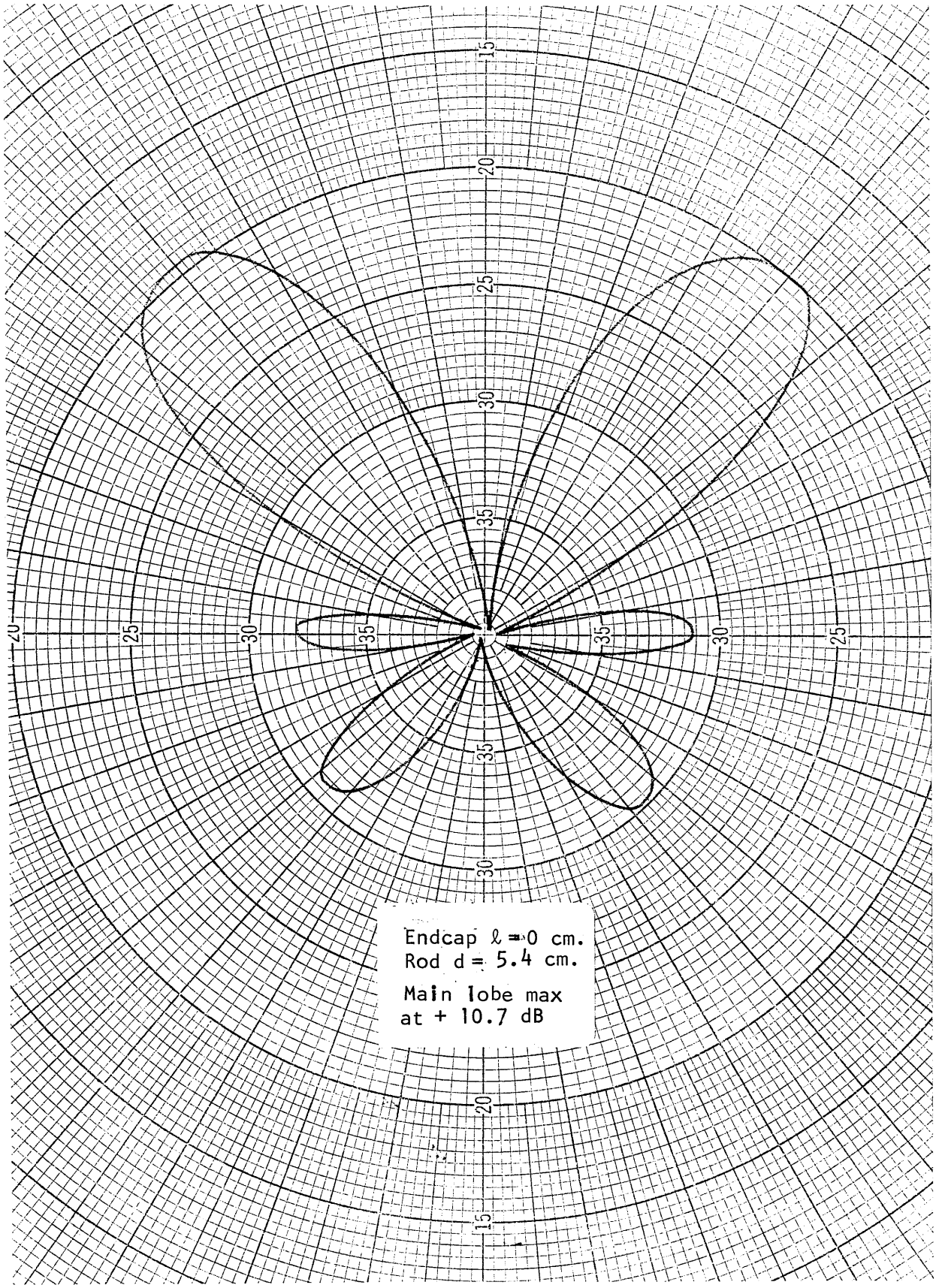

Figure 42. θ-Pattern for Modified End-Aperture Model.

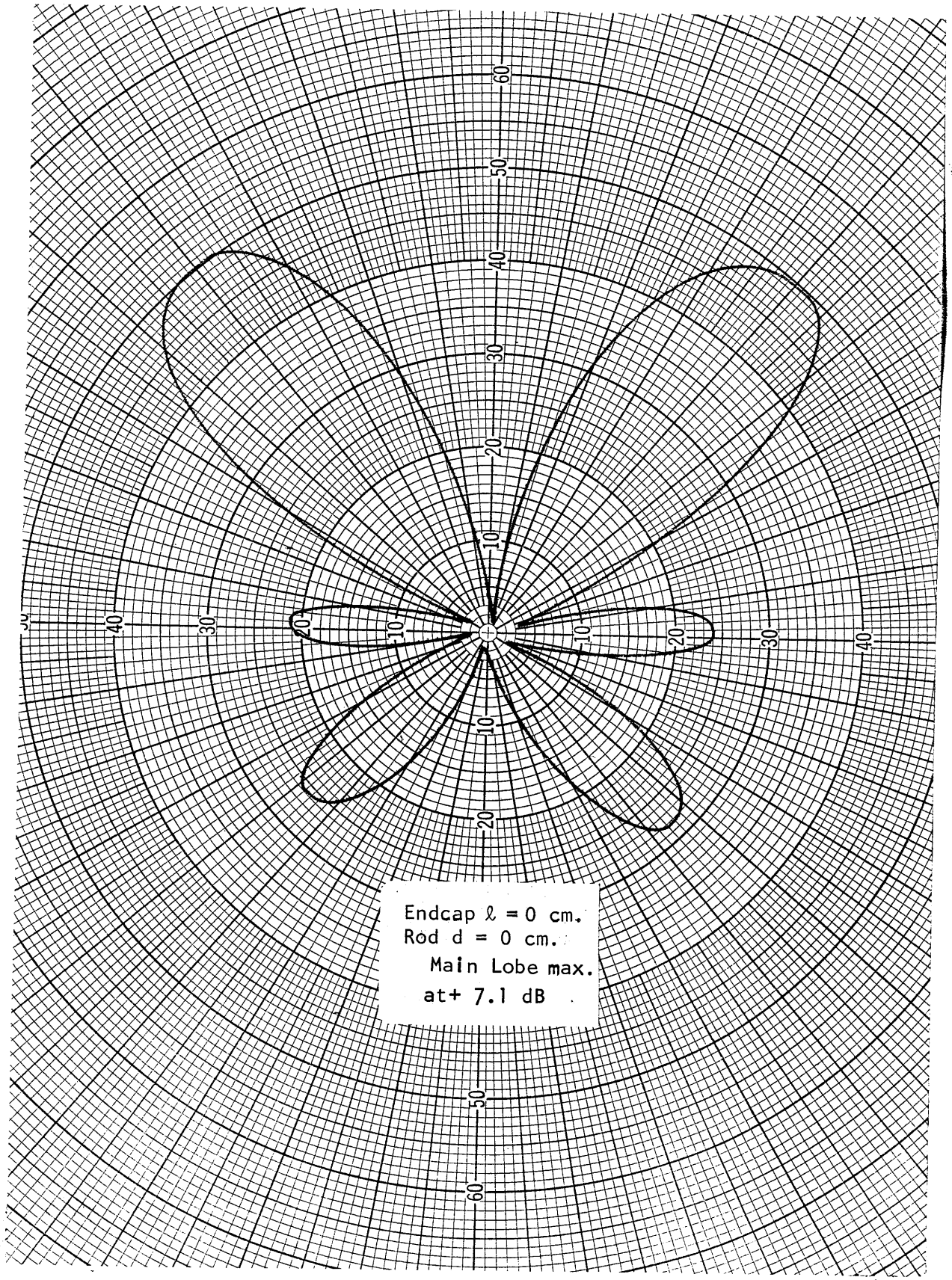

Figure 43. θ-Pattern for Modified End-Aperture Model.

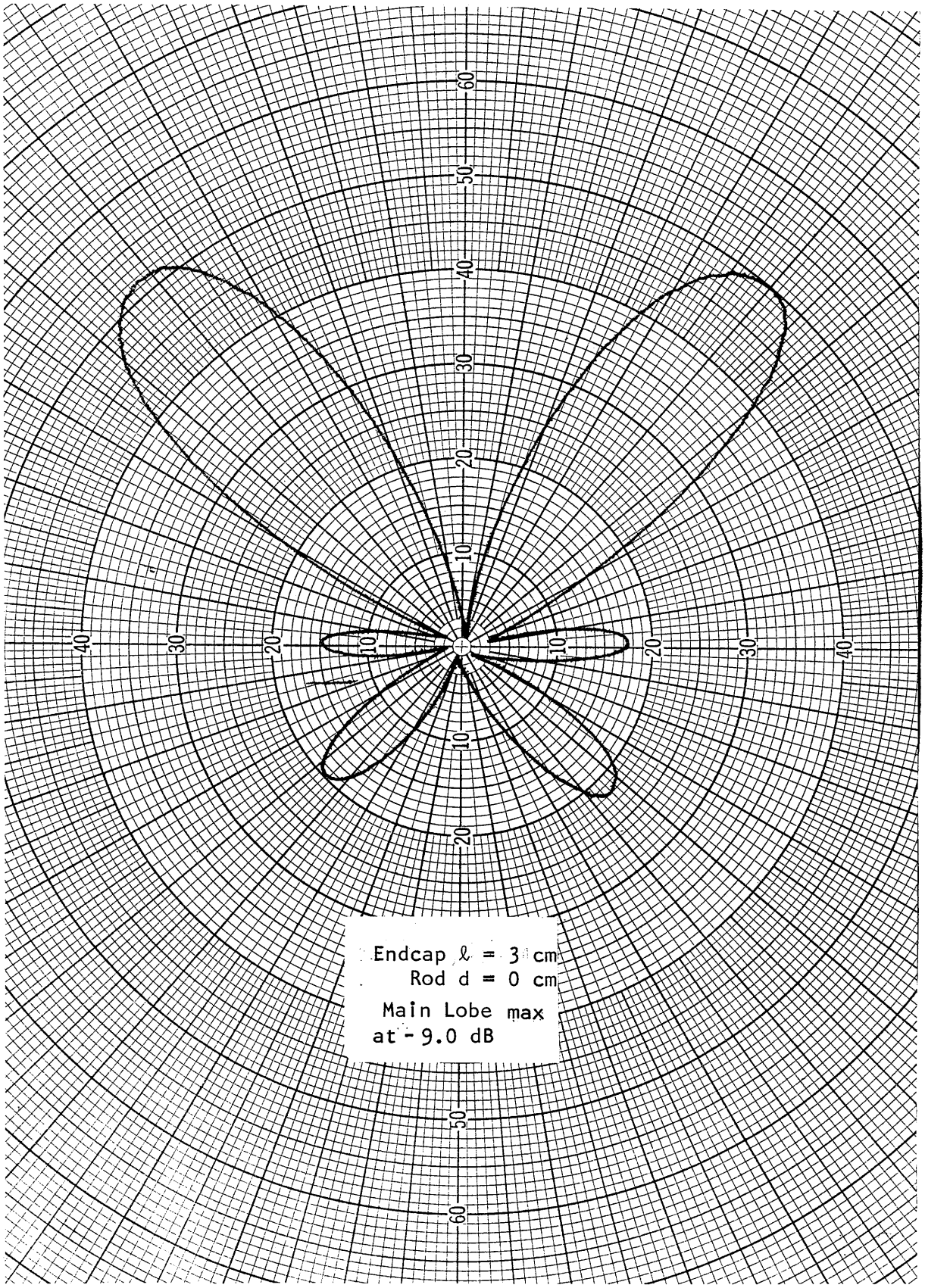

Figure 44. θ-Pattern for Modified End-Aperture Model

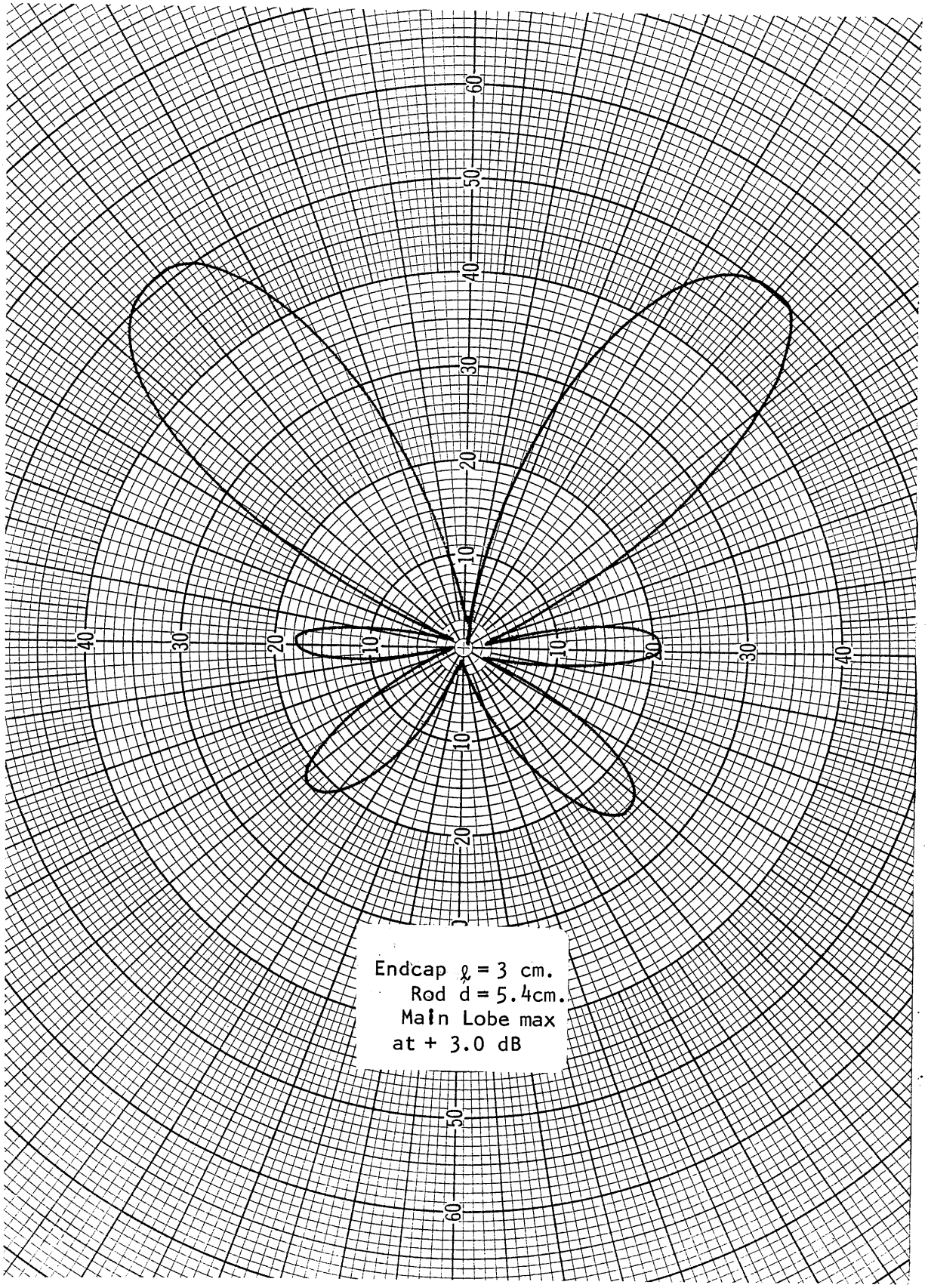

Figure 45. θ-Pattern for Modified End-Aperture Model

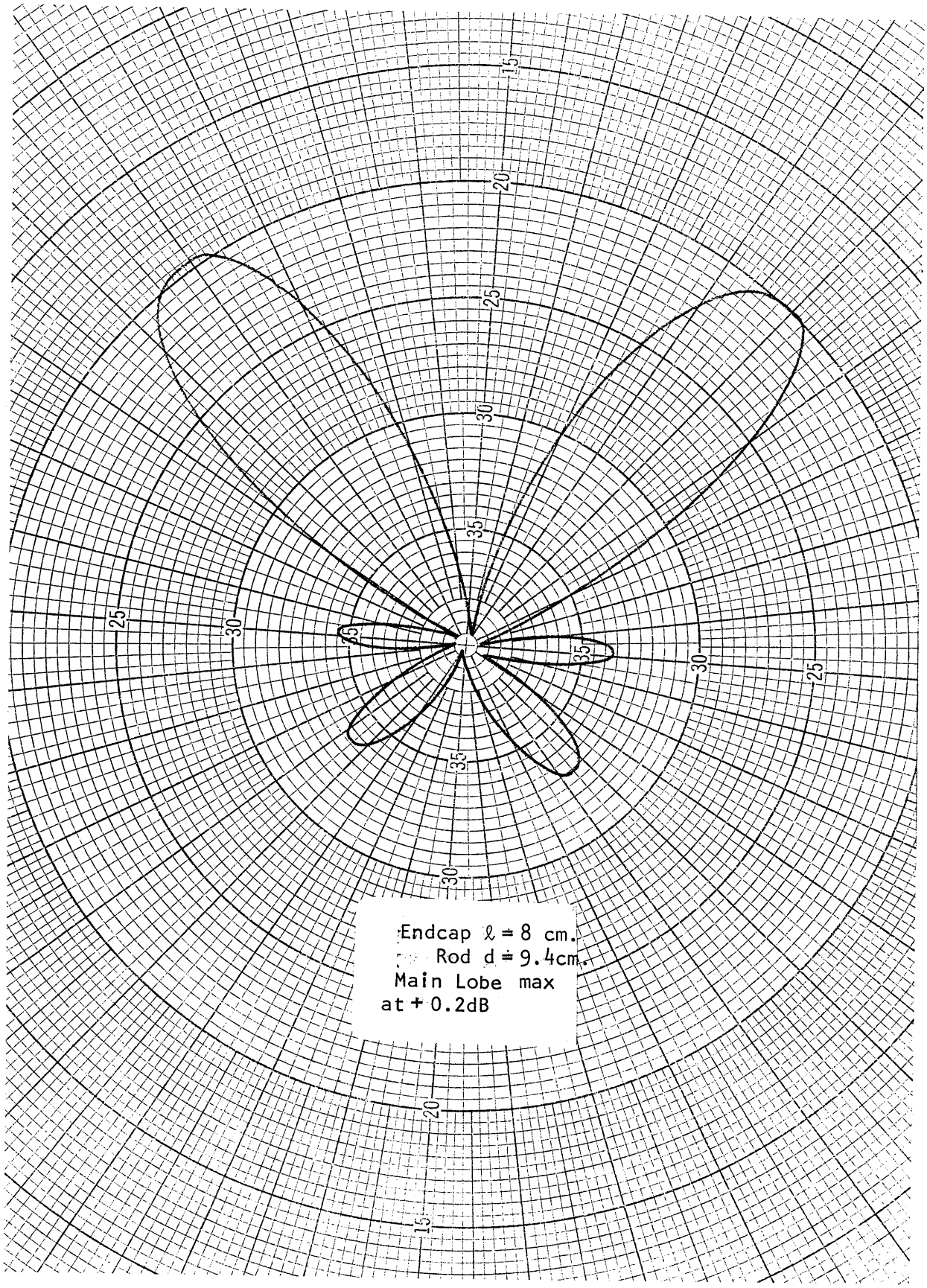

Figure 46. θ-Pattern for Modified End-Aperture Model

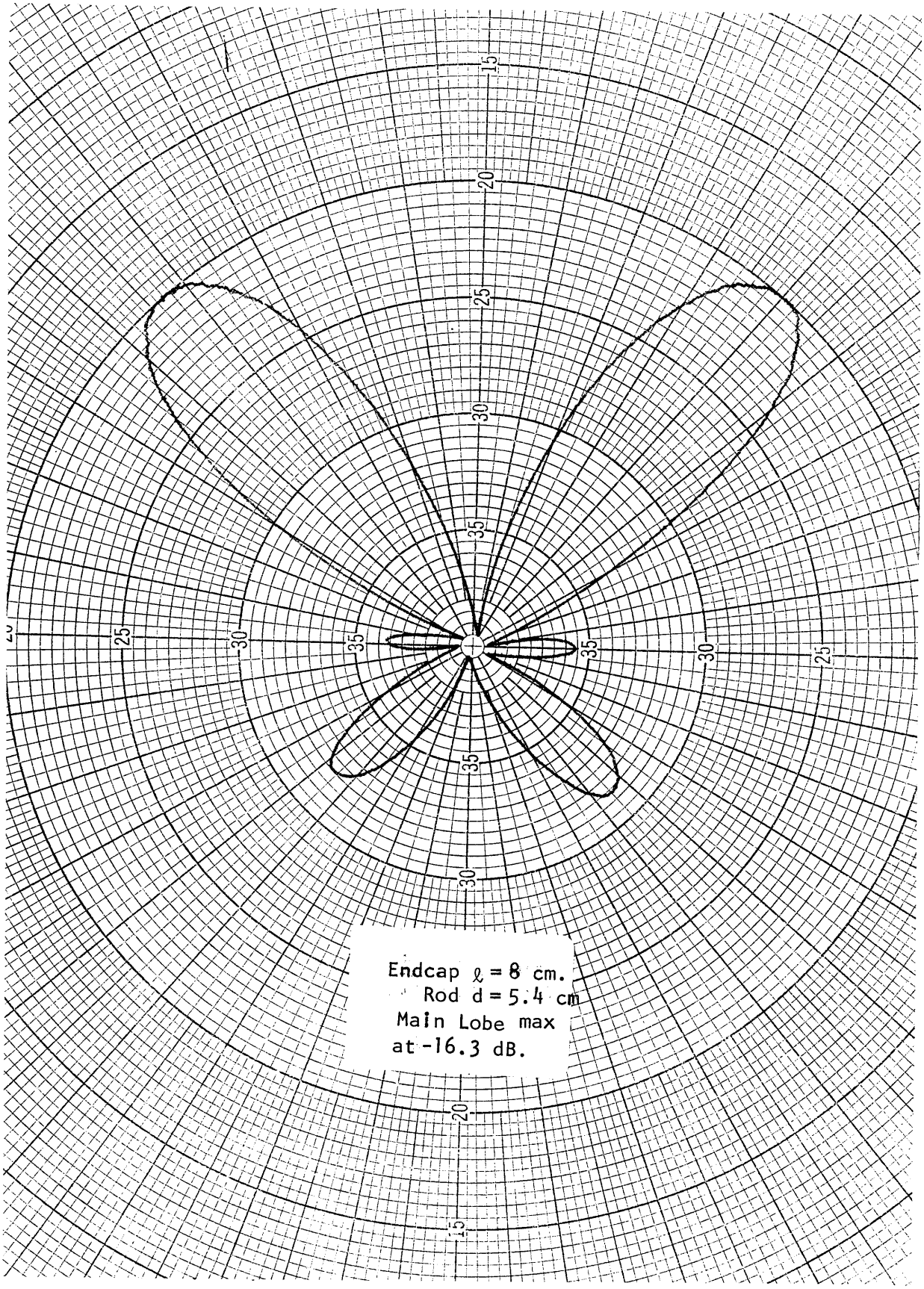

Figure 47. θ-Pattern for Modified End-Aperture Model.

coupling rod ($\ell = 0$) is evident; here, another 12 dB attenuation (+ 3 dB to -9 dB) of the main-lobe maximum is evident, from the absence of the TEM mode coupling that the rod would produce. The remaining Figures 46 and 47, which correspond to the end cap recessed by $\ell = 8$ cm, provide comparable results. A great number of experimental patterns have been obtained, but those given here are typical of the entire set.

A noteworthy common feature that characterizes all of the complete power patterns obtained from the modified end-aperture model is the nearly constant shape of the six-leaved patterns typified by Figure 42 through 47. These patterns, giving the relative power coupled into the detector by an incident plane wave arriving at different angles θ, have similar shapes because the exterior cylindrical antenna dimensions (overall length and decimeter) were left unchanged in obtaining these patterns. Only the coupling mechanism, comprised of the recessed end cap and attached rod, was altered by increments, thereby influencing primarily the relative power levels coupled into the detector. Changes in the coupling mechanism are seen to have little influence in changing the shapes of the patterns. Hence, this implies that the induced current on the antenna is less sensitive to the particular loading we have at the end of the antenna. Viewing the system for a moment (by reciprocity) as a transmitting antenna (with the detector removed and a generator now connected to the detector terminals), one may see that comparatively little power is expected to be radiated directly from the circular aperture region at the end; the primary influence on the radiation patterns is attributable to the current distribution achieved on the outer cylindrical wall, and coupled there from the aperture end. In view of the six-leaved patterns obtained, all of which exhibit major-lobes that point <u>away</u> from the aperture-end of the cylinder (symmetric about $\theta = 180^{o}$), a predominant traveling-wave contribution to the current distribution on the cylinder is evident.

2.2 Effect of the End Cap Location and Rod-Length

To permit measuring the power received at the load as a function of the end cap location d and rod-length ℓ, we have included in Table V a tabulation of the relative received power occurring at the major-lobe maximum for a large number of different combinations of d and ℓ. A careful examination of these data indicates that the received load-power is much less sensitive to the amount (d) by which the end cap is recessed than to the recess-distance $(d-\ell)$ of the end of the conducting rod. For example, for a fixed recess-distance $d-\ell = 2$ cm of the rod-end, it is observed that the two combinations of end-cap location and rod length ($\ell = 8$ cm, $d = 6$ cm) and ($\ell = 10$ cm, $d = 8$ cm) yield essentially the same result. To further demonstrate this effect, Fig. 48 shows a plot of the voltage output at the detector load, when the measurement is made at the major-lobe maximum, as a function of the rod recess-distance $(d-\ell)$. (Each dot in this figure represents a different combination of d and ℓ). The variation of the voltage-reading for a given distance $(d-\ell)$ is seen to be around 10% in all cases measured. This leads to the conclusion that the exponential decay of the circular waveguide modes in the portion of the cylinder without the center conducting rod is the most important factor determining the amount of power that can be transferred to the detector load.

2.3 Effect of Reactive Loading in the Cylindrical Enclosure.

In order to study the effects of loading on the performance of a cylindrical enclosure with an end-coupling scheme, we replaced the HP415B crystal mount, having a nominal input impedance of 50 ohms, with a FXR-N-210-B-57 crystal mount utilizing a built-in shunt inductance. This

replacement crystal mount has measured reactive impedance of 50 ohms at 300 MHz measured by standard coaxial slotted-line techniques. A typical result for the (uncalibrated) voltage pattern at the reactive load as a function of the incident angle is shown in Fig. 49. It is seen that although the magnitude of the reading may differ from that of a sensitive load, the pattern is basically the same for a given combination of end cap location and rod length. Thus, it further confirms our previous observation that the induced current on the external cylindrical surface (which acts like a receiving antenna) is relatively insensitive to the interior loading.

TABLE V

Relative Output Power at Major-Lobe Maximum
for Different d and ℓ Values

Endcap depth d (cm)	Rod-length (cm)	Relative Power (SWR Meter dB) at Major-Lobe Max	Detector RF Voltage (mV)
3 cm	0 cm	-17.5 dB	19.5
	5.4	- 3.7	95.7
4	5.4	-6.4	70.2
5	0	-27.7	6.0
	5.4	- 9.8	47.4
	6.4	- 6.5	69.4
	7.4	- 3.1	102.6
6	0	-32.5	3.5
	5.4	-14.1	28.9
	6.	-11.4	39.5
	6.4	- 9.8	47.4
	7.	- 7.5	66.8
	7.4	- 6.	73.5
	8.	- 3.8	94.6
	8.4	- 2.7	107.4
8	5.4	-23.8	9.5
	6.	-20.9	13.2
	6.4	-18.8	16.9
	7.	-16.1	22.9
	7.4	-14.	29.2
	8	-11.3	39.9
	8.4	- 9.4	49.6
	9.	- 7.2	64.0
	9.4	- 5.5	77.8
10	5.4	-32.9	3.3
	6.	-30.8	4.2
	6.4	-28.9	5.3
	7.	-26.3	7.1
	7.4	-24.1	9.1
	8.	-21.5	12.3
	8.4	-19.4	15.8
	9.	-16.1	22.9
	9.4	-14.7	27.0

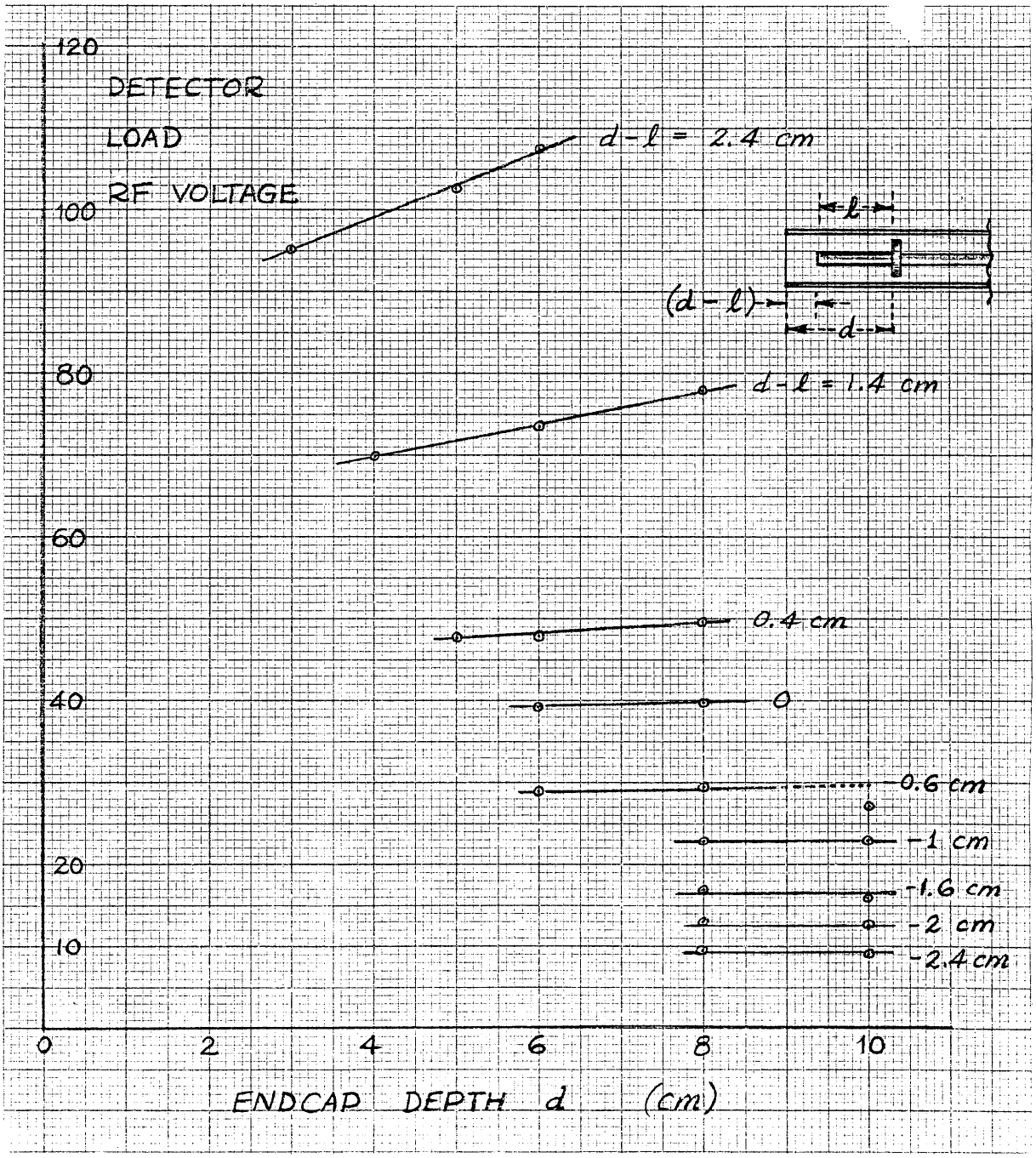

Figure 48. Variations of Detector Voltage with Endcap Depth d, for Several Recess Distance (d-ℓ) Values.

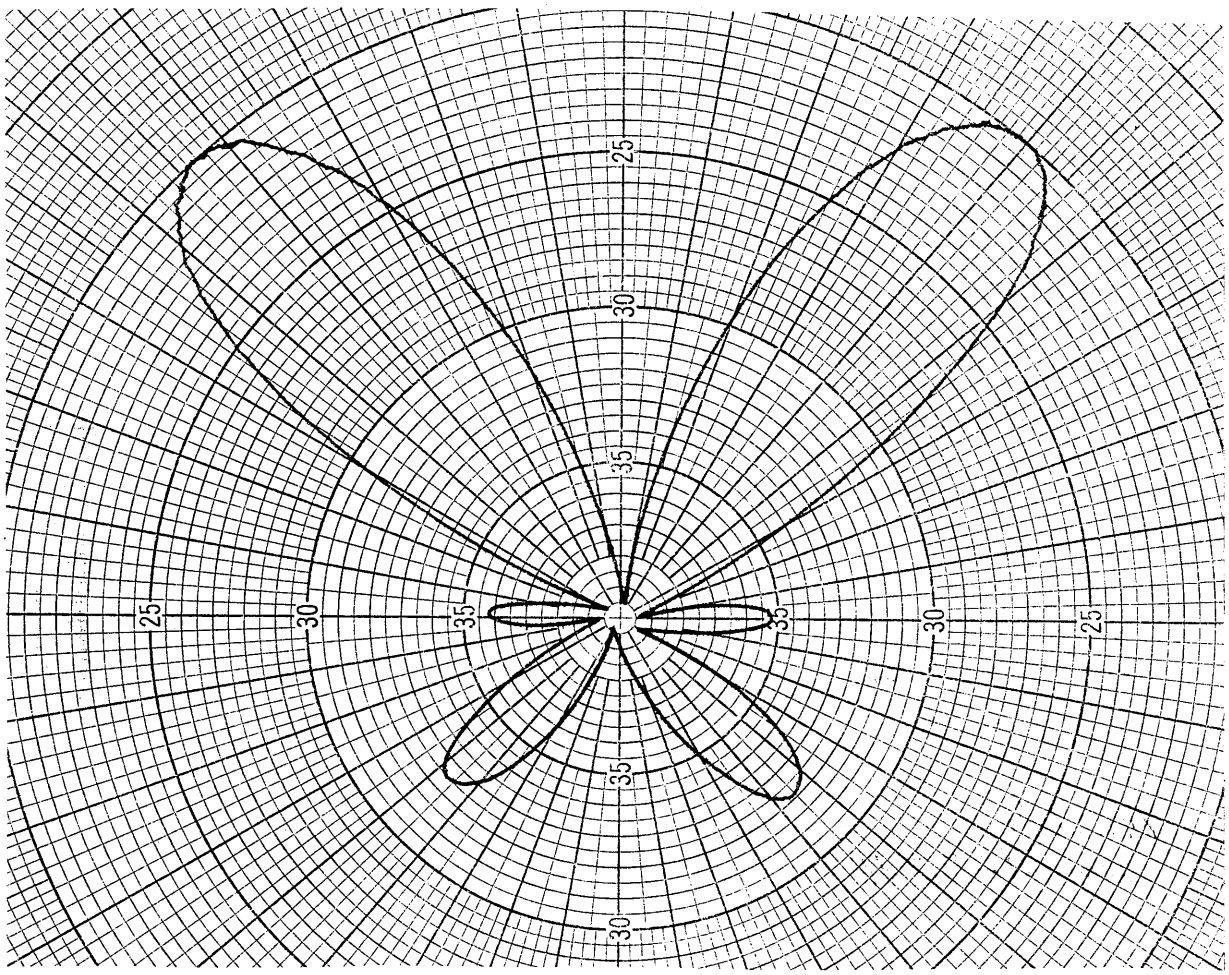

Figure 49. Typical θ-Pattern for Modified End-Aperture Model, Using Detector with Reactive Load Impedance.

PART IV

CONCLUDING REMARKS

In this report, we have investigated two of the more important coupling schemes in the study of electromagnetic penetration into cylindrical enclosures of lengths comparable to the free-space wavelength of an impinging electromagnetic wave. One of these concerns the penetration through a circular or elliptical hole on the cylindrical surface, and the other deals with the penetration through leakage between a recessed end-cap and the inner surface of the cylinder. In the first case, the amount of power received at a load inside the cylinder varies according to the different incident angles of an impinging wave generally in the same way as a thin-wire receiving antenna, with the exception that a strong azimuthal dependence of the hole location is observed. This probably means that when the size of a hole is comparable to the circumference of the cylinder (as is the case in our experiment) the direct penetration of the electromagnetic signal into the cylinder plays a significant role in determining the total performance of the enclosure. This leads us to conclude that a further theoretical investigation is indeed needed in order to be able to understand the mechanism governing the azimuthal variations, even though the average behavior of the cylinder over all azimuthal angles can be explained satisfactorily by the conventional theory of thin-wire receiving antennas.

In addition to the above observation, we have also verified from our measurements that the coupling through holes (within the framework of the thin-wire-and-small-aperture theory) can be looked upon as produced by an equivalent electric and an equivalent magnetic dipole located at the aperture. The magnitude of the electric dipole is determined by the short-circuit, induced-charge distribution at the aperture, while the magnetic dipole is more of a function of the induced current at that location. In the evaluation of the power received at a load inside the cylindrical enclosure, we found that the effects of these two dipoles differ from each other by a ratio determined by the transmission-line voltage and current at the location of these dipoles. Thus, when we terminate the coaxial line at one end (inside the enclosure) by a short-circuit plunger, the amount of power received at the other end by the 50-Ω detector is very sensitive to the position of the short-circuit plunger because it can provide a different tuning effect on the two dipoles. Since the induced charge distribution has a distinctively different dependence on the incident angle of an impinging electromagnetic wave compared to the current distribution, one may expect a very different received-power pattern at the load as a result of this tuning mechanism.

In the other coupling model, concerning the electromagnetic coupling through leakage past a recessed end cap, we observed that the azimuthal variation of the power reception pattern has now completely disappeared because of the symmetry of the coupling aperture existing between the outer rim of the end-cap and the inner surface of the cylindrical enclosure. However, the power reception pattern still differs from that of a thin-wire antenna of a same length in that a strong back lobe is consistently observed

in all the experimental data obtained for this model. A plausible explanation is obtained from the point of view of a transmitting antenna with a generator located at one end. When the length of the cylinder is long enough, the radiation from such a structure could conceptually be similar to that of a traveling-wave antenna. As the current is propagating along the cylinder toward the other end, it radiates in the forward direction and as a consequence, attenuates. Thus the magnitude of the reflected current is somewhat smaller than the forward current, and hence, it produces a smaller lobe in the far-field pattern in the direction toward the generator. Here again, further investigation of the theory of a receiving cylinder with loading at the end of the cylinder is certainly desirable.

Aside from the above considerations, we found that the power reception pattern at the load is very insensitive to the detailed configuration of the recessed end cap. However, for a fixed location of the recessed cap, the magnitude of the received power sharply increases as the length of the protruding conducting rod (which simulates possibly a wire assembly in front of the end cap) shortens. This points out the importance of avoiding any possible conducting lead in the section near the opening, if one is to minimize the extent of electromagnetic penetration in this test frequency-range.

Finally, we would like to make some remarks concerning the environmental effects as well as the frequency dependence on the experimental data we obtained. Throughout the entire investigation, we adopted an operating frequency of 300 MHz in our tests, even though data for 200 MHz were

included in the studies of the first coupling model. From a comparison of the results obtained at these two frequencies, one can appreciate how sensitively the performance of the cylindrical enclosure depended upon the operating frequency. We should further note that the cylinder can no longer be considered as electrically "thin" for frequencies much higher than the test frequencies used. Consequently, the theories we used to interpret our experimental results most certainly would not hold at much higher frequencies, while our experimental results obtained at 300 MHz and 200 MHz are also not indicative of what could happen at those frequencies. Thus we only reaffirm the fact that in any EMI, EMP and EMV studies, one must recognize the importance of the frequency dependence before he attempts to specify the shielding effectiveness of a certain enclosure.

In order to evaluate the environmental effects on the measured data, we have repeated our experiment for the end-coupling model with no absorbing material used in front of the antenna pedestal base, nor in the reflection region on the roof surface (Figure 50). One can see that although the power reception pattern does not change substantially with or without the absorbing material due to the specific type of reflection and the symmetrical geometry of the model, the amount of the received power can differ by a factor of 3, or as much as 5 dB, as a result of spurious reflections and scatterings. We then replaced the fiber-optics telemetry system by a conventional cable system and obtained the undesirable reception pattern as shown in Figure 51. We found that not only do the patterns obtained with the cable system bear very little or no resemblence to the one with a fiber telemetry system, but it can not even be repeated after a complete rotation of the model, simply because of the slight shifting of the cable

position that has occurred by virtue of the rotation. Although results in Fig. 50 and Fig. 51 are somewhat restrictive, they nevertheless demonstrate the importance of avoiding spurious electromagnetic scattering to help assure meaningful and repeatable measurements.

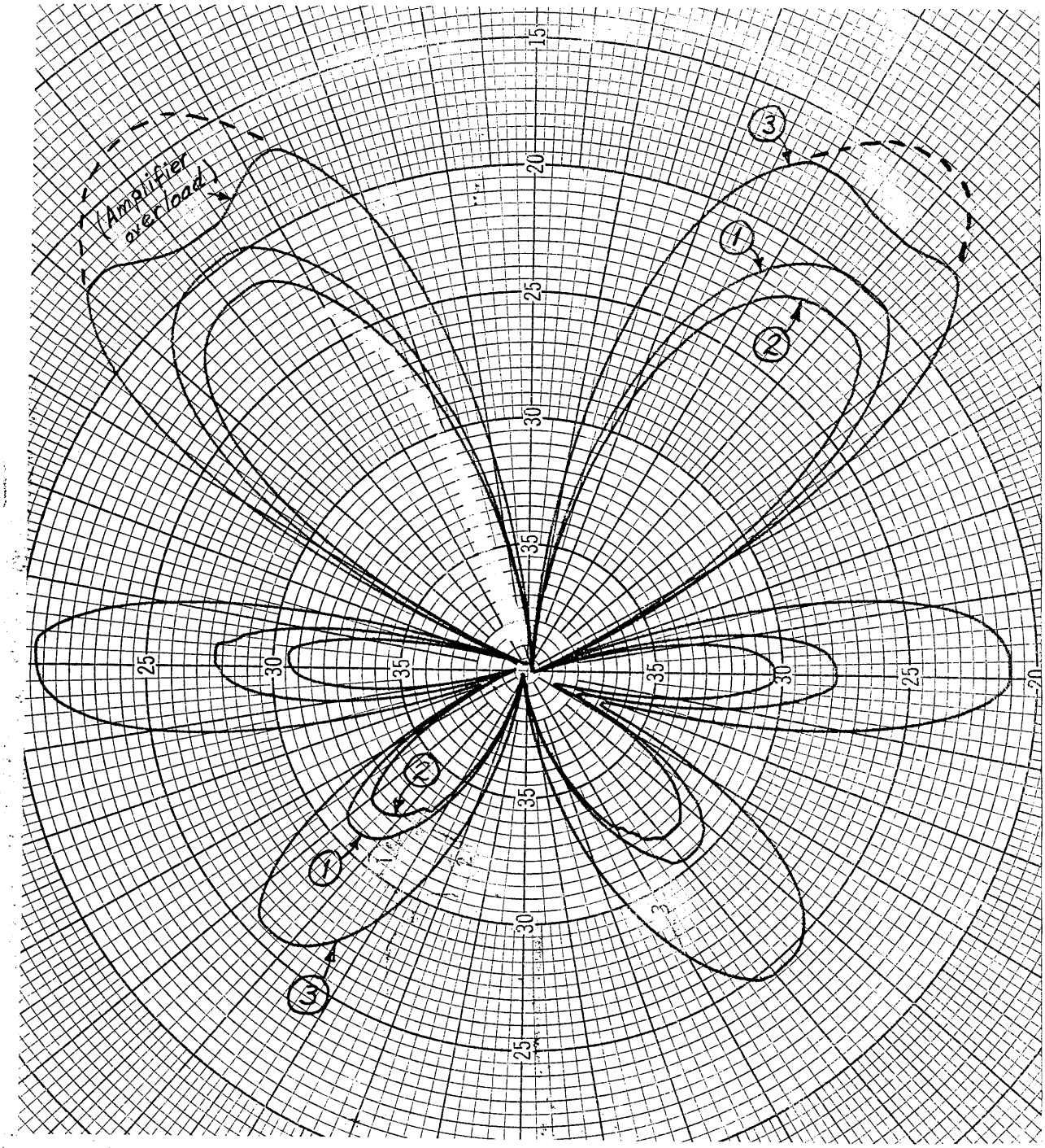

d = 0
ℓ = 0
Main lobe max at +7.1dB
(with absorbers)

1. With all absorbers in place.
2. Without antenna pedestal-base absorbers.
3. With no absorbers.

Figure 50. Pattern Variations Occurring with Reflection Absorbing Materials in Place or Not.

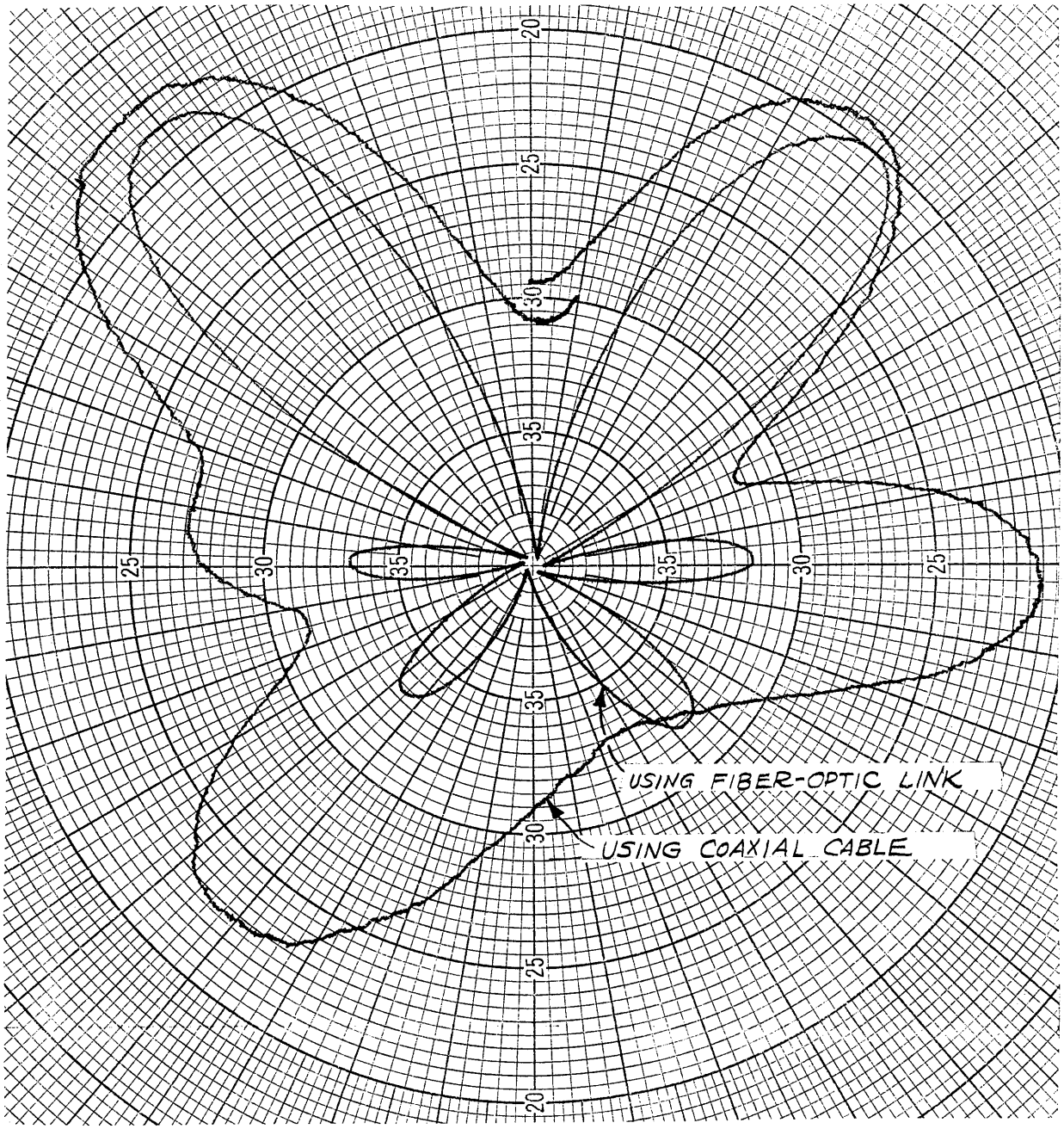

Figure 51. Showing Desirability of Using Fiber Optic Data Link Over a Coaxial Cable Output

LIST OF REFERENCES

Bethe, H.A., "Theory of Diffraction by Small Holes," Physical Review, Vol. 66, Ser. 2, pp. 163-182, 1944.

Bouwkamp, C.J., "Diffraction Theory," Reports on Progress in Physics, Vol. 17, pp. 75-100, 1954.

Chang, David C., Charles W. Harrison, Jr., and Clayborne D. Taylor, "Note Regarding the Propagation of Electromagnetic Fields Through Slots in Cylinders," IEEE Transactions on Electromagnetic Compatibility, Vol. EMC-15, No. 3, pp. 152-154, August 1973.

Chang, D.C. and S.W. Lee, "A Unified Theory of Receiving Antennas Based Upon Wiener-Hopf Technique," to be published.

Chang, D.C., "Radiation of a Buried Dipole in the Presence of a Semi-Infinite Metallic Tube," Radio Sci. Vol. 8, No. 2, pp. 147-154, 1973.

Chen, Y.M. and J.B. Keller, "Current on an Impedance of a Cylindrical Antenna," J. Res. NBS, Radio Propagat., 66D, 1, 15-21, 1962.

Cohn, S.B., "The Electric Polarizability of Apertures of Arbitrary Shape," Proc. I.R.E., Vol. 40, pp. 1069-1071, 1952.

Collin, R.E., Field Theory of Guided Waves. New York: McGraw-Hill, 1960, pp. 285-302.

Fikhmanas, R.F. and P.S. Fridberg, "Theory of Diffraction at Small Apertures. Computation of Upper and Lower Boundaries of the Polarizability Coefficients," Radio Eng. Electron, Phys. (USSR), Vol. 18, pp. 824-829, 1973.

Harrison, Charles W., Jr., and Ronald W.P. King, "Excitation of a Coaxial Line Through a Transverse Slot," IEEE Transactions on Electromagnetic Compatibility, Vol. EMC-14, No. 4, pp. 107-112, November 1972.

King, Ronald W.P., "Current Distribution in Arbitrarily Oriented Receiving and Scattering Antenna," IEEE Transactions on Antennas and Propagation, Vol. AP-20, No. 2, pp. 152-159, March 1972.

King, Ronald W.P., and C.W. Harrison, Jr., Antennas and Waves: A Modern Approach. Cambridge, Mass.: M.I.T. Press, 1969, p. 520.

Levine, H. and J. Schwinger, "The Radiation of Sound from an Unflanged Circular Pipe," Phys. Rev. Vol. 73, 383-406, 1968.

Mittra, R. and S.W. Lee, Analytical Techniques in the Theory of Guided Wave, MacMillan, New York, 1971.

Merewether, David E., "The Arbitrarily Driven Long Cylindrical Antenna," IEEE Transactions on Antennas and Propagation, Vol. 16, No. 6, pp. 769-770, November 1968.

Merewether, David E., "The Arbitrarily Driven Long Cylindrical Antenna," IEEE Transactions on Antennas and Propagation, Vol. 16, No. 6, pp. 769-770, November 1968.

Ramo, Simon, John R. Whinnery, and Theodore Van Duzer, Fields and Waves in Communication Electronics. New York: John Wiley & Sons, 1965, pp. 714-721.

Shen, Liang-Chi, "A Simple Theory of Receiving and Scattering Antennas," IEEE Transactions on Antennas and Propagation, Vol. 18, No. 1, pp. 112-114, January 1970.

Shen, Liang-Chi, Tai Tsun Wu, and Ronald W.P. King, "A Simple Formula of Current in Dipole Antennas," IEEE Transactions on Antennas and Propagation, Vol. 16, No. 5, pp. 542-547, September 1968.

Stratton, J.A., Electromagnetic Theory. New York: McGraw-Hill, 1941, p. 464.

Taylor, Clayborne D., "Electromagnetic Pulse Penetrations Through Small Apertures," IEEE Transactions on Electromagnetic Compatibility, Vol. EMC-15, No. 1, pp. 17-26, February 1973.

Taylor, C.D., and C.W. Harrison, Jr., "On the Excitation of a Coaxial Line by an Incident Field Propagating Through a Small Aperture in the Sheath," IEEE Transactions on Electromagnetic Compatibility, Vol. EMC-15, No. 3, pp. 127-131, August 1973.

Van Bladel, J., "Small-hole Coupling of Resonant Cavities and Waveguides," Proc. IEE, Vol. 17, pp. 1098-1104, 1970.

Weinstein, I.W. Theory of Diffraction and the Factorization Methods, Golem Press, Colo., 1969.

APPENDIX A

EQUIVALENT DIPOLE REPRESENTATION OF A SMALL APERTURE IN A CONDUCTING SCREEN

Collin [1960] used the Schelkunoff field-equivalence principle to obtain a fictitious magnetic current density J_m and magnetic charge density ρ_m to replace the physical on the surface bounded by the aperture, assumed electrically small to permit the assumption of constant fields over the aperture at any instant. The fields penetrating the aperture into the interior were imagined to be radiated from dipoles associated with J_m and ρ_m, the electrical field being related to an electric dipole by an electric polarizability α_e, with the magnetic field related to a magnetic dipole by a dyadic magnetic polarizability α_m.

The polarizability functions were associated with ellipsoidal dielectric and permeable magnetic bodies of dimensions ℓ_1, ℓ_2, ℓ_3 placed in uniform static electric and magnetic fields. The electric polarizability α_e was obtained by calculating the dipole moment for an ellipsoid of permittivity $\varepsilon = 0$ upon lettings its thickness ℓ_3 approach zero. A similar process with a permeable ellipsoid with $\mu = \infty$ was used to derive the magnetic polarizability $\overline{\alpha}_m$. The dipole moments obtained for the elliptic disks become

$$P_3 = - \frac{4\pi \ell_1^3 (1-e^2)}{3E(e)} \varepsilon_o E_o$$

$$M_1 = \frac{4\pi \ell_1^3 e^2}{3[K(e) - E(e)]} H_1$$

$$M_2 = \frac{4\pi \ell_1^3 e^2}{3[E(e) - (1-e^2)K(e)]} H_2$$

in which $K(e)$ and $E(e)$ are the complete elliptic integrals of the first and second kinds, respectively, and the parameter e is the eccentricity $(1 - \ell_2^2/\ell_1^2)$ of the elliptic disk.

The polarizabilities of the disks were taken to be the constants relating the dipole moments to their respective field components. Thus, for the dielectric disk,

$$\alpha_e = - \frac{4\pi\ell_1^3(1-e^2)}{3E(e)}$$

while for the permeable disk,

$$\bar{\alpha}_m = \bar{a}_u\bar{a}_u \frac{4\pi\ell_1^3 e^2}{3[K(e) - E(e)]} + \bar{a}_v\bar{a}_v \frac{4\pi\ell_1^3 e^2(1-e^2)}{3[E(e) - (1-e^2)K(e)]}$$

Thus far, the derivation has been straightforward. The question that can be raised is how the idealized case is related to the problem at hand. Collin has contended that the polarizabilities thus obtained must be divided by a factor of four. His argument is that since the ideal disk has two sides while the aperture surface being considered has only one (the one on the side of the metallic surface where the scattered fields are being calculated), the aperture polarizabilities are only half the magnitude of the polarizabilities of an ideal disk. Furthermore, Collin [1960, p. 295] has argued that since in his case the two cavities being considered (one containing the incident fields and another in which the penetration fields are to be determined) are symmetrical, only half of each aperture equivalent dipole moment contributes to the penetration fields. Collin's final results are

$$\alpha_e = \frac{4\pi \ell_1^3 (1-e^2)}{3E(e)}$$

and*

$$\bar{\alpha}_m = \bar{a}_u \bar{a}_u \frac{-\pi \ell_1^3 e^2}{3[K(e) - E(e)]} + \bar{a}_v \bar{a}_v \frac{-\pi \ell_1^3 e^2 (1-e^2)}{3[E(e) - (1-e^2)K(e)]} .$$

This means that on each side of the aperture, we can replace the aperture by an electric dipole $P = \alpha_e E$ and a magnetic dipole $M = \alpha_m \cdot H$ in front of a conducting screen, thus obtaining solutions to the scattered fields in the exterior or the interior regions separately in a straightforward manner. Here E and H denote the normal component of the electric field and the tangential magnetic field component respectively, when only one side is illuminated in the presence of the aperture.

In utilizing Collin's polarizability functions, Harrison and King [1972, p. 108] have multiplied the functions by a factor of two "to bring them into agreement with the results obtained by Bethe and Bouwkamp."

Harrison and Taylor utilized the polarizability functions as derived by Collin. However, a reference was made by them to a study by Taylor [1973], in which Collin's expressions were multiplied by a factor of two, raising the possibility of a typographical error in one of the two papers.

Taylor [1973, p. 25] referred to an experimental study by Cohn [1952] concerning the penetration fields of an aperture in a cylindrical structure. The results of this study appears to confirm the validity of the polarizability functions as used by Taylor.

---

*The additional factor -1 in these expressions accounts for the fact that the dipoles are oriented in the opposite direction from the unit normal vector on the shadow side of the metallic screen.

For the purposes of this paper, the polarizabilities derived by Collin are considered to be the correct ones. This expression can be indirectly confirmed by a more recent work of Van Bladel [1970] wherein the more general field penetration problem concerning a small aperture of any given shape and size is formulated in terms of the solution of two independent, quasi-static integral equations.

APPENDIX B

THEORIES OF THE ELECTROMAGNETIC PENETRATION THROUGH APERTURES ON THE OUTER SURFACE OF A COAXIAL CYLINDER

In this Appendix are described various theoretical solutions pertaining to the electromagnetic penetration through small apertures on a shielded, cylindrical enclosure. It includes, first of all, the analysis of Harrison and King [1972] which makes use of the Lorentz reciprocity theorem to obtain the desired result from a knowledge of the radiation property of the cylinder; and then the alternative approach of Taylor and Harrison [1973] for a normally-incident plane wave, and its form generalized for an arbitrary angle of incidence. The coordinate system as well as symbols employed in this discussion follow those of Figure 2 in Part II of this report.

In the operating frequency range of 200-300 MHz, the outer radius of the outer cylinder of the model designed is small enough (0.035 wavelength at 200 MHz and 0.051 wavelength at 300 MHz) that we expect thin-wire antenna theory to be reasonably accurate. The theories described in the following sections implicitly have assumed:

1. The outer wall has negligible thickness, and thus the inner radius and the outer radius of the outer sheath are the same.
2. The radius of the outer sheath is large when compared to the aperture diameter, so that the aperture surface is substantially planar.

3. The transverse dimension of the cylinder is assumed to be small compared to the wavelength, so that no transverse component of the exterior current is possible.
4. The aperture is electrically small, yielding electrical and magnetic fields there that are essentially constant at any given instant (the $e^{j\omega t}$ time dependence is suppressed).

B.1 Harrison-King Solution

Briefly, Harrison and King first considered the case of an infinitely long cylinder with very large outer radius; possible resonant currents on the outer surface of the cylinder were accounted for at a later point by use of a "correction factor" t. The structure was initially considered to be driven by an ideal voltage generator of magnitude V_o^e in series with the impedance Z_o located at $z=0$. The electromagnetic radiation from the structure was formulated and the current I_d at the center of a distant dipole due to the fields from the cylinder was determined. The generator was then moved to the center of the distant dipole and the reciprocity theorem was utilized to equate I_d with the desired current $I_z(0)$ at $z=0$. Determination of the current distribution in the coaxial line, calculation of the electric and magnetic fields at the aperture location, and formulation of equivalent electric and magnetic dipoles to represent the aperture were intermediate steps.

In addition to the assumptions stated before, Harrison and King implicitly assumed that the current and charge distributions along the exterior of the infinite cylinder are changed only in magnitude when the cylinder is of finite length. The assumption was also made that the

correction factor for exterior current magnitude was proportional to the ratio of the surface current density on the cylinder exterior to the surface current density on an infinite conducting plane. This in effect assumed a cylinder of infinite radius with no rotational component in the exterior current.

More specifically, an ideal generator is first assumed at $z = 0$. It produces a current distribution along the internal center conductor given by

$$I_z(z) = V_o^e \frac{F(w)}{D}$$

with a voltage distribution along the coaxial line given by

$$V(z) = Z_c V_o^e \frac{G(w)}{D} \quad .$$

In the above, Z_c is the coaxial-line characteristic impedance, while

$$F(w) = Z_c \cosh \gamma w + Z_{Load} \sinh \gamma w$$

$$G(w) = Z_c \sinh \gamma w + Z_{Load} \cosh \gamma w$$

$$D = Z_c(Z_0 + Z_s)\cosh \gamma s + (Z_c^2 + Z_o Z_s)\sinh \gamma s$$

and γ is the complex propagation constant.

The fields at the aperture in the outer conductor (inner radius b) are given by

$$B_\phi(b,\pi,\ell) = \frac{\mu_o}{2\pi b} I_z(\ell)$$

and

$$E_\rho(b,\pi,\ell) = \frac{\eta}{2\pi b Z_c} V(\ell)$$

where $\eta = \sqrt{\mu_o/\varepsilon_o}$.

The equivalent electric and magnetic dipoles are respectively:

$$P_\rho = \alpha_e \varepsilon E\ (b,\pi,\ell)$$

$$M_\phi = -\frac{\alpha_m}{\mu_o} B_\phi (b,\pi,\ell)$$

wherein:

$$\alpha_e = \frac{2\pi a_e^3 (1-k)}{3E(k)}$$

$$\alpha_m = \frac{-2\pi a_e^3 k}{3\ K(k) - E(k)}$$

and in which k is the eccentricity of the elliptical aperture, and $K(k)$ and $E(k)$ are the complete elliptic integrals of the first and second kinds, respectively. (It is seen that these values are exactly twice those obtained by Collin.)

For the E-field polarization parallel to the cylinder axis, the E_θ component is of interest. The E_θ component produced by the equivalent dipoles in front of a flat conducting screen reduces to

$$E_\theta = -V_o^e L(r) \left(\left[\frac{(1-k)G(s-\ell)}{E(k)} \right] \cos\theta + \frac{kF(s-\ell)}{K(k) - E(k)} \right) \cos\phi$$

in which:

$$L(r) = \frac{a_e^3\ \eta\beta^2}{12\pi bD} \cdot \frac{e^{-j\beta r}}{r}$$

r being the radial distance from the aperture to the field point, and $\beta = \omega\sqrt{\mu\varepsilon}$.

When the current produced in the distant dipole by E_θ is equated to the current I_z at $z=0$, the desired result for the current in Z_o is obtained:

$$I_z(0) = - \frac{jE^{inc} a_e^3 \beta}{3bD} \left(\frac{(1-k)G(s-\ell)}{E(k)} \cos\theta + \frac{kF(s-\ell)}{K(k) - E(k)} \right) \cos\phi$$

When the current at $z = s$ is of interest, it can be found by substituting $w = \ell$ for $w = 2-\ell$ in $F(w)$ and $G(w)$, giving

$$I_z(s) = - \frac{jE^{inc} a_e^3 \beta}{3bD} \left(\frac{(1-k)G(\ell)}{E(k)} \cos\theta + \frac{kF(\ell)}{K(k) - E(k)} \right) \cos\phi$$

The current $I_z(s)$ obtained thus far is for a cylinder of infinite exterior length. In order to find the current on a cylinder of finite length, a correction factor t was derived, by comparing the surface current density on the outside surface of the finite cylinder with the corresponding current density on the surface of an infinite plane.

The surface current density at a distance z_o from the center of an unloaded receiving antenna is given by Harrison and King [1972, p.110] as

$$K_{zu}(z_o) = \frac{j2E_z^{inc}}{\eta b \beta} \left(\frac{\cos \beta z_o - \cos \beta h}{\Psi_{du} \cos \beta h - \Psi_u(h)} \right)$$

where Ψ_{du} and Ψ_u are complex integrals not dependent on z, defined in Harrison and King [1972, p. 112] . The corresponding surface current density on an infinite plane was given in the same paper as

$$K_{z\infty} = \frac{2E_z^{inc}}{\eta} \quad .$$

The correction factor t was obtained from the ratio of $K_{zu}(z_o)$ to $K_{z\infty}$:

$$t = \frac{K_{zu}(z_o)}{K_{z\infty}} = \frac{j}{\beta b} \left(\frac{\cos \beta_o z_o - \cos \beta_o h}{\Psi_{du} \cos \beta_o h - \Psi_u(h)} \right) .$$

B.2 Taylor-Harrison Solution

The Taylor-Harrison solution uses a somewhat more straightforward approach than that employed in the Harrison-King analysis. The one-term approximation of King and Harrison [1969, p. 520] was used to obtain the current distribution on the exterior of the cylinder. The conservation of charge principle then yields the charge distribution on the cylinder exterior in terms of the current distribution. From these, the electric and magnetic fields at the aperture were obtained. The Collin polarizability functions were then used to find the penetration fields from which the differential voltage and current produced on the coaxial line were obtained. Finally, these differential expressions integrated over the length of the line gave the desired load currents.

We should mention that in this approach, the cylinder was assumed to be shorter than two wavelengths, so that the one-term current approximation could be used. In addition, the aperture can not be too close to the ends of the cylinder, $\ell^2 >> b^2$ and $(s-\ell)^2 >> b^2$.

More specifically, the current produced by the electric field normally incident on the exterior of the cylinder is given as

$$I_z^{ext}(z) = E_z^{inc} \frac{j4\pi}{\eta\beta} \cdot \frac{\cos \beta(z-s/2) - \cos \beta s/2}{\Psi_{du} \cos \beta s/2 - \Psi_u}$$

in which Ψ_{du} and Ψ_u are complex integrals independent of z and defined in Taylor and Harrison [1973, p. 128] . The external charge density is obtained from the z-derivative of this current, whence

$$\rho^{ext}(z) = \frac{j}{\omega} \cdot \frac{\partial}{\partial z} I_z^{ext}(z_o) .$$

The equivalent dipole moments are given by

$$M_\phi = \alpha_{xx} \frac{I_z^{ext}(z_o)}{2\pi b}$$

$$P_\rho = \alpha_{yy} \frac{\rho^{ext}(z_o)}{2\pi b}$$

where b is the cylinder outer radius and α_{xx} and α_{yy} are elements of the dyadic function defined by Taylor.

Starting with an expression for E_z within the cylinder, the differential voltage exciting the TEM mode expressed in terms of the equivalent magnetic and electric dipoles is obtained:

$$dV(z) = \left\{ \frac{\eta\beta^3 M_o}{4\pi} [g_2(z) - jg_3(z)] - \frac{\beta^3 P_o}{4\pi\varepsilon} [g_3(z) - jg_4(z) - 3g_5(z)] \right\} \beta(z-z_o)\, dz$$

wherein

$$g_u(z) = \frac{2\beta b}{\pi\beta^n} \int_o^\pi \left\{ \frac{\exp(-j\beta((z-z_o)^2 + 4b^2 \sin^2\phi)^{\frac{1}{2}}) \sin^2\phi}{((z-z_o)^2 + 4b^2 \sin^2\phi)^{n/2}} \right.$$

$$\left. - \frac{\exp(-j\beta((z-z_o)^2 + b^2)^{\frac{1}{2}})}{((z-z_o)^2 + b^2)^{n/2}} \right\} d\phi$$

The differential generator current is given by

$$dI_g(z) = \frac{dV(z)}{Z(s-z) + Z(z)}$$

in which $Z(z)$ and $Z(s-z)$ are the impedances seen looking down the transmission line from the differential generator. The use of transmission

line theory gives the following results for the differential current in the loads Z_o and Z_s:

$$dI_z(0) = -\frac{dV(z)}{D}\,[Z_c \cosh \gamma(s-z) + Z_s \sinh \gamma(s-z)]$$

$$dI_z(z) = \frac{dV(z)}{D}\,[Z_c \cosh \gamma z + Z_o \sinh \gamma z]$$

with*

$$D = Z_c(Z_o + Z_s)\cosh \gamma s + (Z_c^2 + Z_o Z_s)\sinh \gamma s\ .$$

The total load current is obtained by integrating the differential current contributions over the cylinder length. Approximating the integrals by the leading terms of Taylor series yields

$$I_z(0) = -j\,\frac{\eta\beta M_\phi}{4\pi b}\cdot\frac{1}{D}\,[Z_c[\cosh \gamma(s-z_o) + Z_s \sinh \gamma(s-z_o)]$$

$$-\frac{P_\rho}{4\pi b\varepsilon}\cdot\frac{\gamma}{D}\,[Z_s \cosh \gamma(s-z_o) + Z_c \sinh \gamma(s-z_o)]$$

$$I_z(s) = j\,\frac{\eta\beta M_\phi}{4\pi b}\cdot\frac{1}{D}\,[Z_c \cosh \gamma z_o + Z_o \sinh \gamma z_o]$$

$$-\frac{P_\rho}{4\pi\varepsilon b}\cdot\frac{\gamma}{D}\,[Z_o \cosh \gamma z_o + Z_c \sinh \gamma z_o\ ]$$

which are the desired results.** It should be noted that these expressions are for a cylinder of finite length and thus do not require an additional correction factor as does the Harrison-King solution.

---

*The formula appearing in Taylor and Harrison [1973] has been changed to eliminate an apparent error in the coefficient of the first term.

**It has been shown in Chang, Harrison and Taylor [1973] that given a dissipationless line ($\gamma = j\beta$), these results are exact.

B.3 Generalization of Taylor and Harrison's Result to a Plane Wave with an Arbitrary Angle of Incidence

The solutions previously discussed were intended for the case of broadside incidence. In most instances it is desirable to have a solution valid for arbitrary incidence angles. This can be accomplished by substituting into the previous solutions a more general expression for the current distribution on the exterior of the cylinder.

Many treatments of the problem of the thin dipole antenna with an arbitrary angle of incidence can be found in the literature. Two particularly interesting solutions of the problem are those of King [1972] and Shen [1970] . King has utilized his psi functions to obtain an accurate although quite complicated solution. Shen used an entirely different approach having the advantage of being mathematically simpler. Also, the physical currents being dealt with are more easily identified with the components of his solution. For these reasons, the Shen solution is used in this study. If greater accuracy is required, especially for short cylinders (less than one-half wavelength), the King approach may be more desirable, even though it is more complicated.

For reasons to be discussed in the next section, only the Taylor-Harrison solution is considered here. The Shen solution lends itself particularly well to this solution, since the external current expression is readily differentiated with respect to z to obtain the required charge density distribution.

The current on a receiving antenna consists of two parts , the first being the current caused on the antenna by the incident wave, while the

second is due to the equivalent voltage maintained across the load. When the load is a short circuit (as in the present case of a continuous cylinder), the second term is zero; hence, for the present case, the non-loaded current is the entire current.

In a previous paper dealing with a transmitting dipole (Shen, Wu, and King 1968), it was shown that the antenna current could be expressed as the superposition of an "outgoing wave" and waves reflected from the ends of the antenna. The same approach is used by Shen in his solution for the receiving antenna. Thus for the present case,*

$$I_z^{ext}(z) = I_R(z) = I_{NL}(z)$$

$$= I_{s\infty}(z,\theta_i) + C_{s1} I_\infty(h+z) + C_{s2} I_\infty(h-z)$$

in which

$$I_{s\infty}(z,\theta_i) = \frac{je^{j\beta_o z \cos\theta_i}}{\eta_o \sin\theta_i \left[C_w - \ell n \frac{\sin\theta_i}{2} + j\frac{\pi}{2}\right]} \cdot \frac{E^{inc}}{\lambda}$$

$$I_\infty(z) = \frac{je^{j\beta_o z}}{\eta_o} \ell n \left\{1 - \frac{2\pi i}{2C_w + \ell n[\beta z + (\beta_o^2 z^2 + e^{-2\gamma})^{\frac{1}{2}}] + \gamma + j\frac{3\pi}{2}}\right\}$$

with

$$C_w = \ell n(1/\beta b) - \gamma$$

$$\gamma = .57721566$$

θ_i = angle of incidence measured from the cylinder axis

and C_{s1} and C_{s2} are constants, given by

---

*The arguments of the $I_\infty(z)$ functions in the second and third terms have been corrected.

$$C_{s1} = \frac{RR_s(\pi-\theta_i) I_{s\infty}(h) I_\infty(2h) - I_{s\infty}(-h) R_s(\theta_i)}{1 - R^2 I_\infty^2(2h)}$$

$$C_{s2} = \frac{RR_s(\theta_i) I_{s\infty}(-h) I_\infty(2h) - I_{s\infty}(h) R_s(\pi-\theta_i)}{1 - R^2 I_\infty^2(2h)} .$$

The functions $R_s(\theta_i)$ and R are defined as

$$R_s(\theta_i) = \frac{\eta_o}{2\pi}\left[2C_w - \ell n \frac{1-\cos\theta_i}{2} + j\pi\right]$$

$$R = \frac{\eta_o}{\pi}\left[C_w + j\frac{\pi}{2}\right] .$$

The $I_z^{ext}(z,\theta_i)$ thus obtained was substituted for the one-term approximation for external current in the Harrison-Taylor study. The differentiation of current to obtain the charge density was performed on Shen's expression to obtain ρ^{ext} for the arbitrary angle of incidence solution. (For computational purposes, the complex conjugates of the I_z^{ext} and ρ^{ext} expressions were used, since Shen assumed an $e^{-j\omega t}$ time dependence of his solution while Taylor and Harrison assumed an $e^{j\omega t}$ time dependence.) It should be noted, however, an implicit assumption Shen had used in his work is that $\beta_o h \sin\theta_i$ should be much greater than one for a given incidence angle θ_i. Hence, his formula can not be expected to be even reasonably accurate for near-grazing angles (when $\theta_i \simeq 0$ or 180^o). A recent study by Chang and Lee [1975] has indicated that R_s has to be substantially modified in that case; a summary of their results is given in Appendix C.

B.4 Comparison of the Harrison-King and Taylor-Harrison Solutions

As is to be expected, the Harrison-King and Taylor-Harrison solutions are very similar. They are not, however, identical and an identification of their differences is necessary in order to determine which solution is more valid.

Examination of the two solutions reveals that the contribution by the equivalent dipole P_x in the Harrison-King solution is multiplied by the cosine of θ, while the Taylor-Harrison solution has no angular dependence. Furthermore, in the Harrison-King solution both the electric and the magnetic equivalent dipoles are multiplied by a single term dependent on the external current distribution on the cylinder and on the aperture location. Thus, their entire external z dependence is contained in the correction factor t. In the Harrison-Taylor solution, however, only the equivalent magnetic dipole is related to the cylinder external current and the aperture location. The equivalent electric dipole is rather related to the z-derivative of the current distribution. This it becomes evident that the two solutions can give the same result only when the aperture is centered on the length of the cylinder ($z = s/2$), or for the case when the transmission line function $G(w)$ equals zero, either having the effect of mullifying the contribution from the equivalent electric dipole. (As defined in Appendix B.1.), $G(w) = Z_c \sinh \gamma w + Z_{Load} \cosh \gamma w$.)

Shen's expression for the exterior current, as discussed in the preceding section, is of value in showing where the discrepancy lies. If the case of an infinitely long cylinder is first considered, Shen's expression for the exterior current reduces to

$$I_z^{ext}(z) = I_{s\infty}(z)$$

$$= \frac{je^{j\beta_o \cos\theta_i z}}{\eta_o \sin\theta_i \left[C_w - \ell n\left[\frac{\sin\theta_i}{2}\right] + j\frac{\pi}{2}\right]} .$$

Then, the corresponding axial charge density becomes

$$\rho^{ext}(z) = \frac{j}{\omega} \cdot \frac{\partial}{\partial z} I_{s\infty}(z)$$

$$= - \frac{j\beta_o \cos\theta}{\omega} I_{s\infty}(z) .$$

When the complete I_z^{ext} and ρ^{ext} expressions given above are used in place of the King one-term approximation in the Taylor-Harrison solution for an infinite cylinder, it is easily seen that the contribution to the load current from the equivalent electric dipole is multiplied by cosine , as in the Harrison-King solution.

However, for the case of a cylinder of finite length, Shen's $I_{s\infty}(z)$ is not the only term contributing to the external current on the cylinder; there are also contributions from the reflections at the cylinder ends. Thus, for the cylinder of finite length, the complete expression for current given by

$$\rho^{ext} \simeq - \frac{j\beta_o}{\omega} [\cos\theta \, \rho_{s\infty}(z) + C_{s1}\rho_\infty (z-h) + C_{s2}\rho_\infty(z+h)]$$

Now, both the Harrison-King and the Taylor-Harrison solutions are valid for boradside incidence only. For the broadside case, the contribution from the equivalent electric dipole must be identically zero in the

Harrison-King solution. However, it is readily seen from the above expression that this is not possible since ρ^{ext} is not identically zero for $\theta = \pi/2$ and the contribution from the equivalent electric dipole is directly proportional to ρ^{ext}.

In view of this contradiction, it would seem evident that the assumption made by Harrison and King, namely that only the magnitude of the current distribution on the exterior of the cylinder is changed when going from the infinitely long to the finite-length case, is not warranted. Furthermore, it appears that the Harrison-King solution is valid only for certain special cases involving broadside incidence, specifically those in which the transmission-line function $G(w) = 0$. Since no such shortcoming has been found in the Taylor-Harrison solution, it is the one used for the prediction of load current in this study.

B.5 Numerical Comparisons of the King One-Term Approximation and the Shen Formulation for Exterior Current Distribution

In devising a computer program to calculate theoretically the power dissipated in the load due to an incident plane wave, we have developed a computer code based upon the generalized form of the Taylor-Harrison formula (Appendix D). To verify the correctness of the computer program, several test runs and comparisons with the King one-term theory originally used by Harrison and Taylor were made. This was considered necessary not only to "debug" the computer program, but also because the Shen paper contains the restriction that $\beta_o a \leq .08$ (a is the cylinder outer radius), while in the present case $\beta_o a \cong 0.3$.

First the function $I_{inf}(z)$ in the Shen formulation was evaluated at $z = 0$. The result was 2.33, compared to the value 2.3 obtained by Shen [1968, p. 542]. Next, the exterior current $I_{nl}(z)$ for $h/\lambda = 0.75$ was evaluated and compared with the distribution shown by Shen [1970, p. 113] . Again the results showed excellent agreement (the arguments of the second and third terms if $I_{nl}(z)$ were corrected, as noted in Section B.3). Finally, the exterior current $I_{nl}(z)$ was compared to the King one-term theory for a normally-incident phase-wave in three test cases. The results of these comparisons are shown in Tables B-I through B-III and are plotted in Figures B-1 through B-3. Figures B-1 and B-2 show the magnitude of the exterior current as a function of cylinder length for $\beta_o = 0.05$ and $\beta_o = 0.3$ respectively; while Figure B-3 shows the exterior current magnitude as a function of cylinder radius for the fixed length $2h = \lambda$. The results show that the King one-term theory and the Shen theory give excellent agreement for cylinder lengths not close to resonance. There is, however, some disagreement between the two theories for the resonant lengths. The King theory shows the magnitude of the exterior current to be greater at the second resonance $(2h \simeq 1.4\lambda)$ than at the first resonance $(2h \simeq .4\lambda)$, while the Shen theory gives the opposite result. Merewether [1968, p.770] gives theoretical and experimental data which tend to support the Shen theory. Furthermore, the King one-term theory is expressly for short antennas while the Shen theory improves for longer antennas. Thus, it would appear that the Shen theory does provide the more accurate solution and that the computer program of the Shen formulation was correct. (The computer programs used are found in Appendix D.)

TABLE B-1

EXTERIOR CURRENT VERSUS LENGTH FOR Ka = .05

$2h/\lambda$	King one-term approximation*			Shen formulation*		
	$Re(I_z^{ext})$	$Im(I_z^{ext})$	$\lvert I_z^{ext} \rvert$	$Re(I_z^{ext})$	$Im(I_z^{ext})$	$\lvert I_z^{ext} \rvert$
.40	1.72E-03	2.36E-03	2.92E-03	2.32E-03	3.09E-03	3.87E-03
.45	4.37E-03	8.68E-04	4.46E-03	5.55E-03	-5.44E-05	5.55E-03
.50	3.27E-03	-1.77E-03	3.72E-03	3.05E-03	-2.38E-03	3.87E-03
.55	1.94E-03	-1.99E-03	2.78E-03	1.75E-03	-2.18E-03	2.80E-03
.60	1.34E-03	-1.81E-03	2.25E-03	1.23E-03	-1.90E-03	2.26E-03
.65	1.05E-03	-1.64E-03	1.95E-03	9.76E-04	-1.70E-03	1.96E-03
.70	8.86E-04	-1.53E-03	1.76E-03	8.32E-04	-1.57E-03	1.78E-03
.75	7.86E-04	-1.45E-03	1.65E-03	7.42E-04	-1.48E-03	1.66E-03
.80	7.23E-04	-1.39E-03	1.57E-03	6.82E-04	-1.43E-03	1.58E-03
.85	6.81E-04	-1.36E-03	1.52E-03	6.40E-04	-1.39E-03	1.53E-03
.90	6.53E-04	-1.34E-03	1.49E-03	6.09E-04	-1.38E-03	1.51E-03
.95	6.35E-04	-1.35E-03	1.49E-03	5.86E-04	-1.38E-03	1.50E-03
1.00	6.24E-04	-1.37E-03	1.50E-03	5.67E-04	-1.40E-03	1.51E-03
1.05	6.19E-04	-1.40E-03	1.53E-03	5.51E-04	-1.43E-03	1.53E-03
1.10	6.17E-04	-1.47E-03	1.59E-03	5.34E-04	-1.49E-03	1.58E-03
1.15	6.17E-04	-1.56E-03	1.68E-03	5.12E-04	-1.58E-03	1.66E-03
1.20	6.15E-04	-1.71E-03	1.81E-03	4.74E-04	-1.72E-03	1.79E-03
1.25	6.00E-04	-1.94E-03	2.03E-03	3.97E-04	-1.93E-03	1.97E-03
1.30	5.31E-04	-2.33E-03	2.39E-03	2.12E-04	-2.27E-03	2.28E-03
1.35	2.37E-04	-3.05E-03	3.06E-03	-3.01E-04	-2.75E-03	2.77E-03
1.40	-1.25E-03	-4.26E-03	4.44E-03	-1.71E-03	-2.95E-03	3.41E-03
1.45	-4.85E-03	-1.81E-03	5.17E-03	-2.98E-03	-1.10E-03	3.18E-03
1.50	-2.51E-03	1.02E-03	2.71E-03	-1.91E-03	3.66E-04	1.94E-03
1.55	-1.11E-03	8.52E-04	1.40E-03	-9.83E-04	4.84E-04	1.10E-03
1.60	-5.70E-04	5.59E-04	7.98E-04	-5.21E-04	3.54E-04	6.30E-04

*All values in amperes/volt/meter.

TABLE B-2

EXTERIOR CURRENT VERSUS LENGTH FOR Ka = .3

$2h/\lambda$	King one-term approximation*			Shen formulation*		
	$Re(I_z^{ext})$	$Im(I_z^{ext})$	$\lvert I_z^{ext}\rvert$	$Re(I_z^{ext})$	$Im(I_z^{ext})$	$\lvert I_z^{ext}\rvert$
.40	4.71E-03	1.24E-03	4.88E-03	8.65E-03	-2.00E-03	8.87E-03
.45	4.58E-03	-4.72E-04	4.60E-03	4.87E-03	-2.94E-03	5.69E-03
.50	3.83E-03	-1.34E-03	4.06E-03	3.42E-03	-2.64E-03	4.32E-03
.55	3.19E-03	-1.65E-03	3.59E-03	2.73E-03	-2.36E-03	3.61E-03
.60	2.74E-03	-1.74E-03	3.25E-03	2.35E-03	-2.17E-03	3.20E-03
.65	2.44E-03	-1.75E-03	3.00E-03	2.12E-03	-2.04E-03	2.94E-03
.70	2.24E-03	-1.73E-03	2.83E-03	1.96E-03	-1.95E-03	2.77E-03
.75	2.10E-03	-1.72E-03	2.71E-03	1.86E-03	-1.90E-03	2.66E-03
.80	2.01E-03	-1.71E-03	2.64E-03	1.79E-03	-1.88E-03	2.59E-03
.85	1.96E-03	-1.71E-03	2.60E-03	1.74E-03	-1.88E-03	2.56E-03
.90	1.93E-03	-1.73E-03	2.59E-03	1.70E-03	-1.91E-03	2.56E-03
.95	1.92E-03	-1.77E-03	2.62E-03	1.66E-03	-1.96E-03	2.59E-03
1.00	1.94E-03	-1.84E-03	2.67E-03	1.67E-03	-2.05E-03	2.65E-03
1.05	1.98E-03	-1.94E-03	2.77E-03	1.67E-03	-2.19E-03	2.76E-03
1.10	2.05E-03	-2.09E-03	2.93E-03	1.66E-03	-2.41E-03	2.92E-03
1.15	2.15E-03	-2.32E-03	3.17E-03	1.62E-03	-2.73E-03	3.17E-03
1.20	2.29E-03	-2.70E-03	3.54E-03	1.48E-03	-3.24E-03	3.56E-03
1.25	2.47E-03	-3.35E-03	4.16E-03	1.02E-03	-4.04E-03	4.17E-03
1.30	2.55E-03	-4.64E-03	5.30E-03	-4.71E-04	-4.96E-03	4.96E-03
1.35	1.42E-03	-7.55E-03	7.68E-03	-3.22E-03	-3.92E-03	5.07E-03
1.40	-6.31E-03	-7.75E-03	9.99E-03	-3.38E-03	-9.72E-04	3.51E-03
1.45	-5.57E-03	-2.61E-04	5.57E-03	-2.05E-03	1.80E-04	2.04E-03
1.50	-2.77E-03	7.38E-04	2.86E-03	-1.11E-03	3.06E-04	1.16E-03
1.55	-1.52E-03	6.39E-04	1.65E-03	-5.69E-04	3.30E-04	6.57E-04
1.60	-8.89E-04	4.65E-04	1.00E-03	-2.43E-04	2.59E-04	3.55E-04

*All values in amperes/volt/meter.

TABLE B-3

EXTERIOR CURRENT VERSUS RADIUS FOR $2h/\lambda = 1.0$

Ka	King one-term approximation*			Shen formulation*		
	$Re(I_z^{ext})$	$Im(I_z^{ext})$	$\lvert I_z^{ext} \rvert$	$Re(I_z^{ext})$	$Im(I_z^{ext})$	$\lvert I_z^{ext} \rvert$
.02	4.03E-04	-1.14E-03	1.21E-03	3.72E-04	-1.16E-03	1.21E-03
.04	5.57E-04	-1.30E-03	1.42E-03	5.08E-04	-1.33E-03	1.42E-03
.06	6.88E-04	-1.42E-03	1.58E-03	6.22E-04	-1.45E-03	1.58E-03
.08	8.09E-04	-1.51E-03	1.71E-03	7.26E-04	-1.55E-03	1.71E-03
.10	9.23E-04	-1.58E-03	1.83E-03	8.24E-04	-1.63E-03	1.83E-03
.12	1.03E-03	-1.63E-03	1.93E-03	9.18E-04	-1.70E-03	1.93E-03
.14	1.14E-03	-1.68E-03	2.03E-03	1.01E-03	-1.76E-03	2.03E-03
.16	1.25E-03	-1.72E-03	2.13E-03	1.10E-03	-1.81E-03	2.12E-03
.18	1.35E-03	-1.76E-03	2.21E-03	1.18E-03	-1.86E-03	2.20E-03
.20	1.45E-03	-1.78E-03	2.30E-03	1.27E-03	-1.90E-03	2.29E-03
.22	1.55E-03	-1.80E-03	2.38E-03	1.35E-03	-1.94E-03	2.36E-03
.24	1.65E-03	-1.82E-03	2.46E-03	1.43E-03	-1.97E-03	2.44E-03
.26	1.75E-03	-1.83E-03	2.53E-03	1.51E-03	-2.00E-03	2.51E-03
.28	1.85E-03	-1.84E-03	2.60E-03	1.59E-03	-2.03E-03	2.58E-03
.30	1.94E-03	-1.84E-03	2.67E-03	1.67E-03	-2.05E-03	2.65E-03
.32	2.04E-03	-1.84E-03	2.74E-03	1.75E-03	-2.08E-03	2.72E-03
.34	2.13E-03	-1.83E-03	2.81E-03	1.83E-03	-2.09E-03	2.78E-03
.36	2.23E-03	-1.82E-03	2.88E-03	1.91E-03	-2.11E-03	2.84E-03
.38	2.32E-03	-1.81E-03	2.94E-03	1.98E-03	-2.12E-03	2.90E-03
.40	2.41E-03	-1.79E-03	3.00E-03	2.06E-03	-2.13E-03	2.96E-03

*All values in amperes/volt/meter.

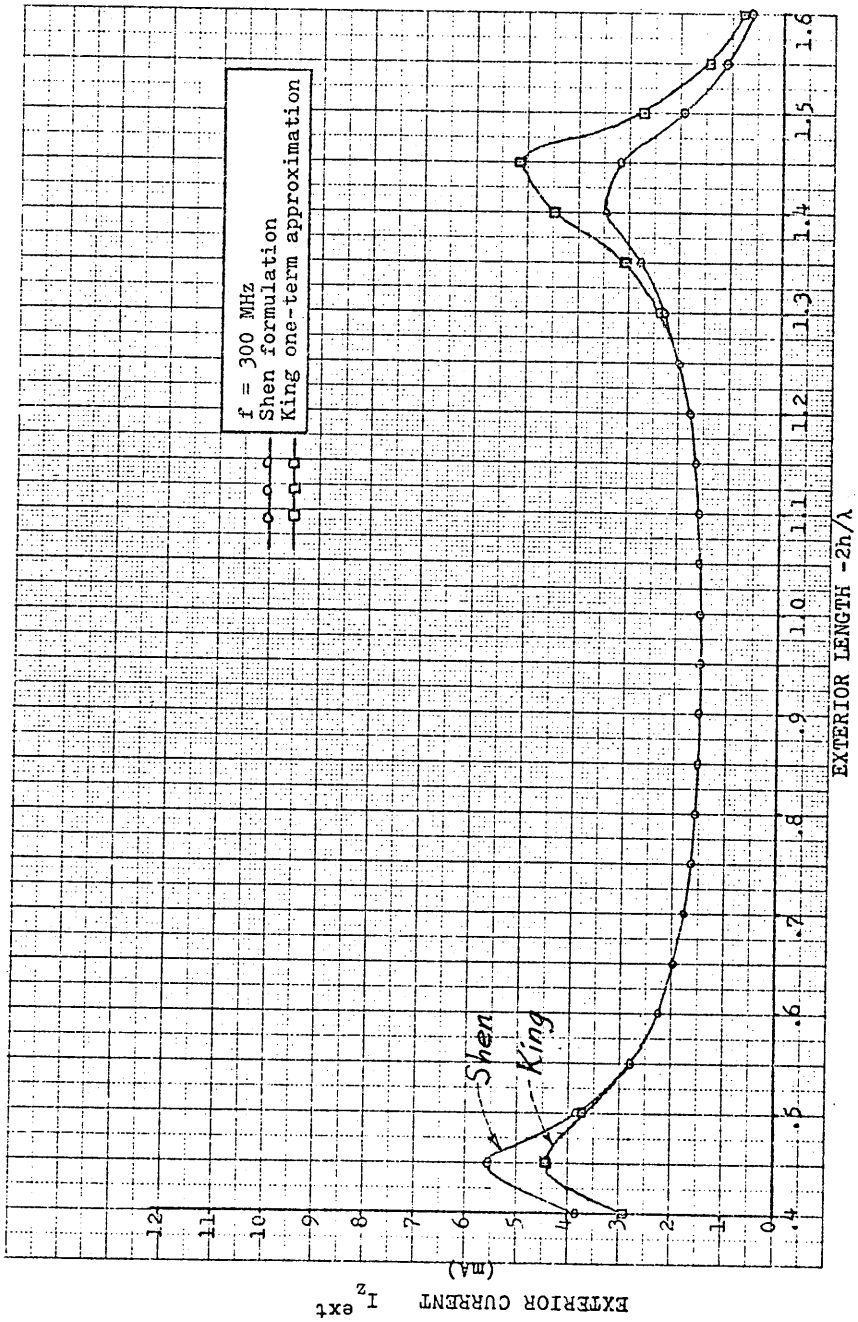

Figure B-1. Exterior Current versus Exterior Length for Ka = .05

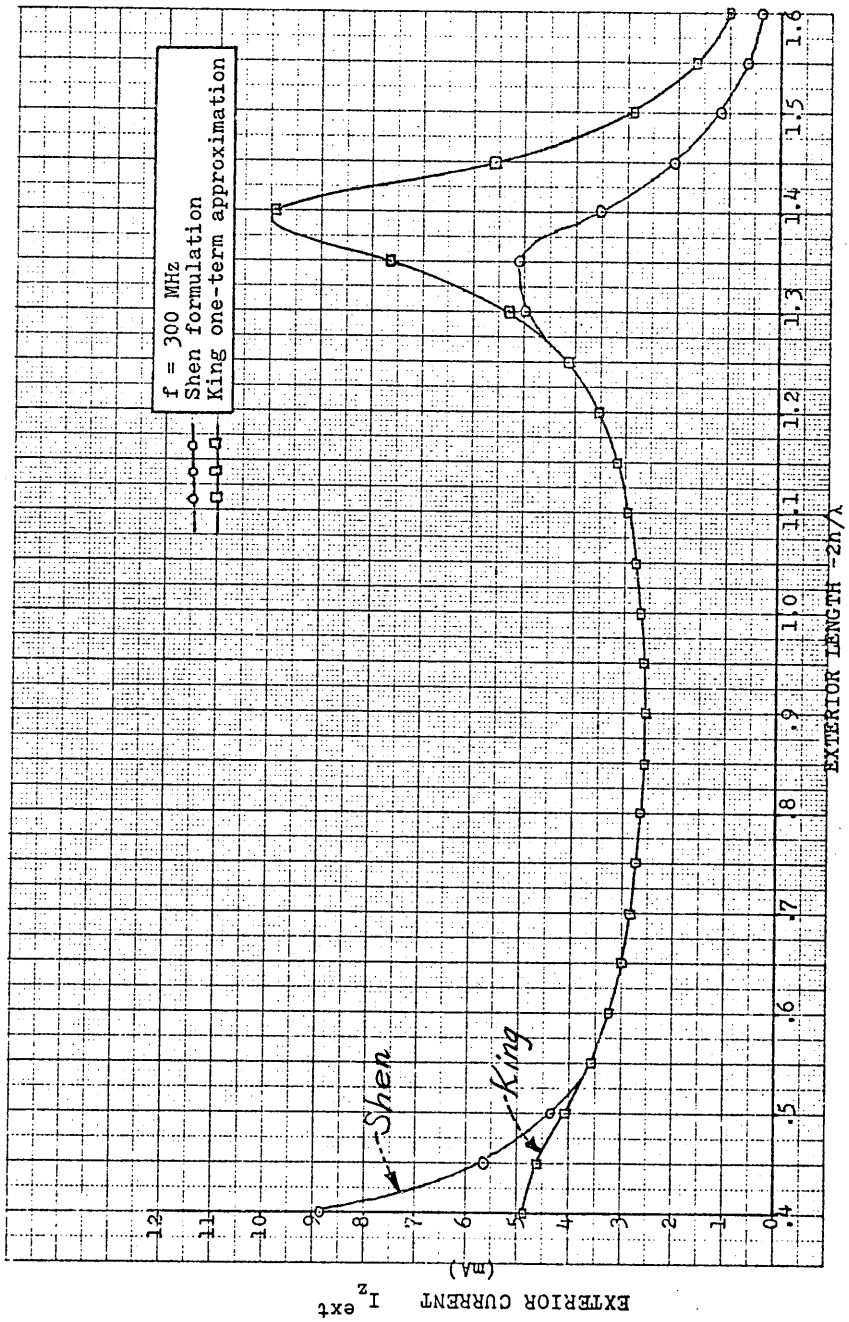

Figure B-2. Exterior Current versus Exterior Length for Ka = .30

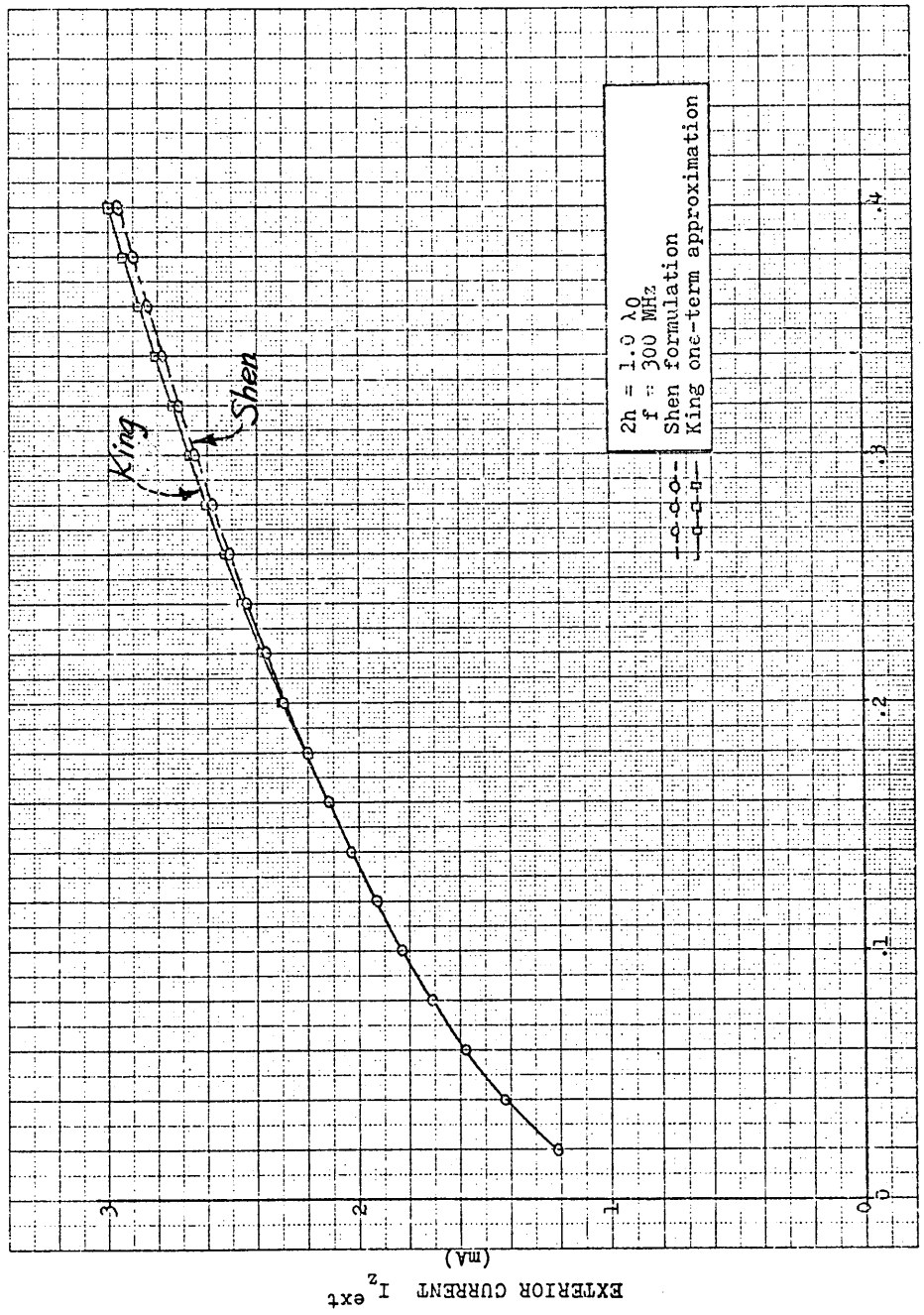

Figure B-3. Exterior Current versus Exterior Radius for $2h/\lambda = 1.0$

B.6 Theoretical Calculation of Load Power as a Function of the Incidence Angle θ

The theoretical average power delivered to the load impedance Z_s as a function of the declination (off-axis) angle θ is shown in Tables B-5 and B-6, based upon the generalized form of Taylor-Harrison's formula (Appendix D). Data for the case of a 200 MHz are included. A one-inch diameter circular aperture was used, with the aperture offset by 0.039 m in order to agree with the dimensions used in the experimental model. The theoretical pattern for the shorter wavelength (f = 300 MHz) is shown in Figure B-4, while that for the longer wavelength (f = 200 MHz) is shown in Figure B-5. Since the Shen theory of the current distribution assumes no ϕ variation, the patterns are symmetric about the cylinder axis.

As mentioned before, the Shen theory is not valid for grazing angles of incidence (close to 0° or 180°). Thus, while the polar plot of load power versus θ for the 200 MHz case shows the load power increasing indefinitely as θ approaches 180°, that result is not physically realizable and should be discounted. The part of the plot for $|\theta| > 140^\circ$ is therefore shown in dashed lines.

TABLE B-5

THEORETICAL POWER DELIVERED TO Z_s VERSUS θ AT 200 MHz

θ (degrees)	Power*
20	1.26
30	1.80
40	9.36
50	24.78
60	46.40
70	66.38
80	73.20
90	60.71
100	35.28
110	11.50
120	.79
130	5.56
140	24.10
150	61.89
(160)	(159.13)

*The power values have been normalized to lie in a range from 0 - 100 units.

$2h = 1.39$ m
$\ell = .5$ m
one-inch diameter circular aperture

TABLE B-6

THEORETICAL POWER DELIVERED TO Z_s VERSUS θ AT 300 MHz

θ (degrees)	Power*
20	52.01
30	80.63
40	98.46
50	82.18
60	36.17
70	4.45
80	13.57
90	25.17
100	8.96
110	5.15
120	44.52
130	90.20
140	100.00
150	76.45
160	45.30

*The power values have been normalized to lie in a range from 0 - 100 units.

$2h = 1.39$ m
$\ell = .5$ m
one-inch diameter circular aperture

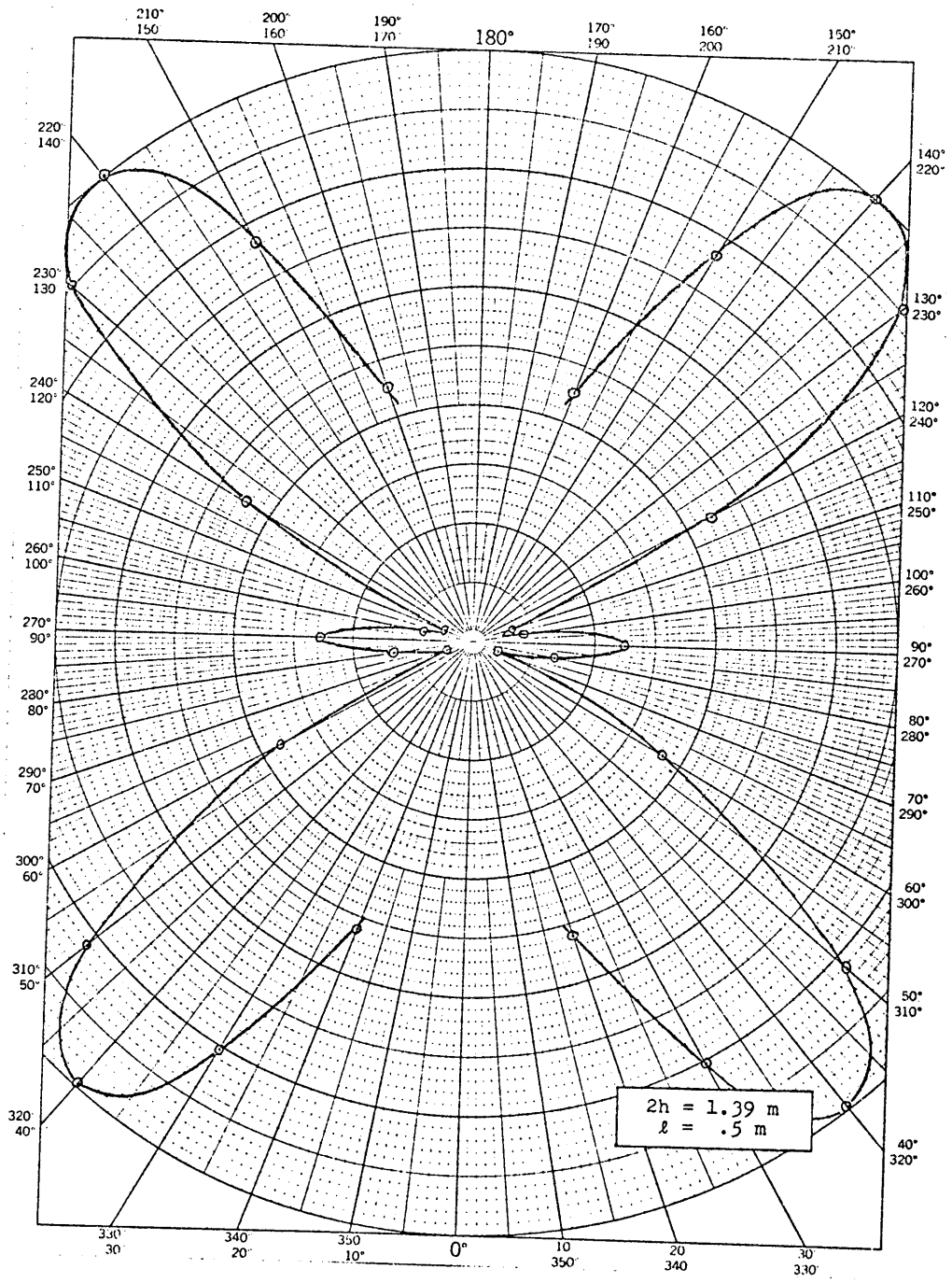

Figure B-4. Theoretical Power Pattern for an Operating Frequency of 300 MHz

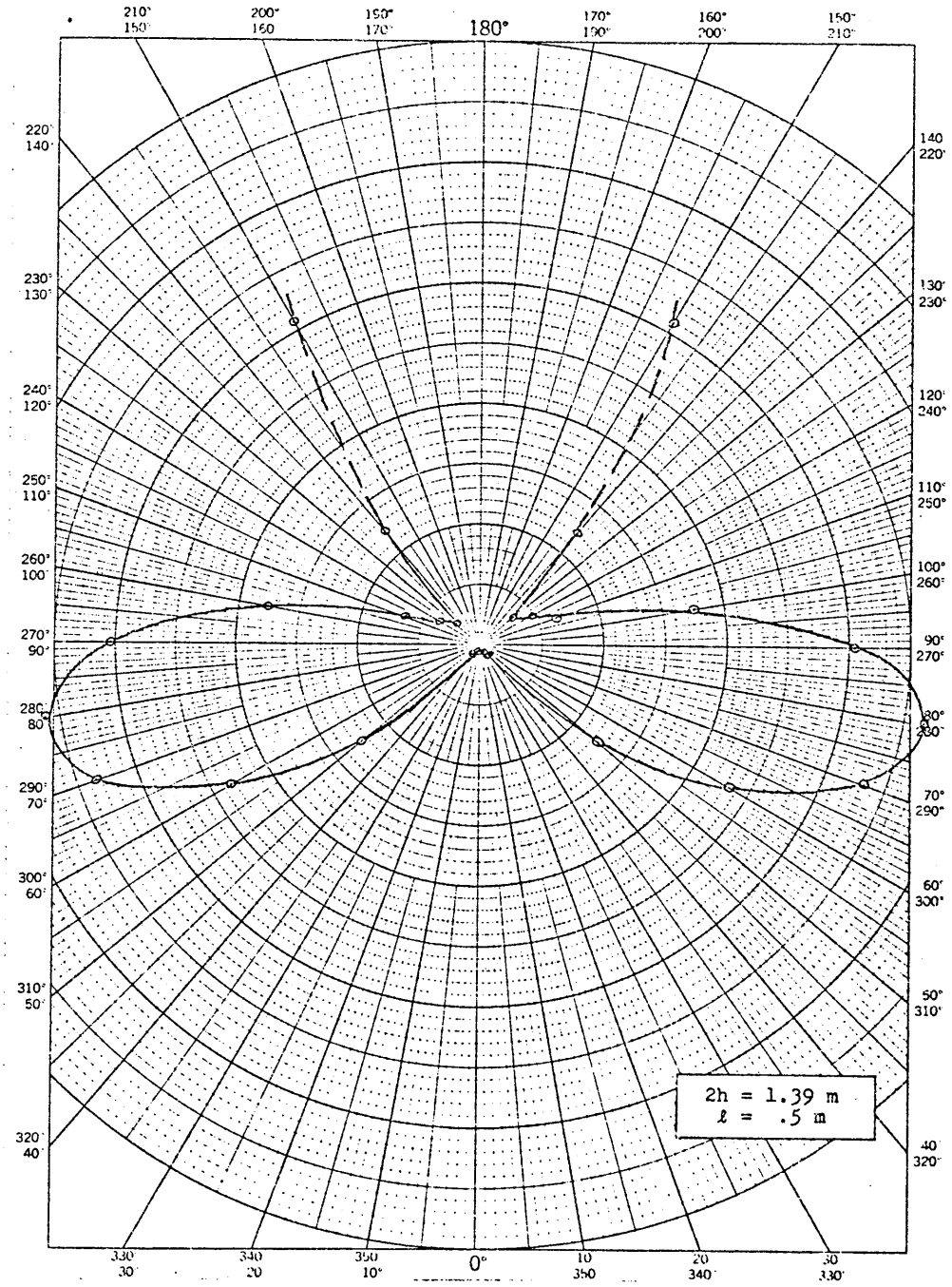

Figure B-5. Theoretical Power Pattern for an Operating Frequency of 200 MHz

APPENDIX C

ELECTROMAGNETIC PENETRATION INTO A TUBULAR CYLINDER

In this Appendix, the work of Chang and Lee [private communication], is summarized in an effort to extend Shen's result (as described in Appendix B) to the case of near-grazing wave incidence. As pointed out by Chang and Lee, the building block in Shen's solution is the canonical problem of a plane-wave incident upon a semi-infinitely long, tubular cylinder. The current distribution on the cylinder in this case is obtained formally in terms of an integral

$$I(z) = AE_{\theta}^{i} \int_{c} \frac{e^{+i\alpha z}\, d\alpha}{(\alpha-\beta_o)(\alpha-\beta_o \cos\theta) K_{-}(\alpha)}$$

wherein

$$A = 2 \sin\theta_i [\eta_o (1+\cos\theta_i) K_{+}(\beta_o \cos\theta_i)]^{-1} ,$$

$$K_{+}(\alpha) = K_{-}(-\alpha);\ K(\alpha) = K_{+}(\alpha) K_{-}(\alpha) ,$$

$$K(\alpha) = 2 I_o(\gamma b) K_o(\gamma b);\quad \gamma = (\beta_o^2 - \alpha^2)^{\frac{1}{2}}$$

and I_o, K_o are the modified Bessel functions of first and second kinds, E_{θ}^{i} is the incident electric-field amplitude, and θ_i is the incidence angle; c is an integration contour on the real axis of the complex α-plane, and z is the distance measured from the end of the cylinder. For an observation point away from the end on the cylinder, i.e. $\beta_o z >> 1$, Shen [1970] has shown in his paper that the major contribution to the integral comes from the region $|\alpha/\beta_o - 1| \sim (\beta_o z)^{-1}$. Thus, he proceeded to approximate the quantity $(\alpha-\beta_o \cos\theta_i)^{-1}$ by $\beta_o (1-\cos\theta_i)^{-1}$ in the evaluation of such

an integral, which subsequently yields the same result as given in Appendix B. We can see that when the incidence angle is near-grazing ($\theta_i \simeq 0$), the quantity $(\alpha-\beta_o \cos\theta_i)^{-1}$ actually will blow up as α is replaced by β_o. Thus, Shen's result is not valid in this case.

Chang and Lee have reevaluated the integral in a manner such that the approximation made by Shen is not needed. For the current on the outer surface of the cylinder, the result is similar to Shen's except that the so-called "reflection coefficient" R_s in Shen's formula is now modified as follows:

$$R_s(\theta_i,z) = R_{Shen}(\theta_i) - (\eta_o/2\pi)\exp(-iv_o)E_1(-iv_o);$$

$$v_o = 2\beta_o z \sin^2\theta_i/2 .$$

Thus, for the observation point sufficiently far from the end so that $v_o >> 1$, the second term is very small, and Shen's expression yields correct results. However, in the grazing direction, $v_o \to 0$, and the second term must be added to Shen's expression in order to yield a physically reasonable answer. In addition, the current that leaks into the inside of a tubular cylinder is also given by

$$I_{int}(\theta_i;z) \simeq T(\theta_i) I_o E_\theta^i e^{-\alpha_{01}(z/b)},$$

where

$$T(\theta_i) = \frac{i\beta b(1-\cos\theta_i)}{\pi j_{01}^2 H_0^{(1)}(j_{01})J_1(j_{01})} K_-(\beta_0\cos\theta_i); \quad I_0 = \frac{4\pi}{i\eta_0\beta_0\sin\theta_i K(\beta_0\cos\theta_i)}$$

and $\alpha_{01} = (j_{01}^2 - \beta_o^2 b^2)^{\frac{1}{2}}$ where j_{01} is the first zero of the Bessel function J_0, $J_{01} = .2405$.

Using a multi-reflection concept, one can now construct the modified form of Shen's expression for the current distribution on the tubular cylinder as well as the leakage current into the cylinder. The current on the cylinder is

$$I(\theta_i:z) = E_\theta^i \{I_{s\infty}(\theta_i:z) + C_{s2}\, I_\infty(h-z) + [\delta(\theta_i) + C_{s1}]\, I_\infty(h+z)\}$$

The expression is the same as Shen's formula given in Appendix B for $0 \leq \theta_i < \pi/2$, with the exception of the additional term $\delta(\theta_i)$, given by

$$\delta(\theta) = [R_s(\theta_i;2h) - R_s(\theta_i;h+z)]\, I_{s\infty}(\pi-\theta_i;h)$$

which usually is small, unless θ_i is near grazing. For $\pi/2 < \theta_i < \pi$ one uses the relationship, $I(\theta_i;z) = I(\pi-\theta_i;-z)$.

As shown by Chang and Lee, a similar procedure can be applied to obtain the leakage current into the cylinder. The result is given here:

$$I_{int}(\theta_i;z) = E_\theta^i\, [T(\theta) I_o(\theta) + T(\pi) C_{s2} I_\infty(2h)]\, e^{-\alpha_{01}(z/b)}$$

Here, the quantity $I_\infty(2h)$ is the current distribution at $z = 2h$ on an infinite antenna driven by a voltage generator located at $z = 0$, the expression for which is given in Appendix B. We further note that the leakage current into the tubular cylinder decays exponentially as $\exp(-\alpha_{01}\, z/b)$ which corresponds to an evanescent TM_{01}-mode. Since α_{01} is approximately two, the decay of leakage current is indeed very rapid. The coupling of the electromagnetic energy into the enclosure through apertures at a recessed end-cap can therefore be understood mainly as a tunneling effect.

For the case when a perturbing metallic rod is attached to the recessed end-cap, but the rod does not protrude from the hollow cylindrical end, leakage into the enclosure follows basically the same tunneling effect until it reaches the tip of the conducting rod. From then on, it continues in the form of a propagating wave, without further attenuation until it arrives at the end-cap where an aperture may be located. Consequently, the length of the conducting rod could be a dominant factor in determining the amount of electromagnetic energy that coupled into the enclosure.

APPENDIX D

Computer Programs

```
C     HARRISON AND TAYLOR SOLUTION INCORPORATING THE KING ONE-TERM
C     APPROXIMATION FOR THE EXTERIOR CURRENT.
C
C
C     INPUT --- FREQ (FREQUENCY),Z0,ZS,A ( RADIUS OF INNER CONDUCTOR),
C     B1 (OUTER RADIUS OF OUTER CONDUCTOR), B9 (INNER RADIUS OF OUTER
C     CONDUCTOR), H (HALF LENGTH OF THE CYLINDER EXTERIOR), S1 (DIS-
C     TANCE FROM THE CENTER OF THE APERTURE TO ZS), L (DISTANCE FROM THE
C     CENTER OF THE APERTURE TO Z0), Z (DISTANCE THE APERTURE IS OFFSET
C     FROM THE CENTER OF THE EXTERIOR LENGTH), AE (SEMI-MAJOR DIMENSION
C     OF THE APERTURE), BE (SEMI-MINOR DIMENSION FO THE APERTURE), TH1
C     (THETA ANGLE OF INCIDENCE), PHI (PHI ANGLE OF INCIDENCE).
C
C     INPUT PARAMETERS - ALL DISTANCES ARE IN METERS,ALL IMPEDANCES IN
C     OHMS,AND ALL ANGLES IN DEGREES.
C     OUTPUT --- CIS (ABSOLUTE VALUE OF LOAD CURRENT IN ZS IN MICRO-
C     AMPERES/VOLT/METER).
C
C
      COMMON A,B,C,C2,FREQ,B1,K,H
      REAL K,KELLIP,L,IMAG,MODI,INTR,INTI,INTUR,INTUI,MODTL,MODT
      COMPLEX I,D,FW,TEMP3,T,PSIU,PSIDU,IZ,T5,GW,IZEXT,EG,IG,IS,PEXT
      I=(0.0,1.0)
      PI=3.14159265
      U=4.*PI*1.E-7
      TH=TH1*PI/180.
      PHI=PHI1*PI/180.
      ZC=60*ALOG(B9/A)
      B=2.094395E-8*FREQ
      W=6.283186*FREQ
      HI=2*H
      S=S1+L
      T2=SIN(B*S)
      T3=COS(B*S)
      T4=COS(B*H)
      T7=COS(B*L)
      T8=SIN(B*L)
      D=ZC*(Z0+ZS)*T3+(ZC**2+Z0*ZS)*T2*I
      K=(1-(BE/AE)**2)
      CALL PSI(INTR,INTI, INTUR,INTUI)
      PSIU=INTR+INTI*I
      PSIDU=INTUR+I*INTUI
      FW=ZC*T7+I*Z0*T8
      GW=I*T8*ZC+Z0*T7
      IF(K.NE.0) GO TO 65
      Q=4./PI
      EELLIP=PI/2.
      KELLIP=PI/2.
      GO TO 66
65    CALL ELLIP(KELLIP,EELLIP)
      Q=K/(KELLIP-EELLIP)
66    IZEXT=I*(COS(B*XX)-T4)/(30.*B*(T4*PSIDU-PSIU))
      PEXT=SIN(B*XX)/(30.*W*(T4*PSIDU-PSIU))
      ALPHAXX=-PI*AE**3*Q/3.
      ALPHAYY=PI*AE**3*(1.-K)/(3.*EELLIP)
      EG=I*W*U*ALPHAXX*IZEXT/(8.*PI**2*B1**2)
      IG=-I*W*15.*ALPHAYY*PEXT/(PI*B1**2*ZC)
      IS=(EG*(ZC*T7+I*T8*Z0)+ZC*IG*(Z0*T7+ZC*T8*I))/D
      CIS=CABS(IS)*1.E+6
3     STOP    $    END
```

```
      SUBROUTINE ELLIP(KELLIP,EELLIP)
      COMPLETE ELLIPTIC INTEGRALS OF THE 1ST AND 2ND KIND
      COMMON A,B,C,C2,FREQ,B1,K,H
      REAL K,KELLIP
      TEMP1=.1713245*(FKINT(.9324695)+FKINT(-.9324695)) +
     1.3607616*(FKINT(.6612094)+FKINT(-.6612094))+
     2.4679139*(FKINT(.2386192)+FKINT(-.2386192))
      TEMP2=.1713245*(EINT(.9324695)+EINT(-.9324695))+
     1.3607616*(EINT(.6612094)+EINT(-.6612094))+
     2.4679139*(EINT(.2386192)+EINT(-.2386192))
      KELLIP=.7853982*TEMP1
      EELLIP=.7853982*TEMP2
      RETURN
      END

      FUNCTION FKINT(X)
      COMMON A,B,C,C2,FREQ,B1,K,H
      REAL K
      FKINT=1/SQRT(1-K*(SIN(.78538816*(X-1)))**2)
      RETURN
      END

      FUNCTION EINT(X)
      COMMON A,B,C,C2,FREQ,B1,K,H
      REAL K
      EINT=SQRT(1-K*(SIN(.78538816*(X+1)) )**2)
      RETURN
      END

      SUBROUTINE PSI(INTR,INTI,INTUR,INTUI)
      COMMON A,B,C,C2,FREQ,B1,K,H
      REAL INT1,INT2,K2,K1,INTR,INTI,INTUR,INTUI ,K
      TEMPR=.1894506*(F(.0950125)+F(-.0950125))+
     1.1826034*(  F(.2816036)+  F(-.2816036))+
     2.1691565*(  F(.4580168)+  F(-.4580168))+
     3.1495960*( F(.6178762)+ F(-.6178762))+
     4.1246290*(  F(.7554044)+  F(-.7554044))+
     5.0951585*(  F(.8656312)+  F(-.8656312))+
     6.0622535*(  F(.9445750)+ F(-.9445750))+
     7.0271525*(  F(.9894009)+  F(-.9894009))
      TEMPI=.1894506*(FF(.0950125)+FF(-.0950125))+
     1.1826034*( FF(.2816036)+ FF(-.2816036))+
     2.1691565*( FF(.4580168)+ FF(-.4580168))+
     3.1495960*(FF(.6178762)+FF(-.6178762))+
     4.1246290*( FF(.7554044)+ FF(-.7554044))+
     5.0951585*( FF(.8656312)+ FF(-.8656312))+
     6.0622535*( FF(.9445750)+FF(-.9445750))+
     7.0271525*( FF(.9894009)+ FF(-.9894009))
      C=COS(B*H)
      C1=1-C
      C2=COS(B*B1)*C1
      C3=2*C2*(ALOG(H+SQRT(H**2+B1**2))-ALOG(B1))
      K2=.189451*(F1(.095013)+F1(-.095013))+
     1.182603*(F1(.281604)+F1(-.281604))+
     2.169157*(F1(.458017)+F1(-.458017))+
     3.149596*(F1(.617876)+F1(-.617876))+
     4.124629*(F1(.755404)+F1(-.755404))+
     5.095159*(F1(.865631)+F1(-.865631))+
     6.062254*(F1(.944575)+F1(-.944575))+
     7.027152*(F1(.989401)+F1(-.989401))
      K1=.189451*(F2(.095013)+F2(-.095013))+
     1.182603*(F2(.281604)+F2(-.281604))+
     2.169157*(F2(.458017)+F2(-.458017))+
     3.149596*(F2(.617876)+F2(-.617876))+
     4.124629*(F2(.755404)+F2(-.755404))+
     5.095159*(F2(.865631)+F2(-.865631))+
     6.062254*(F2(.944575)+F2(-.944575))+
     7.027152*(F2(.989401)+F2(-.989401))
```

```
      INT1=-H*K2
      INT2=H*K1
      TEMDUI=.1894506*(FUI(.0950125)+FUI(-.0950125))+
     1.1826034*(FUI(.2816036)+FUI(-.2816036))+
     2.1691565*(FUI(.4580168)+FUI(-.4580168))+
     3.1495960*(FUI(.6178762)+FUI(-.6178762))+
     4.1246290*(FUI(.7554044)+FUI(-.7554044))+
     5.0951585*(FUI(.8656312)+FUI(-.8656312))+
     6.0622535*(FUI(.9445750)+FUI(-.9445750))+
     7.0271525*(FUI(.9894009)+FUI(-.9894009))
      INTR=H*TEMPR
      INTI=-H*TEMPI
      INTUR=(INT1+(INT2+C3)/C1
      INTUI=H*TEMDUI/C1
      RETURN
      END

      FUNCTION F(X)
      COMMON A,B,C,C2,FREQ,B1,K,H
      REAL K
      R=SQRT((H*(1-X))**2+B1**2)
      F=COS(B*R)*(COS(B*H*X)-COS(B*H))/R
      RETURN
      END

      FUNCTION FF(X)
      COMMON A,B,C,C2,FREQ,B1,K,H
      REAL K
      R=SQRT((H*(1-X))**2+B1**2)
      FF=SIN(B*R)*(COS(B*H*X)-COS(B*H))/R
      RETURN
      END

      FUNCTION FUI(X)
      COMMON A,B,C,C2,FREQ,B1,K,H
      REAL K
      R=SQRT((H*(1-X))**  2+B1**2)
      R1=SQRT((H*X)**2+B1**2)
      FUI=((COS(B*H*X)-COS(B*H))*(R1*SIN(B*R)-R*SIN(B*R1)))/(R*R1)
      RETURN
      END

      FUNCTION F1(X)
      COMMON A,B,C,C2,FREQ,B1,K,H
      REAL K
      R=SQRT((H*(1-X))**2+B1**2)
      F1=(COS(B*H*X)-C)*COS(B*R)/R
      RETURN
      END

      FUNCTION F2(X)
      COMMON A,B,C,C2,FREQ,B1,K,H
      REAL K
      R1=SQRT((H*X)**2+B1**2)
      F2=(COS(B*R1)*(COS(B*H*X)-C)-C2)/R1
      RETURN
      END
```

```
C     HARRISON AND TAYLOR SOLUTION INCORPORATING THE SHEN FORMULATION
C     FOR THE EXTERIOR CURRENT.
C
C
C     INPUT --- FREQ (FREQUENCY),ZO,ZS,A ( RADIUS OF INNER CONDUCTOR),
C     B1 (OUTER RADIUS OF OUTER CONDUCTOR), B9 (INNER RADIUS OF OUTER
C     CONDUCTOR), H (HALF LENGTH OF THE CYLINDER EXTERIOR), S1 (DIS-
C     TANCE FROM THE CENTER OF THE APERTURE TO ZS), L (DISTANCE FROM THE
C     CENTER OF THE APERTURE TO ZO), Z (DISTANCE THE APERTURE IS OFFSET
C     FROM THE CENTER OF THE EXTERIOR LENGTH), AE (SEMI-MAJOR DIMENSION
C     OF THE APERTURE), BE (SEMI-MINOR DIMENSION FO THE APERTURE), TH1
C     (THETA ANGLE OF INCIDENCE).
C
C     INPUT PARAMETERS - ALL DISTANCES ARE IN METERS,ALL IMPEDANCES IN
C     OHMS,AND ALL ANGLES IN DEGREES.
C
C     OUTPUT --- CIS (ABSOLUTE VALUE OF LOAD CURRENT IN ZS IN MICRO-
C     AMPERES/VOLT/METER).
C
C
      COMMON K,I,GAM,ETA,PI,CW,TH,W,A,B,C,C2,FREQ,B1,H
      REAL K,KELLIP,L
      COMPLEX I,D,IZEXT,PEXT,EG,IG,IS,IINF,ISINF,R,RS,RHOI,RHOSI,CS1,CS2
      COMPLEX CSD
      I=(0.0,1.0)
      PI=3.14159265
      U=4.*PI*1.E-7
      TH=TH1*PI/180.
      PHI=PHI1*PI/180.
      B=2.094395E-8*FREQ
      W=6.283186*FREQ
      GAM=.57721566
      CW=ALOG(1./(B*B1))-GAM
      R=120.*(CW+I*PI/2.)
      ETA=120.*PI
      ZC=60*ALOG(B9/A)
      S=S1+L
      HI=2*H
      T2=SIN(B*S)
      T3=COS(B*S)
      T4=COS(B*H)
      T7=COS(B*L)
      T8=SIN(B*L)
      D=ZC*(ZO+ZS)*T3+(ZC**2+ZO*ZS)*T2*I
      K=(1-(BE/AE)**2)
      IF(K.NE.0) GO TO 65
      Q=4./PI
      EELLIP=PI/2.
      KELLIP=PI/2.
      GO TO 66
65    CALL ELLIP(KELLIP,EELLIP)
      Q=K/(KELLIP-EELLIP)
66    CSD=1.-R*R*IINF(2.*H)**2
      CS1=(R*RS(PI-TH)*ISINF(H)*IINF(2.*H)-RS(TH)*ISINF(-H))/CSD
      CS2=(R*RS(TH)*ISINF(-H)*IINF(2.*H)-ISINF(H)*RS(PI-TH))/CSD
      IZEXT=ISINF(Z)+CS1*IINF(H+Z)+CS2*IINF(H-Z)
      IZEXT=CONJG(IZEXT)
      PEXT=RHOSI(Z)+CS1*RHOI(H+Z)+CS2*RHOI(H-Z)
      PEXT=CONJG(PEXT)
      ALPHAXX=-PI*AE**3*Q/3.
      ALPHAYY=PI*AE**3*(1.-K)/(3.*EELLIP)
      EG=I*W*U*ALPHAXX*IZEXT/(8.*PI**2*B1**2)
      IG=-I*W*15.*ALPHAYY*PEXT/(PI*B1**2*ZC)
      IS=(EG*(ZC*T7+I*T8*ZO)+ZC*IG*(ZO*T7+ZC*T8*I))/D
      CIS=CABS(IS)*1.E+6
3     STOP    $    END
```

```
      SUBROUTINE ELLIP(KELLIP,EELLIP)
      COMPLETE ELLIPTIC INTEGRALS OF THE 1ST AND 2ND KIND
      COMMON K,I,GAM,ETA,PI,CW,TH,W,A,B,C,C2,FREQ,B1,H
      REAL K,KELLIP
      TEMP1=.1713245*(FKINT(.9324695)+FKINT(-.9324695)) +
     1.3607616*(FKINT(.6612094)+FKINT(-.6612094))+
     2.4679139*(FKINT(.2386192)+FKINT(-.2386192))
      TEMP2=.1713245*(EINT(.9324695)+EINT(-.9324695))+
     1.3607616*(EINT(.6612094)+EINT(-.6612094))+
     2.4679139*(EINT(.2386192)+EINT(-.2386192))
      KELLIP=.7853982*TEMP1
      EELLIP=.7853982*TEMP2
      RETURN
      END

      FUNCTION FKINT(X)
      COMMON K,I,GAM,ETA,PI,CW,TH,W,A,B,C,C2,FREQ,B1,H
      REAL K
      FKINT=1/SQRT(1-K*(SIN(.78538816*(X-1)))**2)
      RETURN
      END

      FUNCTION EINT(X)
      COMMON K,I,GAM,ETA,PI,CW,TH,W,A,B,C,C2,FREQ,B1,H
      REAL K
      EINT=SQRT(1-K*(SIN(.78538816*(X+1)) )**2)
      RETURN
      END

      FUNCTION IINF(Z)
      COMMON K,I,GAM,ETA,PI,CW,TH,W,A,B,C,C2,FREQ,B1,H
      COMPLEX I,IINF,T9
      TT=B*Z+SQRT(B*B*Z*Z+EXP(-2.*GAM))
      T9=1.-2.*PI*I/(2.*CW+ALOG(TT)+GAM+I*1.5*PI)
      IINF=I*CEXP(I*B*Z)*CLOG(T9)/ETA
      RETURN
      END

      FUNCTION ISINF(Z)
      COMMON K,I,GAM,ETA,PI,CW,TH,W,A,B,C,C2,FREQ,B1,H
      COMPLEX I,D9,ISINF
      D9=(CW-ALOG(SIN(TH)/2.)+I*PI/2.)*ETA*SIN(TH)
      ISINF=I*CEXP(I*B*Z*COS(TH))/D9
      RETURN
      END

      FUNCTION RS(T)
      COMMON K,I,GAM,ETA,PI,CW,TH,W,A,B,C,C2,FREQ,B1,H
      COMPLEX I,RS
      RS=60.*(2.*CW-ALOG(.5-COS(T)/2.)+I*PI)
      RETURN
      END

      FUNCTION RHOI(Z)
      COMMON K,I,GAM,ETA,PI,CW,TH,W,A,B,C,C2,FREQ,B1,H
      COMPLEX I,U2,U3,U4,U5,RHOI
      UU=EXP(-2.*GAM)
      U0=B*Z+SQRT(B*B*Z*Z+UU)
      U1=ALOG(U0)
      U2=2.*CW+GAM+I*1.5*PI
      U3=-2.*PI*I/(1.-2.*PI*I/(U1+U2))
      U4=-U3/(U1+U2)**2
      U5=U4/U0
      RHOI=(-CEXP(I*B*Z)/(W*ETA))*(U5*(B+B**2*Z/(U0-B*Z))+I*B*CLOG(1.-2.
     1*PI*I/(U1+U2)))
      RETURN
      END

      FUNCTION RHOSI(Z)
      COMMON K,I,GAM,ETA,PI,CW,TH,W,A,B,C,C2,FREQ,B1,H
      COMPLEX I,RHOSI,D9
      D9=B*ETA*SIN(TH)*(CW-ALOG(SIN(TH)/2.)+I*PI/2.)
      RHOSI=-I*B*COS(TH)*CEXP(I*B*Z*COS(TH))/D9
      RETURN
      END
```